

***In vitro* evaluation of bone cell response to novel 3D-
printable nanocomposite biomaterials for bone
reconstruction**

by

Zahra Haghpanah

A thesis

presented to the University of Waterloo

in fulfilment of the

thesis requirement for the degree of

Master of Applied Science

in

Systems Design Engineering

Waterloo, Ontario, Canada, 2022

© Zahra Haghpanah 2022

Author's Declaration

I hereby declare that I am the sole author of this thesis. This is a true copy of the thesis, including any required final revisions, as accepted by my examiners.

I understand that my thesis may be made electronically available to the public.

Abstract

Critical-sized segmental bone defects are a challenging problem for orthopedic surgeons. These defects are unable to heal spontaneously within a patient's lifetime. Thus, biomaterials are used to repair such defects and provide a substitute for the lost bone in order to recover both structure and function. Biomaterials should ideally be osteoconductive, osteoinductive, and resorbable to stimulate osteogenic differentiation and remodeling in addition to having sufficient mechanical properties. Biomaterials designed to undergo remodeling should present a balance between the biomaterial's resorption and new tissue formation. Thus, the interaction of any novel biomaterial with bone cells, osteoblasts and osteoclasts, should be investigated.

In this research, a set of novel 3D printable nanocomposite biomaterials containing acrylated epoxidized soybean oil (AESO) or methacrylated AESO (mAESO), polyethylene glycol diacrylate (PEGDA), and nanohydroxyapatite (nHA) was produced using a masked stereolithography (mSLA)-based 3D printer. The effects of volume fraction of nHA and methacrylated AESO on the interactions of bone cells (osteoblasts and osteoclasts) with the nanocomposites were evaluated *in vitro* and compared to a control biomaterial, hydroxyapatite (HA). Two separate studies, one using osteoblasts and the other osteoclasts, were performed to characterize cell response.

In the osteoblast study, immortalized mouse pre-osteoblast MC3T3-E1 cells were differentiated to osteoblasts (dMC3T3-OB). The effects of the addition of nHA and methacrylation of AESO on osteoblast-like cells were studied. Adhesion, proliferation, and activity of dMC3T3-OB were studied by seeding cells on the 3D-printed discs for 1, 3, and 7 days. Overall, each of the nanocomposites was shown to support dMC3T3-OB cells' adhesion, proliferation, and activity, and compared to the HA control. Incorporating higher amounts of nHA enhanced cell adhesion and proliferation, although it didn't influence cell activity, as measured by Alkaline Phosphatase (ALP). The presence of mAESO in the nanocomposites resulted in greater adhesion, proliferation, and activity at day 7 compared to the AESO nanocomposites, which may be explained by the increase in stiffness of mAESO nanocomposites.

In the osteoclast study, mouse RAW 264.7 macrophages were differentiated to osteoclasts using receptor activator of nuclear factor kappa-B ligand (RANKL). The differentiated cells were purified by serum gradient purification and then were cultured on nanocomposites to evaluate their osteoclast-mediated resorption. The adhesion and activity of the differentiated and purified RAW 264.7 cells (dRAW-OC, osteoclast-like cells) were studied by seeding the cells on 3D-printed discs for 7 days. The effect of methacrylation of AESO on the adhesion, tartrate-resistant acid phosphatase (TRAP) staining, actin ring size, number of osteoclast-like cells, and number of nuclei per osteoclasts were investigated. Results showed excellent osteoclast-like cells survival, defined actin rings, large multinucleated cells, and higher number of TRAP-positive cells on mAESO-based nanocomposites compared to AESO-based one. The osteoclast response on the mAESO discs was also comparable to the HA control. Calcein staining was used to visualize pit formation on the biomaterials. AESO-based and mAESO-based nanocomposites, and surprisingly the HA discs, did not exhibit any sign of resorption pits formed by the osteoclast-like cells. While we were unable to obtain osteoclast-mediated resorption pits, a confocal image of a pit-like structure was obtained as a proof-of-concept to perform depth and volume calculation.

Taken all together, the results presented in this thesis demonstrated that mAESO-based nanocomposites containing higher amounts of nHA had better interactions with osteoblast-like and osteoclast-like cells, comparable to interactions with HA controls. This suggests future potential for bone defect repair.

Acknowledgments

I would like to express my sincere respect and appreciation to both of my supervisors, Dr. Thomas Willett and Dr. Maud Gorbet, for their guidance and assistance during the pursuit of my studies. Thanks to my thesis readers, Dr. Eline Boghaert and Dr. Ewen MacDonald, for their valuable time and comments. I would also thank Dr. Michaela Strüder-Kypke and Corin Alexander Seelemann for training and helping me with confocal microscopy (Molecular and Cellular Imaging Facility, University of Guelph). Moreover, I would like to express my gratitude to all the group members in Waterloo Composite Biomaterial Systems and Material Interactions with Biological Systems labs for their support. I am also grateful to my family, especially, my parents for all their love, presence, patience, and support. Last but not least, I would like to thank one of the persons that I most care about, Hossein, as my best friend in life who has provided the most important mental support for my graduate studies. My family encourages me to move forward and makes my life meaningful and colorful.

Table of Contents

Author’s Declaration.....	ii
Abstract.....	iii
Acknowledgments.....	v
List of Figures.....	viii
List of Tables.....	x
List of Abbreviations.....	xi
1 Introduction.....	1
2 Literature Review.....	6
2.1 Bone biology and structure.....	6
2.2 Bone cells.....	9
2.2.1 Osteoblasts: Osteoblastogenesis and bone formation.....	10
2.2.1.1 Experimental model to study osteoblasts in-vitro.....	11
2.2.2 Osteoclasts: Osteoclastogenesis and bone resorption.....	12
2.2.2.1 Experimental model to study osteoclasts in-vitro.....	15
2.3 Bone remodeling.....	17
2.4 The bone fracture healing mechanism.....	19
2.5 Critical-sized segmental bone defect and current treatment.....	20
2.6 Biomaterials for bone reconstruction.....	22
2.6.1 Required properties for bone biomaterials.....	22
2.6.2 Nanocomposite biomaterials.....	25
2.6.2.1 Hydroxyapatite.....	26
2.6.2.2 Polymers.....	29
2.6.2.2.1 Acrylated epoxidized soybean oil.....	30
2.6.2.2.1.1 Functionalization of AESO.....	30
2.7 Overview of 3D-printing.....	32
3 Objectives and Hypotheses.....	35
4 Materials and Methods.....	37
4.1 Fabrication of 3D-printed nanocomposite discs.....	38
4.1.1 3D-printing nanocomposite discs with mSLA printer.....	38
4.2 <i>In vitro</i> osteoblast study on nanocomposite biomaterials.....	39
4.2.1 Osteoblastic differentiation and alizarin red staining.....	39
4.2.2 Culturing dMC3T3-OB cells on nanocomposite discs.....	42
4.2.3 Evaluation of dMC3T3-OB cells interaction with nanocomposite discs.....	43

4.3	<i>In-vitro</i> osteoclast study on nanocomposite biomaterials	46
4.3.1	Differentiation of RAW264.7 cells to osteoclasts and serum gradient purification	46
4.3.1.1	TRAP staining of purified cells	47
4.3.2	Culturing dRAW-OC cells on SP30 and mSP30 nanocomposite discs	48
4.3.3	Evaluation of dRAW-OC cells interaction with SP30 and mSP30 nanocomposite discs...	49
4.3.3.1	TRAP Staining	49
4.3.3.2	F-Actin and Nuclei Staining	50
4.3.3.3	Resorption pit assay	51
4.3.3.4	Confocal laser microscopy and analysis	51
4.4	Statistical Analysis.....	52
5	Evaluation of dMC3T3-OB cells responses to the 3D-printed nanocomposite discs: results and discussion.....	53
5.1	dMC3T3-OB cells proliferation and viability on SP0, SP5, and SP10 nanocomposite discs.....	53
5.2	dMC3T3-OB cells proliferation, viability, and ALP activity on SP10, mSP10, SP30, and mSP30 nanocomposite discs	55
5.3	Discussion	59
6	Evaluation of dRAW-OC cells responses to the 3D-printed nanocomposite discs: results and discussion.....	64
6.1	Characterization of dRAW-OC cells on SP30 and mSP30 nanocomposite discs.....	64
6.1.1	TRAP staining of dRAW-OC cells on nanocomposite discs.....	64
6.1.2	F-Actin/DAPI staining of dRAW-OC cells on nanocomposite discs	65
6.1.3	Calcein staining of nanocomposite’s surface to observe resorption pits	69
6.2	Discussion	72
7	Conclusion, Limitations, and Recommendation for Future Work.....	77
7.1	Conclusion	77
7.2	Limitations	77
7.3	Recommendation and Future Works.....	79
	Letter of Copyright Permission.....	81
	References.....	97
	Appendix 1 – Pilot study of osteoblast interaction with nanocomposites containing 30% nHA.....	116
	Appendix 2 – Osteoclast proliferation and morphology on nanocomposite discs	120

List of Figures

Figure 1-1. A radiograph of critical-sized bone defect the ulna of a dog [10].	1
Figure 1-2. Different grafts types used in the bone defects treatment [23].	2
Figure 2-1. Hierarchical structural organization of bone with different levels and structures [47]	6
Figure 2-2. Trabecular (spongy) and cortical (compact) bone tissues differ in their microarchitecture and porosity [48].	7
Figure 2-3. Illustration of a) components of compact bone [51], and b) spongy bone, periosteum, and endosteum [52].	8
Figure 2-4. Diagram of immature bone (Woven) and mature bone (Lamellar) [53].	9
Figure 2-5. Four types of cells are found within bone tissue [51]	10
Figure 2-6. Strategies of osteoblastogenesis [60]	11
Figure 2-7. Osteoclastogenesis pathway [60]	13
Figure 2-8. Mechanism of bone resorption. Ctsk: cathepsin K [77].	15
Figure 2-9. The bone remodeling process [106]	17
Figure 2-10. Illustration of the four stages of the bone healing process [118]	19
Figure 2-11. A: Fracture of the distal femur after a road traffic accident, B: Distal femur reconstruction with megaprosthesis [135], C: Implantation of a total femoral prosthesis after resection of the tumor [8].	22
Figure 2-12. A graphical representation of relationship between toughness and modulus of various HA-based composite materials [148].	26
Figure 2-13. The chemical structure of AESO [165].	30
Figure 2-14. Reaction during the modification of AESO to synthesize mAESO [168]	31
Figure 2-15. 3D printing methods: Direct Ink Writing and Masked Stereolithography. ©Composite Biomaterial Systems Laboratory, University of Waterloo.	34
Figure 4-1. (Left) Image of the AnyCubic Photon mSLA 3D-printer and (Right) AESO-based nanocomposite discs printed using the AnyCubic Photon mSLA printer.	39
Figure 4-2. MC3T3-E1 after 14 (A, B) and 21 (C, D) days of osteogenic differentiation.	41
Figure 4-3: Discs in silicone tubes to keep cell suspension on the surface.	43
Figure 4-4: Nikon Eclipse TS100	44
Figure 4-5. <i>In vitro</i> methodology to assess OB-like cells interactions with nanocomposites.	45
Figure 4-6. Serum gradient purification of differentiated RAW 264.7 cells in a 50 ml tube.	47
Figure 4-7. Isolated TRAP-positive dRAW264.7 osteoclasts by serum gradient.	48
Figure 4-8. TRAP-positive dRAW264.7 osteoclasts from the bottom fraction of the serum gradient purification.	50
Figure 4-9. <i>In vitro</i> methodology to assess OC-like cells interactions with nanocomposites.	52

Figure 5-1: Differentiated MC3T3-E1 osteoblast cell viability and adhesion on 3D printed nanocomposite discs. Representative images of live/dead staining of cells on SP0, SP5, SP10, and HA discs at day 1, 3, and 7 days after seeding [177].	54
Figure 5-2. Differentiated MC3T3-E1 osteoblast cell proliferation on 3D printed nanocomposite discs. Proliferation of dMC3T3-OB cells as measured using the XTT assay [177].	55
Figure 5-3. Differentiated MC3T3-E1 osteoblast cell viability and adhesion on 3D printed nanocomposite discs. Representative images of live/dead staining of cells on SP10, mSP10, SP30, mSP30 and HA discs at day 1, 3, and 7 days after seeding.	56
Figure 5-4. Differentiated MC3T3-E1 osteoblast cell proliferation on 3D printed nanocomposite discs. Proliferation of dMC3T3-OB cells as measured by XTT assay.	57
Figure 5-5. ALP expressed by differentiated MC3T3-E1 osteoblast cells cultured on the nanocomposite discs.	58
Figure 5-6. ALP activity of dMC3T3-OB cells cultured on the nanocomposite discs. The amount of ALP was normalized to XTT data.	59
Figure 6-1. dRAW-OC cells were cultured on nanocomposite discs with RANKL for 7 days and stained for TRAP. Representative images of TRAP staining on SP30, mSP30 and HA discs on day 7 (n=3).	65
Figure 6-2. dRAW-OC cells were cultured on SP30, mSP30, and HA disc for 7 days. Osteoclast-like cells were stained with DAPI and Alexa Fluor 488-Phalloidin, and the number of nuclei per osteoclast was counted.	66
Figure 6-3. Morphology evaluation of osteoclast-like cells on mSP30 nanocomposite disc.	67
Figure 6-4. Morphological evaluation of osteoclast-like cells cultured on SP30, mSP30, and HA discs, stained with DAPI and Alexa Fluor 488-Phalloidin.	68
Figure 6-5. dRAW-OC cells were cultured on SP30, mSP30, and HA disc for 7 days. Osteoclast-like cells were stained with DAPI and Alexa Fluor 488-Phalloidin, and the diameter of actin rings on multinucleated cells was determined.	69
Figure 6-6. Representative images of calcein staining of nanocomposite discs by fluorescence microscope. dRAW-OC cells were cultured on SP30, mSP30, and HA disc for 7 days.	70
Figure 6-7. Pit 3D visualization by confocal microscopy on SP30 disc.	71
Figure 6-8. Pit 3D visualization by confocal microscopy on SP30 disc.	71
Figure 10-1. Image of Hyrel 3D-printer and discs	117
Figure 10-2. A) Tensile strength and elastic modulus values of 3D printed SP30 nanocomposites. B) Osteoblast metabolic activity as measured by the XTT assay. C) Live-dead assay showing live cells (green) and dead cells (red). D) Cytoskeletons of osteoblast cells seeded on the nanocomposites for day-1 and day-3.	119
Figure 11-1. dRAW-OC cells proliferation on 3D printed nanocomposite discs. Proliferation of dRAW-OC cells as measured using the XTT assay.	120
Figure 11-2. SEM images RAW264.7 and dRAW-OC cells grown on SP10 and SP30 nanocomposite discs under RANKL stimulation at day 14.	121

List of Tables

Table 2-1: Biomechanical properties of bone [31]	23
Table 2-2: Biomaterials' classification for bone grafting [31].....	24
Table 4-1. Compositions of nanocomposite inks.....	39
Table 4-2: Ingredients to make 10 ml of osteogenesis induction media.....	40

List of Abbreviations

AA	ascorbic acid 2-phosphate
AESO	Acrylated Epoxidized Soybean Oil
ALP	Alkaline Phosphatase
ARS	Alizarin Red Staining solution
CPCs	Calcium Phosphate Cements
CSBDs	Critical-sized segmental bone defects
CTSK	Cathepsin K
dMC3T3-OB	Differentiated MC3T3-E1 cells
dRAW-OC	Differentiated RAW264.7 cells
DIW	Direct Ink Writing
DMEM	Dulbecco's Modified Eagle Medium
EthD-1	ethidium homodimer
ECM	Extracellular Matrix
FBS	Fetal Bovine Serum
FBGCs	Foreign Body Giant Cells
GPh	β -glycerophosphate
HA	Hydroxyapatite
M-CSF	Macrophage Colony-Stimulating Factor
mSLA	masked stereolithography
MSCs	Mesenchymal Stem Cells
mAESO	Methacrylated AESO
MC3T3-E1	Mouse pre-osteoblast immortalized MC3T3-E1 cells
nHA	nano-hydroxyapatite
OB	Osteoblasts
OCN	Osteocalcin
OC	Osteoclasts
P/S	Penicillin/streptomycin
PBS	Phosphate-Buffered Saline
PEGDA	Polyethylene Glycol Diacrylate
PMMA	Poly (methyl methacrylate)
RAW 264.7	RAW 264.7 Murine Macrophages
RANKL	Receptor Activator of Nuclear Factor- κ B Ligand
Rpits	Resorption pits
RT	Room Temperature
SEM	Scanning Electron Microscopy
TRAP	Tartrate-resistant Acid Phosphatase
α-MEM	α -modified Minimum Essential Medium

1 Introduction

Critically-sized segmental bone defects (CSBDs) resulting from bone metastases resection, severe fractures, traumatic injuries, and severe infection resection are a significant clinical orthopedic challenge [1][2]. A critical-sized bone defect is defined as a segmental bone loss when the defect size or length is greater than 2-2.5 times the diameter of the affected long bone (Figure 1-1) [1][3]. Although bone tissue has a remarkable ability to regenerate and heal itself, critically sized segmental bone defects and complex fractures do not heal spontaneously within a patient's lifetime and therefore require surgical intervention [4]. Regeneration/reconstruction of these defects requires donor-derived or synthetic grafts [5][6].

Annually, billions of dollars are spent in the United States to repair critically sized bone defects, and over two million operations are performed globally [7]. As of 2013, there were 59 bone graft substitutes marketed by 17 companies in the UK available for implantation. Only 37% of products had clinical data [8]. Although there are synthetic biomaterials available that have represented good clinical success in the treatment of bone injuries, to the best of our knowledge, none of the currently available synthetic grafts have combined load-bearing property, resorbability, and the ability to match the osteogenic and osteoinductive qualities of natural bone graft [9]. There is thus a need for a biomaterial that can fill critically sized bone defects, supporting the osteogenic process and resorbing at a controlled rate.



Figure 1-1. A radiograph of a critical-sized bone defect of the ulna of a dog. Reprinted with permission from [10].

Bone graft is ranked as the second most common transplanted tissue [11]. Roughly speaking, 2.2 million bone grafting surgeries are done worldwide annually at the cost of \$2.5 billion. [12]. Although an

autograft, a piece of bone that is harvested from the patient's healthy tissue from a non-load-bearing area (like iliac crest or pelvis) and then implanted at the defect site [11], is the gold standard of care for bone defects, it is complicated by donor site morbidity, anesthesia time, and insufficient graft volume for CSBDs treatment (Figure 1-2-a) [4][13]. Thus, current treatments for CSBD reconstruction are allografts, a piece of bone that is taken from human cadavers or donors [11], and metal megaprotheses, an implant designed to replace the resected large bone segment [5], (Figure 1-2-b, c). Allografts have better mechanical stability than autografts, allowing large bone defect reconstruction without donor site morbidity [14]. However, allografts do not repair as quickly or as completely as autografts, they carry some risk of donor-to-recipient disease transmission and have limited ability to revascularize and remodel [13]. Massive structural allografts (those used to treat CSBD) have several complications, including fracture, infection, and nonunion [15]. For example, 40% of failures are due to fractures when allografts are used for CSBD reconstruction [13]. Reconstruction with metal alloy megaprotheses is one of the treatments of large bone defects. While megaprotheses are used to provide structural and mechanical support [16], they have different shortcomings such as aseptic loosening, fatigue fractures, local recurrence of the tumor, deep infections, mechanical failure, and dislocation [17][18][19][20]. The high complication rate associated with allografts and metal alloy mega-protheses has highlighted the need for developing new approaches using novel synthetic biomaterials engineered to serve as bone graft substitutes [13].

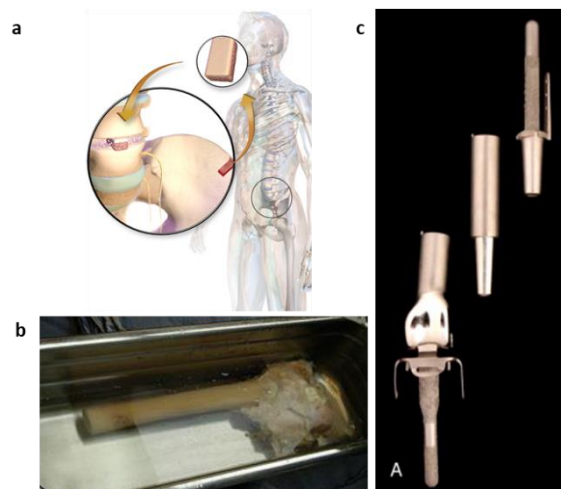


Figure 1-2. Different grafts types used in the bone defects treatment; a) autograft harvested from iliac crest [21], b) allograft [22], c) metal megaprosthesis system. Reprinted with permission from [23].

These engineered biomaterials should possess properties that match both the mechanical and biological context of bone tissue matrix [24]. The biomaterials should promote integration with host bone, osteogenesis, and angiogenesis while having the desired and sufficient mechanical stability and facilitating load transfer under weight-bearing conditions [1]. The biomaterial must have essential properties such as biocompatibility, osteoconductivity (i.e., ability to support the attachment of osteoprogenitor cells and osteoblasts), osteoinductivity (i.e., ability to increase the osteoprogenitor cell differentiation into osteoblasts), and bioactivity (i.e., ability to develop a direct and robust bonding with bone tissue through the formation of bone-like apatite [25]) [6]. A bone biomaterial should be replaced by mature bone without transient loss of mechanical support. This means the biomaterial should be resorbable in a controlled manner [26]. Also, to conform to irregularly shaped defects and match patient-specific anatomy, the biomaterial should be 3D printable.

Poly (methyl methacrylate) (PMMA), calcium phosphate cements (CPCs), and bioactive glass composites are some examples of synthetic biomaterials that are currently used to repair non-critically sized defects. Despite having a high strength (≥ 70 MPa), PMMA is non-resorbable and does not integrate with host bone, which leads to device loosening and long-term failure [27][28]. Ceramic biomaterials composed of hydroxyapatite or tri-calcium phosphate are attractive options since they are resorbable/degradable and osteoconductive and act similar to natural bone in compression [13]. However, their use is limited by brittleness, and they are subject to fracturing due to the repeated loading [29]. Moreover, bioactive glass composites present remarkable mechanical properties but uncontrolled resorption [30]. Since these conventional biomaterials are unsuitable for CSBD reconstruction, composite biomaterials are being developed to attain the desired mechanical and biological properties [13].

Composite biomaterials provide the possibility of making bone grafts equivalent to the autogenous bone by integrating all the factors associated with osteoconduction, osteoinduction, osteogenicity, and bioresorbability [31]. Natural bone has a unique physiologic microstructure, a nanocomposite of collagen and hydroxyapatite, an ideal framework for bone development and physiologic regeneration [32]. Accordingly, synthetic grafts are designed as nanocomposites to mimic bone microstructure, present bone-

like strength, stimulate osteogenic differentiation, and be resorbable at a controlled rate relevant to patient biology [2][29]. Bone cells' attachment, spreading, and differentiation on implanted graft materials are crucial for bone formation [33]. Once implanted, bone graft biomaterials interact with the local cells, osteoblasts (i.e., bone-forming cells), and osteoclasts (i.e., bone-resorbing cells). Prior works indicate that osteoblasts are more critical for implant osseointegration [34][35]. However, osteoclasts are critical in determining an implant's longevity [36][37]. A controlled resorption rate is critical since implant strength should be maintained until the regenerated tissue can provide mechanical support, cell penetration, and vascularization [38]. Through controlled resorption, the biomaterial integrates with the bone remodeling process [6], which is the most important physiological process in the skeleton that osteoblasts and osteoclasts are involved in [16][39].

In-vitro testing is essential in estimating the material properties of biomaterials, such as biocompatibility and cytotoxicity [32]. In-vitro cell-based assays are easy, reproducible, and inexpensive compared to *in vivo* studies [6]. Most of the published research reports on biocompatibility and *in vitro* cell-material interactions use only osteoblasts, and few studies consider the significance of the osteoclast response [40]. However, osteoblasts and osteoclasts work cooperatively during bone tissue remodeling. So, both are essential for developing new healthy bone within a defect site [41][42]. The osteoclast response evaluation provides valuable information regarding osteoclast-mediated resorption of a new biomaterial and indicates its potential as a future bone graft material [36]. Therefore, the study of both osteoblast and osteoclast responses is required to ensure the complete characterization of a new synthetic bone biomaterial.

My thesis is a crucial part of a research program focused on developing competent 3D-printable nanocomposite biomaterials for critically sized bone defect reconstruction. The nanocomposite system developed in the Waterloo Composite Biomaterial Systems Laboratory (WCBSL) combines an inorganic phase, nano-hydroxyapatite (nHA), and an organic phase, acrylated epoxidized soybean oil (AESO) or methacrylated AESO (mAESO), and polyethylene glycol diacrylate (PEGDA). This thesis provides a novel and robust means for evaluating our new class of advanced 3D printable nanocomposite based on the responses of osteoblasts and osteoclasts. The new methods and materials presented herein will significantly

impact skeletal biomaterials' development and selection of novel bone graft substitutes to reconstruct critically sized segmental bone defects (CSBDs).

This thesis is organized as follows. Chapter 2 includes the literature review relevant to this research thesis. Chapters 3 and 4 present the objectives/hypotheses and the materials and methods, respectively. In Chapter 5, the results and discussion of the osteoblast study are reported, and Chapter 6 presents the investigation with osteoclasts. Finally, in Chapter 7, conclusion, limitations, and recommendations for future work are presented.

2 Literature Review

2.1 Bone biology and structure

Bone is a living tissue material that can adapt to changes in its physiological or mechanical environment [43]. It is essential to understand bone composition, architecture, and bone matrix organization to develop bone-inspired graft materials successfully. As shown in Figure 2-1, bone has a hierarchical structure from the nanoscale to the macro-scale: collagen molecules, bone mineral crystals, and non-collagenous organic proteins; collagen fibrils; bone lamella, Haversian systems, and osteons; cancellous and cortical bone [44].

Bone is a composite material with two major phases: 65 wt% of bone consists of an inorganic phase known as mineralized matrix, and 35 wt% is an organic matrix [45][46]. The mineralized matrix is composed of poorly crystalline, highly substituted hydroxyapatite ($\text{Ca}_{10}(\text{PO}_4)_6(\text{OH})_2$) with other minute constituents such as carbonate, citrate, magnesium, fluoride, and strontium [46]. The organic matrix comprises 90% type I collagen and 10% noncollagenous proteins such as glycoproteins, proteoglycans, morphogenetic proteins, integrin-binding proteins, and growth factors [46]. Hydroxyapatite nucleates into collagen fibrils where collagen fibrils provide a nano-scale structural template, and hydroxyapatite gives the strength and stiffness to the structural frame to withstand compression and bending stresses [45][46].

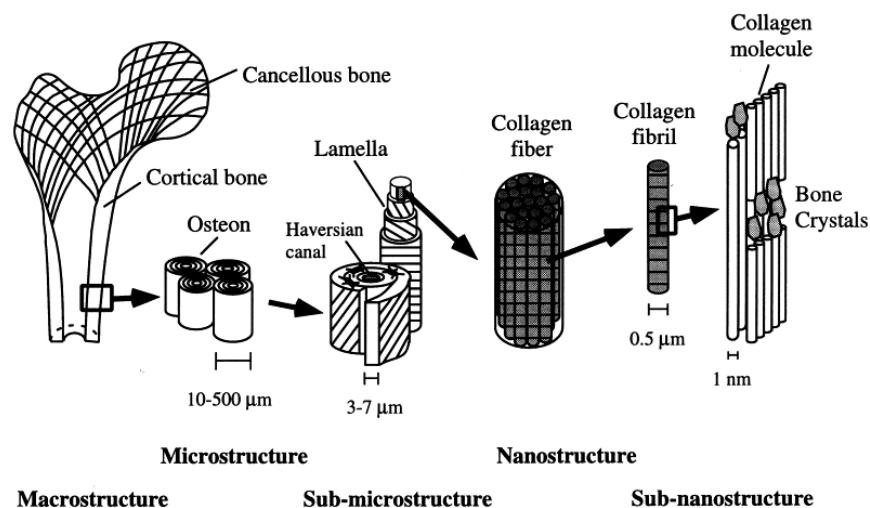


Figure 2-1. Hierarchical structural organization of bone with different levels and structures. Reprinted with permission from [47].

Bone has physical and physiological functions. Its physical functions include supporting the body, operating as a lever system during movement, and protecting organs from shock and injury. From a physiological point of view, bone functions are hematopoiesis, source of progenitor cells, and mineral homeostasis [44]. At the macroscopic level, a mature bone is divided into the cortical (compact) and the trabecular bones (also known as cancellous or spongy bone), which differ in density and microstructure (Figure 2-2) [47].

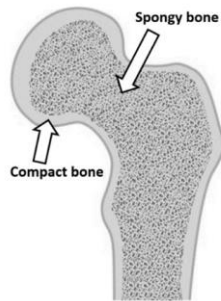


Figure 2-2. Trabecular (spongy) and cortical (compact) bone tissues differ in their microarchitecture and porosity. Reprinted with permission from [48].

Cortical bone has a compact structure with 10% porosity and constitutes 80% of the whole bone mass found in the skull, iliac crest, long bone diaphysis, and the shells of vertebrae and other bones containing relatively large amounts of cancellous bone [49]. The primary function of cortical bone is to give structural support and protection to the skeleton framework [44][45]. Osteons (Haversian systems) are the main structural unit of the cortical bone, cemented to one another but separated by interstitial and circumferential lamellae [50]. Each osteon contains a longitudinal central canal, the Haversian canal, that houses nerves and blood vessels supplying the bone with nutrients. Haversian canals are connected to one another, to the blood supply and bone marrow cavity by Volkmann's canals. [49]. The cylinder-shaped layers of the osteons, called concentric lamellae, are composed of a calcified matrix (collagen fibers and impure hydroxyapatite) (Figure 2-3-a). There are also circumferential lamellae that run along the periosteum. It covers the outside of bones, along the endosteum, which lines the inner spongy bone tissue and the interstitial lamellae between osteons. Osteocytes are imprisoned in small space called lacuna. The lacunae in the central canal are connected to each other through small canals called canaliculi, to provide

intercellular communication and nutrient delivery to the osteocyte cells. The trabecular bone constitutes the remaining 20% of bone mass and can be found in the inner part of the cortical bone, the long bone ends, the iliac crest, and the vertebrae and ribs. Spongy bone has a lattice-like matrix network called trabeculae surrounded by the bone marrow. The trabecular bone is less dense and more porous, with a higher concentration of blood vessels than compact bone. The trabeculae are thin rods made up of parallel lamellae composed of bone matrix, osteocytes and canaliculi and covered by endosteum (Figure 2-3-b) [44] [45][49].

Microscopically, bone is classified into two phenotypes; woven and lamellar bone [50]. Woven bone is immature, newly deposited bone or primary bone tissue found in the embryonic development stages and young children. It is composed of randomly oriented and disorganized collagen fibers. Lamellar bone is a mature bone composed of highly organized collagen fibers oriented in concentric sheets termed lamellae (Figure 2-4) [44][47].

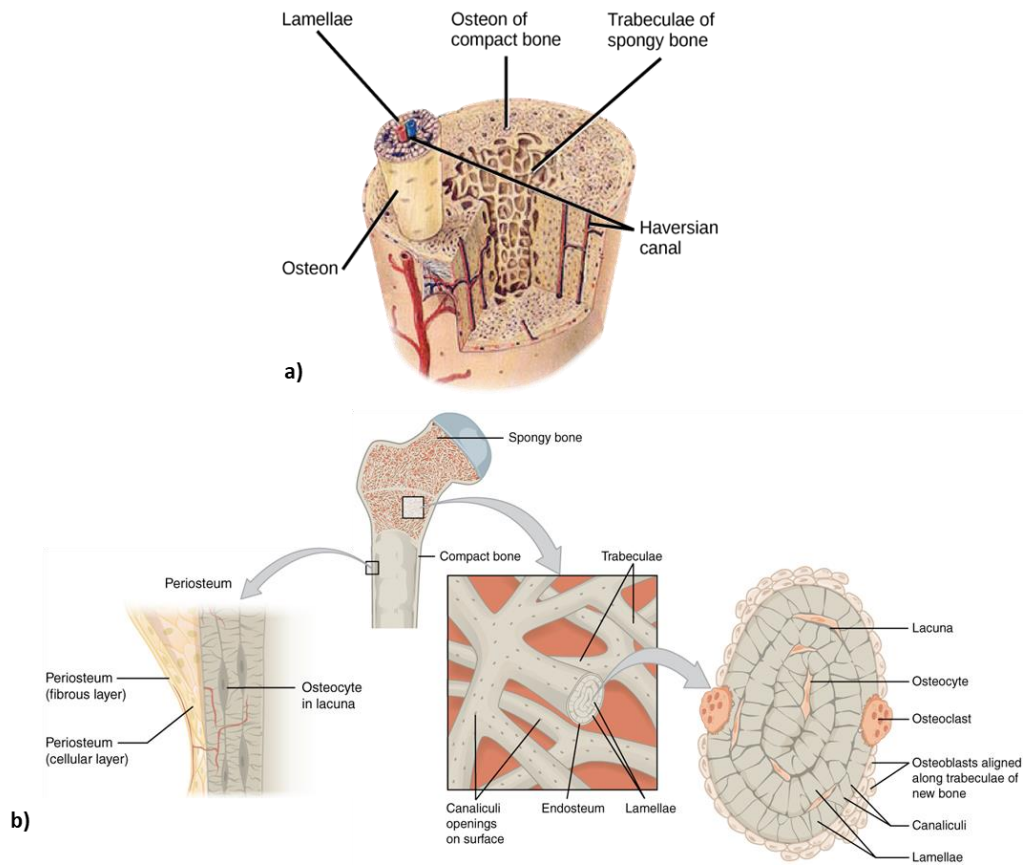


Figure 2-3. Illustration of structure of cortical and cancellous bone. a) components of compact bone [51], and b) spongy bone, periosteum, and endosteum [52]. License: [CC BY: Attribution](https://creativecommons.org/licenses/by/4.0/).

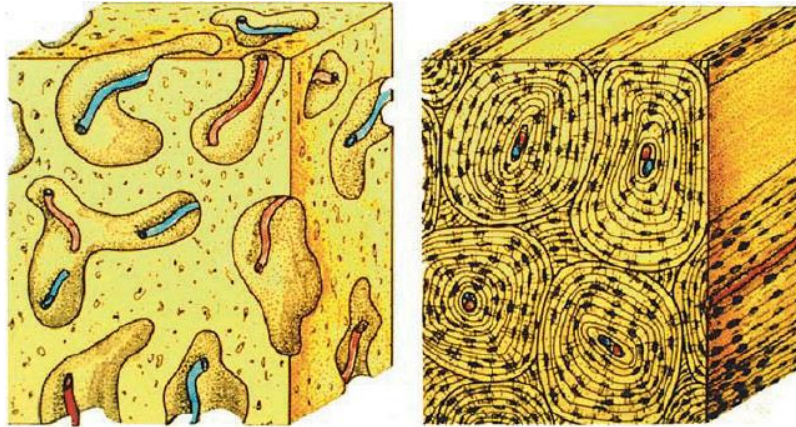


Figure 2-4. Diagram of immature bone (Woven) and mature bone (Lamellar). Reprinted with permission from [53].

2.2 Bone cells

Bone comprises four cell types: osteoblasts, osteoclasts, osteocytes, and osteoprogenitor (or osteogenic) cells (Figure 2-5) [54]. Each cell type has a unique function and is found in different locations in bones. The osteoblast is found in the periosteum (outer surface of the bone), endosteum (inner surface of the bony tissue), and inside osteons, it is responsible for depositing bone matrix and forming new bone [51][54]. When osteoblasts get trapped within the calcified matrix (mineralized bone), their phenotype changes, and they mature and become osteocytes [51][54]. The osteocyte is the primary cell of mature bone and the most common type of bone cell responsible for maintaining the mineral concentration of the matrix and sensing and responding to strains [51][54]. These cells are located in lacuna and connected for intercellular communication and nutrient delivery via canaliculi [51][54]. Mature osteoblasts and osteocytes do not divide, so the osteogenic cells located in the periosteum and the marrow are responsible for replenishing them [51][54]. Osteogenic cells are immature and undifferentiated bone cells that develop into osteoblasts. The last cell type is the osteoclast, a multinucleated cell responsible for bone resorption [51][54].

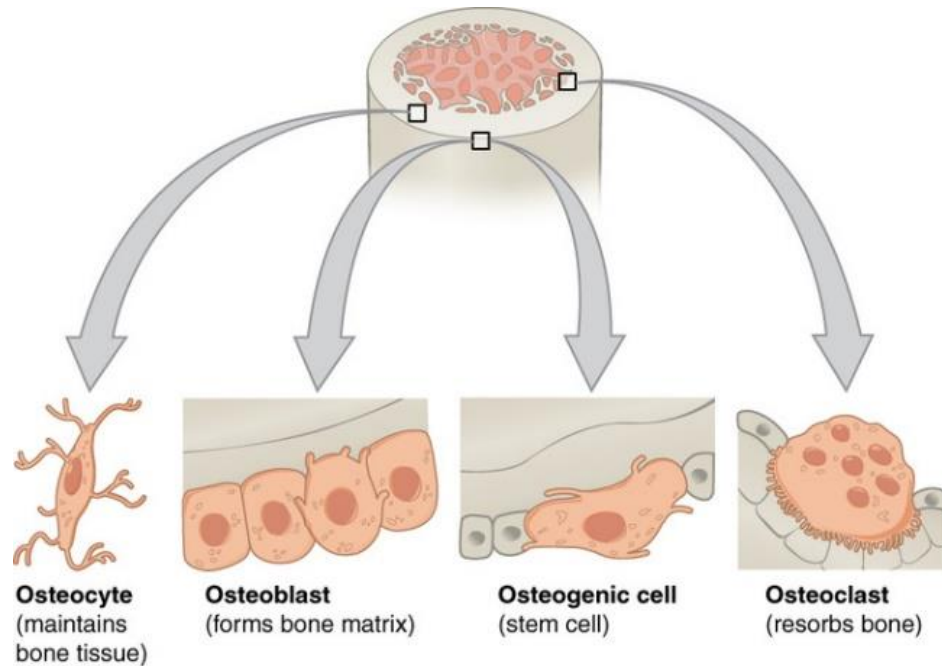


Figure 2-5. Four types of cells are found within bone tissue. Reprinted with permission from [51].

2.2.1 Osteoblasts: Osteoblastogenesis and bone formation

Osteoblasts are cuboidal cells that constitute 4-6% of the total resident human bone cells [55] derived from mesenchymal stem cells (MSCs) found in bone marrow [56]. A sequential cascade of biological processes drives the osteogenesis process (bone formation). This sequence is started by migrating MSCs to bone remodeling sites followed by proliferation, lineage commitment, expression of lineage-specific markers, collagen secretion, and extracellular matrix (ECM) mineralization [57]. This process is briefly explained below (for more details, please refer to [58][59]).

First, MSCs are committed to osteoprogenitors. Then, the generated osteoprogenitors are differentiated into osteoblastic lineage via the expression of transcription factors RUNX2 [60]. RUNX2 is a key component in the osteogenesis process that upregulates osteoblast-related genes such as alkaline phosphatase (ALP), osteocalcin (OCN), and bone sialoprotein (BSP) [59][61]. Osteoprogenitors proliferate into pre-osteoblasts which do not secrete ECM and do not show ALP activity. They continue differentiation into non-proliferating and matrix-producing mature osteoblasts. The first deposited and unmineralized ECM is known as “osteoid”, made up of type I collagen, non-collagen proteins (osteocalcin, osteopontin, bone sialoproteins), proteoglycans, and bone morphogenetic proteins [45][59]. Osteoblasts release enzymes

that breakdown the proteoglycans, and as a result, calcium ions (previously immobilized by the proteoglycans) are released from proteoglycans. Additionally, ALP secreted by osteoblasts degrades phosphate-containing compounds, and consequently, phosphate ions are released [58]. The accumulation of calcium phosphate in the form of hydroxyapatite leads to mineralization of the osteoid, resulting in a hard but lightweight material that makes bone [59]. Mature osteoblasts have different fates: apoptosis, bone lining cells, or osteocytes (Figure 2-6) [60]. Osteocytes are the main mechanosensitive skeletal cell type, and bone lining cells are flat osteoblast lineage cells lining the bone surface [59][62].

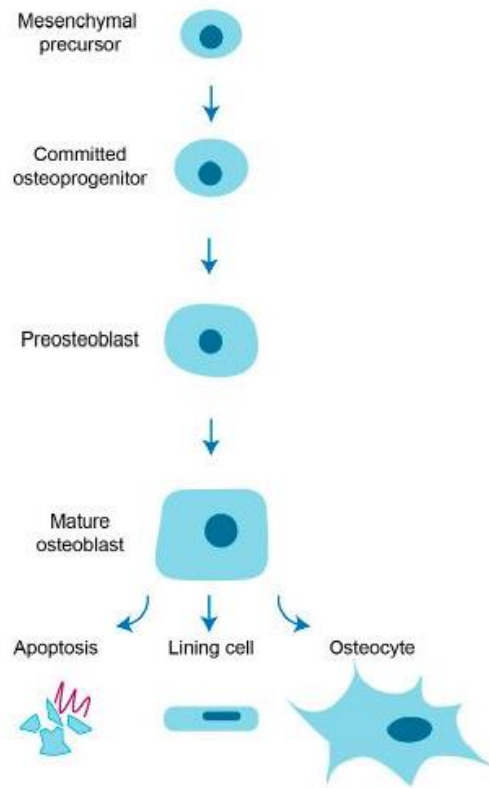


Figure 2-6. Strategies of osteoblastogenesis. Reprinted with permission from [60].

2.2.1.1 Experimental model to study osteoblasts in-vitro

Human primary cells are isolated directly from bone marrow to be used *in vitro* for osteogenic differentiation [63]. Although these cells maintain their origin tissue's morphological and functional characteristics, they do not live forever, have limited sources (from the same donor) and ability for self-

renewal and differentiation. Also, the donors' genetic characteristics and age might cause different cell behaviors under the same culture conditions. These cells are more sensitive than immortalized cell lines, cells that have been manipulated to grow indefinitely and can be cultured for longer periods of time. Primary cells usually need special media, additional nutrients, and growth factors. Since the early 20th century, immortalized cell lines have been used as a powerful tool to study biological processes and perform preliminary screenings or primary investigations such as cytotoxicity [64]. These cell lines are cost-effective, widely available, easy to work with, stay alive for longer periods, and lead to higher experimental reproducibility [64][59].

The undifferentiated preosteoblastic cell line MC3T3-E1 is the standard *in vitro* model of osteogenesis and has been widely used in transcriptional regulation, mineralization, and bone tissue engineering [65]. The MC3T3-E1 cell lines are differentiated to mature osteoblasts by specific reagents such as ascorbic acid 2-phosphate, β -glycerophosphate, and melatonin [65]. The differentiation can be confirmed by alizarin red staining, which identifies calcium deposition by osteoblasts. Alkaline phosphatase (ALP) is a byproduct of osteoblast activity considered a hallmark of the osteoblast phenotype and widely recognized as a biochemical marker for new bone formation [66][67]. Therefore, ALP expression is an early marker for osteogenesis. It can be detected by reacting with a p-nitrophenylphosphate chromogenic substrate [66].

2.2.2 Osteoclasts: Osteoclastogenesis and bone resorption

Osteoclasts play a crucial role in bone growth, bone remodeling, and bone healing by degrading and demineralizing the bone matrix. They are also critical actors in regulating calcium homeostasis by releasing calcium into the bloodstream [44][68]. Osteoclasts are giant and multinucleated cells derived from hematopoietic stem cells, with 2 to 30 nuclei, and varying in diameter between 10 and 300 μm (Figure 2-7) [69][70]. In the formation of osteoclasts, two cytokines play vital roles: macrophage colony-stimulating factor (M-CSF) and receptor activator of nuclear factor- κB ligand (RANKL) [58]. Briefly speaking, hematopoietic stem cells within the bone marrow give rise to macrophage progenitors under the influence

of M-CSF. M-CSF is primarily responsible for the proliferation and survival of osteoclast precursors produced by the adjacent bone marrow stromal cells and osteoblasts [71][72]. The M-CSF binds to its receptor in osteoclast precursors, cFMS, and then this combination stimulates precursor cells' proliferation and prevents their apoptosis [73]. Osteoclast precursor cells are positive for tartrate-resistant acid phosphatase (TRAP), an enzyme indicative of osteoclast activity. Then, the binding of RANKL to its receptor on osteoclast precursors, RANK, induces a signaling cascade leading them to differentiate into mononucleated osteoclasts and subsequently fuse to become multinucleated osteoclasts [71]. RANKL is an essential factor for osteoclastogenesis and is expressed by bone marrow stromal cells, osteoblasts, and osteocytes [58]. The resultant multinucleated osteoclasts resorb bone matrix by secreting protons (H^+), proteases (e.g., Cathepsin K), and matrix metalloproteinases (MMPs).

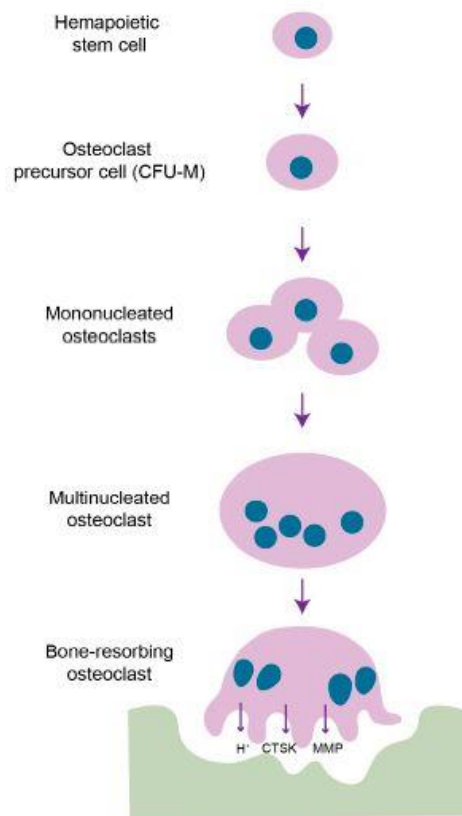


Figure 2-7. Osteoclastogenesis pathway. Reprinted with permission from [60].

Bone resorption is the demineralization and degradation of inorganic and organic components of bone by osteoclasts, respectively. The mechanism of bone resorption is shown in Figure 2-8. Osteocytes recruit osteoclasts to the resorption site by detecting skeletal microdamage or for regulating mineral homeostasis [58]. The migration of osteoclast precursor from the circulation into bone or within the bone cavity is controlled by several chemokines such as Cxcl9 [74][75]. Osteoclasts are normally attached to the surface of the bone. Their function depends on the tight connection to the bone matrix (formation of resorption pit/sealing zone) and osteoblast-like cells (activation of RANK via interaction with osteoblast-derived RANKL) [76]. The plasma membrane of the osteoclast attaches to the bone through the binding of $\alpha_v\beta_3$ -integrin to proteins, including osteopontin and bone sialoprotein (BSP) [58]. This attachment creates the resorption compartment, a closed and sealed microenvironment between the osteoclast and the bone. Then, osteoclasts develop several invaginations called “ruffled border” on their plasma membrane facing the bone to be resorbed. The ruffled border helps the process of digestive enzyme delivery and the creation of an acidic environment. The hydrogen ions (protons) are derived from carbonic anhydrase in the cell's cytoplasm and pumped into the resorption compartment via proton pumps [77]. Chloride ions (Cl^-) are also transported into the resorption compartment via chloride channels to maintain electroneutrality. The secretion of hydrogen and chloride ions creates an acidic environment, leading to the dissolution of hydroxyapatite and the exposure of the organic matrix [76]. The organic and inorganic matters of the bone matrix are digested by the action of several enzymes like tartrate-resistant acid phosphatase, cathepsin K, and matrix metalloproteinases [78]. These enzymes are formed in the cytoplasm of osteoclasts and packaged into vesicles to be released via the ruffled border into the resorption lacunae. When the matrix is digested, shallow depressions called “Howship’s lacunae” are created. Following resorption, degraded products are endocytosed via the ruffled border, packed into vesicles, and released extracellularly by exocytosis through the membrane opposite the ruffled border. After completion of the resorption, osteoclasts undergo apoptosis [59].

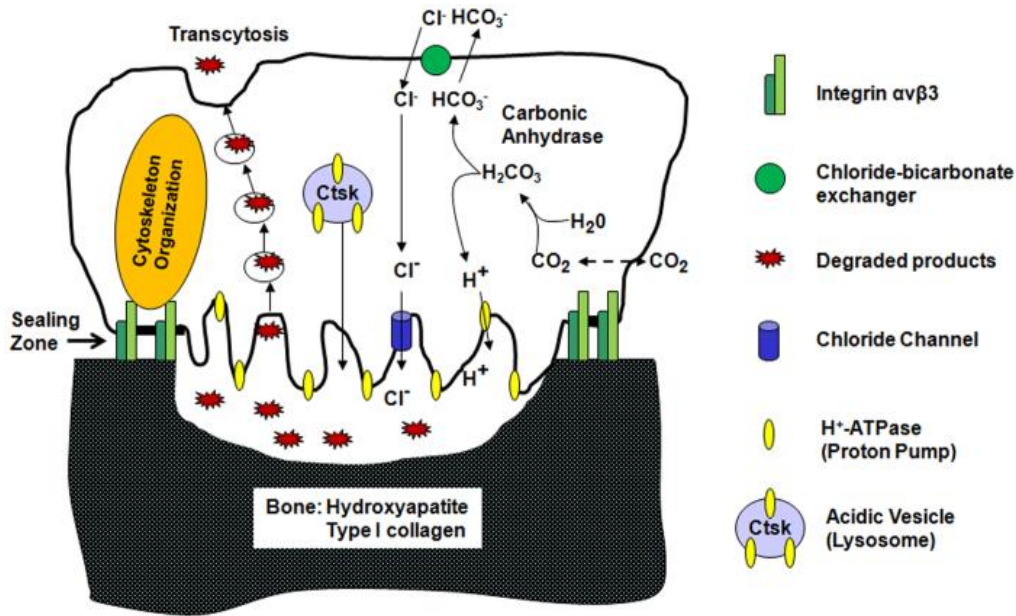


Figure 2-8. Mechanism of bone resorption. Ctsk: cathepsin K. Reprinted with permission from [77].

2.2.2.1 Experimental model to study osteoclasts in-vitro

Identification of RANKL and M-CSF made a revolutionary change in the generation and study of osteoclasts. These two cytokines allow researchers to generate osteoclasts *in vitro* in the absence of other cell types. A variety of cell populations, including adult mouse bone marrow cells and mouse/human peripheral blood mononuclear cells, can be differentiated into osteoclasts [79]. Like osteoblasts (see section 2.2.1.1), osteoclasts can be generated from immortalized cell lines such as the RAW 264.7 murine macrophage cell line rather than primary cells [80]. Using RAW264.7 cells removes the necessity of treatment with M-CSF since these cells express both M-CSF and its receptor c-fms. Therefore, supplementing the culture medium with RANKL is sufficient to differentiate RAW 264.7 cells into mature osteoclasts [79][81]. The differentiated RAW 264.7 cells can then be cultured on bone tissue or biomaterials to assess resorption *in vitro* [79].

Three features usually distinguish the presence and activity of osteoclasts: multinucleated cells, TRAP expression, and the bone/biomaterial resorption ability [82]. The osteoclast phenotype is confirmed by staining the nuclei (labeling DNA), and osteoclast activity is detected by TRAP expression and osteoclast-mediated resorption pits (Rpits) [79]. Most research on the resorbing activity of osteoclasts has

been restricted to 2D qualitative analysis using different staining methods [83]. For example, multinuclear cell morphology, TRAP activity, and the number and area of formed resorption pits on bone or dentine surfaces have been stained with histochemical or immunological staining and studied by reflective microscopy [84][85]. Osteoclastic bone resorption happens in 3D *in vivo*. So, it is essential to evaluate resorption pits in 3D using advanced methods like scanning electron microscopy, confocal microscopy, and atomic force microscope (AFM) [86]–[89]. Confocal microscopy is a three-dimensional method that can be used for measuring surface topography over a wide range of size scales, making it possible to characterize resorption pits geometry precisely in 3D [68][90].

The primary function of osteoclasts is bone resorption, and its microscopic measurement is the most widely used approach [91]. Once osteoclasts are cultured on bone resorbable biomaterials *in vitro*, resorptive lacunae (Rpit) are formed similarly to those created during bone resorption *in vivo*. The number and size (length, width, and depth) of Rpits determine a biomaterial's resorbability by osteoclasts *in vitro* [92]. It was found by Hefti *et al.* that the size of resorption pits in native bone and titanium and zirconia surfaces were quite similar in size [93]. According to a study by Arnett and Dempster, pits were stained by toluidine blue and then identified and quantified by a simple microscope with bright-field illumination [94]. However, this approach can only be used for bone slices or biomaterials containing proteins like collagen molecules. Toluidine blue cannot be used to stain calcium phosphates, making it challenging to observe resorbed areas on certain biomaterials that do not contain collagen [91].

Although the volume of resorption pits in bone indicates the work done by osteoclasts, the plane area of the pits has mostly been used to quantify the work by osteoclasts [95]–[99]. Some authors have claimed that measuring plane area is not a reliable indicator for the extent of resorption and have emphasized the need for or advantages of volumetric measurements [100]–[102]. As such, Stereomorphometry of SEM images have been used to determine the volume of resorption pits [103]. Yamada *et al.* showed that the area, depth, and volume of resorption pits could also be assessed accurately by a 3D laser scanning microscope. They compared the resorption capacity of mature osteoclasts on

tricalcium phosphate (TCP) and zinc-containing TCP (ZnTCP) and demonstrated that there was a significant difference in pit volume for two different biomaterials with the same pit area [104].

2.3 Bone remodeling

Synthetic bone graft materials must be resorbable and support the ingrowth of bone tissue. A material impermeable to cellular infiltration leads to a slower rate of resorption and new bone formation. The use of allografts shows that dense tissue can undergo extensive osseous integration by osteoclasts and osteoblasts [105]. Thus, a bone graft substitute should be designed to slowly integrate into the skeleton via controlled remodeling. Bone remodeling is a continuous process where old or damaged bone tissue is removed by osteoclasts and replaced with new bone tissue formed by osteoblasts [60]. The remodeling rate varies based on areas of the skeleton and also areas of a bone. For example, the cortical bone along the long bone shaft is altered at a much lower rate than the bone on the femur's head [51]. In adults, there is about 10% of bone tissue remodeling each year [106]. Remodeling takes place to help reshape and heal bone tissue after a fracture, repair micro-cracks due to normal activities, and supply calcium and minerals to other tissues as demand arises [107][106]. In the following paragraph, the bone remodeling process is described as well as in Figure 2-9.

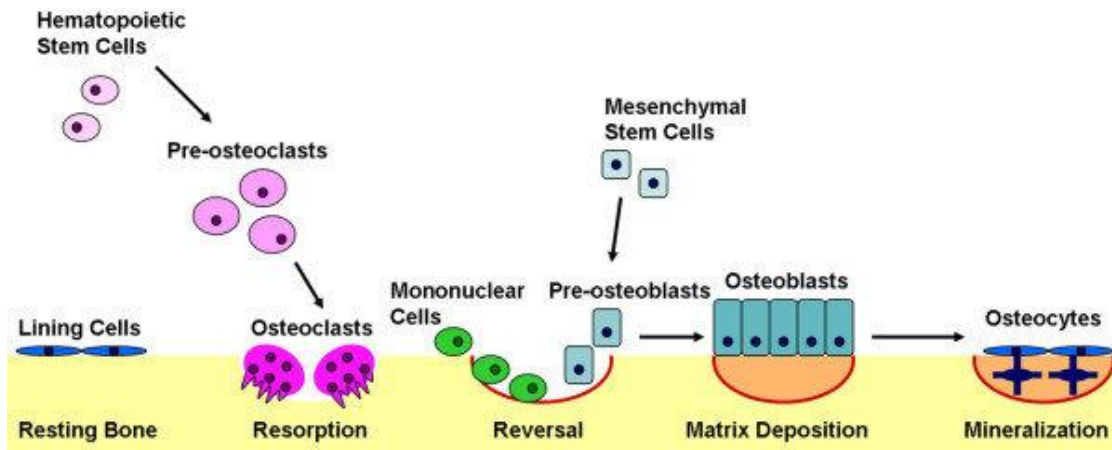


Figure 2-9. The bone remodeling process. Reprinted with permission from [108].

The first step is the activation of osteocytes induced by changes in mechanical forces, calcium homeostasis, or hormone levels [106]. Next, the remodeling cycle is initiated and has three phases: bone

resorption, transition or reversal, and bone formation [58]. Osteoclast progenitors are recruited to the damaged-bone surface/degradation site in the resorption phase [60]. Subsequently, these cells make the local environment acidic, and the minerals are dissolved, as described in section 2.2.2. As a result, resorption cavities are formed with depth varying between 40-60 μm . When a certain amount of bone is resorbed, the reversal phase starts, where bone resorption stops, osteoclasts begin to die, and osteoblast progenitors are recruited [60][106][109]. Direct and indirect communications between mature osteoclasts and osteoblasts have been reported to occur during the reversal phase [58]. Molecules called semaphorins and ephrins are involved in these communications, but the direct contact between these two cells has not been demonstrated *in vivo*, and it is still an area of controversy [58][110][111]. For more details regarding the mechanisms involved in the reversal phase and osteoblast/osteoclast communication, refer to [58][60][112]. The completion of the first two phases mentioned above takes roughly 2-3 weeks [106]. In the last phase (formation phase), mature osteoblasts produce a new bone matrix (osteoid) that fills the resorption cavities [113]. The bone remodeling phase completes by matrix mineralization and the differentiation of some osteoblasts into osteocytes. This step continues for months and results in dense mineralized bone tissue [106].

Bone remodeling in cancellous bone happens on the trabeculae surface and takes about 200 days in normal bone. On the other hand, the cycle duration is shorter in cortical bone, with a median of 120 days [109]. Remodeling is triggered by osteoclastic resorption, which erodes a resorption lacuna with a depth of 60 μm in young people and 40 μm in elderly people per day [109]. Cortical bone has a lower surface-to-volume ratio; so, the resorption proceeds in tunnels (osteonal remodeling) through the bone itself [109]. It is worth mentioning that during normal bone remodeling, a balance between bone resorption (removal of calcified tissue) and bone formation is controlled by several coordinated signaling mechanisms (signaling, antiresorptive, and anabolic pathways [114]) to couple formation to resorption [115]. This balance is maintained in the mature, healthy bone to ensure no significant net changes in bone mass or mechanical strength happen after each remodeling cycle. Imbalance may occur under certain pathological conditions

resulting in abnormal bone remodeling and the development of bone disorders (e.g., osteoporosis) [115]. The remodeling process is also active during the healing of injured bone, explained in the following section.

2.4 The bone fracture healing mechanism

Bone fracture is a medical condition caused by sports, accidents, falls, or osteoporosis, and is characterized by the loss of bone anatomic continuity and mechanical stability [49]. There are two types of fracture healing: direct (primary) healing and indirect (secondary) healing [49]. Direct bone healing occurs when the fracture gap is less than 0.1 mm, and the fracture site is stabilized [116]. There is no vascular disruption and no callus formation in direct bone healing [49]. Inflammation activates a process of continuous ossification, which directly produces a new lamellar bone structure to fill the bone gap and subsequent Haversian remodeling [116].

Indirect bone healing is more common and happens when the fracture gap is less than twice the diameter of the injured bone [117]. Once the fracture happens, the bone healing process starts immediately [118]. Four stages are involved in the secondary bone fracture healing as illustrated in Figure 2-10 [51]: hematoma formation followed by inflammation, soft callus formation (initially granulation tissue followed by fibrocartilage formation and mineralization of cartilage), hard callus formation (formation of woven/trabecular bone), and bone remodeling (reestablishment of cortical bone by cutting cone formation of osteons) [49][51][118]. A variety of cellular components is also required for the bone healing process [119]. In the following paragraphs, the indirect bone healing process is explained in more detail.

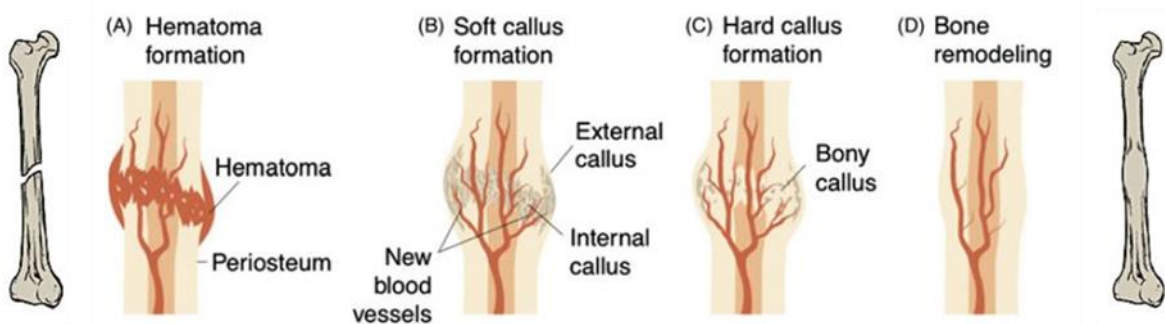


Figure 2-10. Illustration of the four stages of the bone healing process. Reprinted with permission from [120].

Immediately after the fracture, an hematoma (collection of blood, most often clotted) is formed because of the tear in blood vessels [119]. The hematoma is enriched with bioactive molecules such as bone morphogenetic protein and coagulation and inflammatory factors for platelet activation and recruitment of inflammatory cells (macrophages and neutrophils), neovascularization, fibroblasts, and osteoprogenitor cells [118]. As seen in Figure 2-10, the hematoma acts as a sealing zone covering the affected area. Platelets, macrophages, osteoclasts, and various inflammatory cells penetrate the sealing zone and secrete cytokines and growth factors [118][119]. Macrophages and osteoclasts in the hematoma help remove degenerated cells, injured and devitalized tissue, and other debris [49][119].

The second stage is the soft callus formation, where both chondrocytes and fibroblasts form granulation tissue and fibrocartilage [118]. The fibrocartilage fills the space between the broken ends and holds them together [118]. In this phase, mesenchymal stem cells are recruited to regenerate vasculature and differentiate into osteoblasts to initiate bone formation [49][119]. This is followed by the third stage, hard callus formation, where an increase in osteoblast activity and mineralized matrix formation takes place. As a result, the soft callus is gradually transformed into a hard callus, and consequently, woven bone is formed [118].

In the last phase (bone remodeling), which can take several months, woven bone is degraded by osteoclasts and replaced with mature lamellar bone laid down by osteoblasts. The process is continuous until the bone has been fully remodeled to new bone indistinguishable from uninjured tissue [118][121]. As explained, bone can regain full functionality after injury (minor fractures) due to the physiological healing process and its regeneration ability (self-repair and self-remodeling ability). However, there are conditions such as large segmental defects where the bone fails to heal, defined as “non-unions”.

2.5 Critical-sized segmental bone defect and current treatment

Bone defects resulting from severe traumatic injuries and large bone resection for various pathologies are challenging in the orthopedic field due to the limited regenerative capacity of bone in such defects [44][122]. The critically-sized segmental bone defect (CSBDs) is defined as the smallest osseous

defect in a particular bone that does not heal spontaneously over a long period of time [123]. The minimum size that renders a defect “critical” has been defined as a segmental bone deficiency of a length exceeding 2-2.5 times the diameter of the affected long bone [124]. In addition to surgical and research challenges, the non-union caused by such defects can lead to prolonged and postoperative treatment costs and affect the quality of patients’ lives [125].

Bone grafting is a key solution for significant bone defects that fills the defect’s space, provides mechanical support, and enhances the defect's biological repair [126]. Autograft has been considered the gold standard for bone defect healing due to possessing most requirements, including osteoconductivity and osteoinductivity for successful bone regeneration [127]. However, an autograft is associated with donor site morbidity. It also has the disadvantage of prolonged surgical and anesthesiological time that can cause a proportionally increased risk of infection [127][128]. Autograft is not commonly used to reconstruct CSBDs. The treatment of CSBDs, which is required to prevent amputation, has changed over the years [129]. The current standard solutions for CSBDs reconstruction are allografts-based structure and metal alloy mega-prostheses.

Allografts obtained from human cadavers are good alternatives to autografts, constituting about 34% of the bone substitutes [12][126]. They are relatively easy to obtain, avoid donor-site morbidity, show optimal osteoconductivity and biomechanical characteristics due to their three-dimensional structure similarity with the human bone [126]. However, allografts are usually not osteoinductive or osteogenic, are associated with risks of immunogenicity, viral disease transmission, and bacterial infection. This leads to inadequate mechanical properties for load-bearing bone applications due to the lack of remodeling and repair, which leads to microcracks and eventually fatigue failure [126]. Allograft’s quality is highly dependent on donor characteristics leading to the variability in clinical results [44][126]. The failure rate of allografts has been reported in the range of 25% and 35% in the literature [130][131].

Metal alloy mega-prostheses for CSBDs reconstruction have been used more frequently in the last three decades to replace the affected bone tissue instead of regenerating bone tissue (Figure 2-11) [129]. Their components have been developed to resist corrosion, avoid fractures, and present better fixation

[129][132]. Despite the advances in materials and implant designs, megaprotheses have complications and a high failure rate [133]. The complication rate for megaprotheses has been reported to be between 25% and 92% [134][135][136]. Aseptic loosening, mechanical failure, and infection are factors causing the high incidence of complications [5][19]. According to the literature, infection is the most common mode of failure in megaprotheses, ranging between 5% and 40% [133]. The complications associated with autografts, allografts, and metal mega-protheses for critical defects have identified a need for new approaches. [12]. In the next section, the required properties for bone biomaterials and composites as suitable biomaterial for bone defect reconstruction are explained.

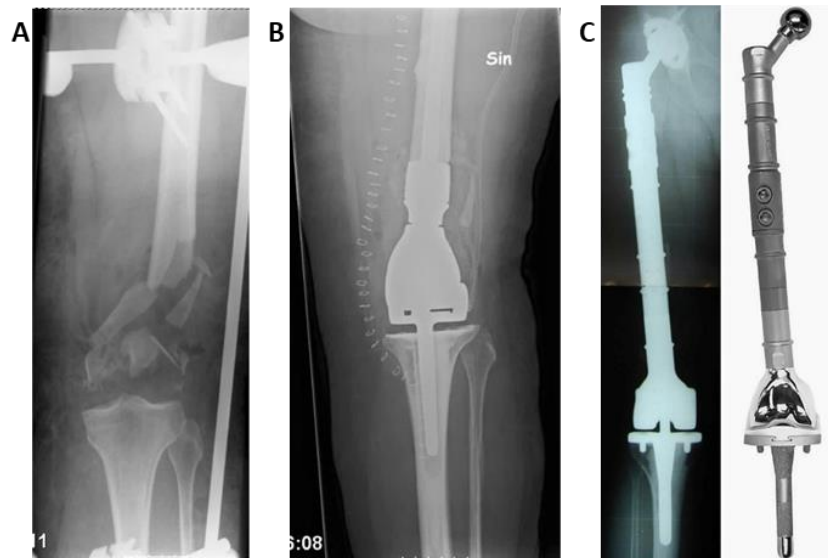


Figure 2-11. A: Fracture of the distal femur after a road traffic accident, B: Distal femur reconstruction with megaprosthesis. Reprinted with permission from [137], C: Implantation of a total femoral prosthesis after resection of the tumor. Reprinted with permission from [5].

2.6 Biomaterials for bone reconstruction

2.6.1 Required properties for bone biomaterials

Due to the mentioned limitations, considerable work has been conducted toward developing synthetic bone graft materials. Alternative biomaterials must be compatible with bone cells, support cellular attachment and proliferation, be resorbable, and support the ingrowth of new bone tissue. Furthermore, biomaterials should mainly provide the combination of mechanical support and osteo-regeneration [138], which involve four significant biological properties: osteoinductivity, osteoconductivity, osteogenicity, and

osseointegrativity [139]. The biomaterials should possess mechanical properties comparable to natural bone and have similar strength to the replaced bone [140]. Biomechanical properties of cortical and cancellous bones are shown in (Table 2-1) [31]. The biomaterials should support the attachment and migration of new osteoblasts and osteoprogenitor cells (osteoconductivity), in situ mineralization of the collagen matrix produced by osteoblasts to form new bone (osteogenicity), the recruitment and differentiation of osteoprogenitor cells into osteoblast (osteoinductivity), and the formation of intimate bonding between the newly formed mineralized tissue and host bone (osseointegrativity) [126][127].

Table 2-1: Biomechanical properties of bone. Reprinted with permission from [31].

Properties	Measurements	
	Cortical bone	Cancellous bone
Young's modulus (GPa)	14-20	0.05-0.5
Tensile strength (MPa)	50-150	10-20
Compressive strength (MPa)	170-193	7-10
Fracture toughness (MPa.m ^{1/2})	2-12	0.1
Strain to failure	1-3	5-7
Density (g/cm ³)	18-22	0.1-1
Apparent density (g/cm ³)	1.8-2.0	0.1-1.0
Surface/bone volume (mm ² /mm ³)	2.5	20
Total bone volume (mm ³)	1.4 × 10 ⁶	0.35 × 10 ⁶
Total internal surface (mm ²)	3.5 × 10 ⁶	7.0 × 10 ⁶

Therefore, a synthetic biomaterial for bone graft substitutes should allow cell adhesion, migration, proliferation, and differentiation to enhance bone defect healing [141]. Moreover, it should bring desired mechanical properties while resorption is balanced with bone formation without spontaneous degradation [31]. Quick material degradation could result in mechanical failure. On the other hand, if it does not degrade quickly enough, mechanical failure could occur or an inflammatory response could be stimulated, which impairs tissue regeneration [142]. In other words, ideally, the mature bone should replace the bone substitute without transient loss of mechanical support and stability [7].

Bone implants are commonly made of metals, ceramics, polymers and their composites (see Table 2-2). Metals are great candidates for load-bearing orthopedic applications because of their excellent mechanical properties, compressive strength, and fatigue resistance [143]. However, they are known as

non-bioactive materials with no osteoinductivity and osteoconductivity [49]. Also, insufficient interfacial bonding between the metal and host tissue limits the osseointegrativity and leads to aseptic implant loosening [31][144]. Although metal implants exhibit adequate mechanical properties, their application is limited due to their stiffness and non-biodegradability [31]. Conventional biomaterials are inadequate for CSBD reconstruction because they cannot sustain the combined loading experience by natural bone while aiding in new bone formation [2]. Recent studies have shown that dense, osteoconductive, bone-inspired nanocomposite biomaterials might be a potential and promising alternative approach for CSBD reconstruction [29][145]. In the following section, nanocomposite biomaterials are reviewed in more detail.

Table 2-2: Biomaterials' classification for bone applications. Adapted with permission from [31].

Biomaterials	Advantages	Disadvantages	Applications	Examples
Metal and alloy	Strong and often ductile	Too stiff, Dense, may corrode	Bone plates, load-bearing bone implants, dental arch wire, and dental brackets	Titanium, stainless steel, Co-Cr alloys, and Ti alloys
Ceramic	Bioinert Bioactive Bioresorbable High resistance to wear	Brittle, poor tensile strength	Hip joints and load-bearing bone implants Bone filler, coatings on bio-implants, orbital implant, alveolar ridge augmentation, maxillofacial reconstruction, and bone tissue engineering	Alumina, zirconia HA, bioglass, TCP
Polymer	Flexible, resilient, surface modifiable, selection of chemical functional groups	Not strong, toxicity of some degradation products	Bone tissue scaffolds, bone screws, pins, bone plates, bone and dental filler, and bone drug delivery	Collagen, gelatin, chitosan, alginate, PLA, PGA, PLGA, PCL, PMMA, PE
Composite	Strong, design flexibility, enhanced mechanical reliability than monolithic materials		Bone graft substitutes, middle ear implants, bone tissue scaffolds, guided bone regenerative membranes, and bone drug delivery	HA/collagen, HA/gelatin, HA/chitosan, HA/alginate, HA/PLGA, HA/PLLA, HA/PE HA/PEEK
Nanocomposite	Large surface area, high surface reactivity, relatively strong interfaces	No optimized technique for material processing	Major areas of orthopedics, tissue engineering, and drug delivery	Nano-HA/collagen, Nano-HA/gelatin, Nano-HA/chitosan, Nano-HA/PLLA

2.6.2 Nanocomposite biomaterials

Single-phase materials do not necessarily have all the characteristics needed for bone grafting, and they are far from the properties of an actual autogenous bone graft. Composites are a combination of two or more materials that differ in morphology or composition [146]. In this approach, it is feasible to control the mechanical properties of composites closer to the natural bone by using a secondary substitution phase. Basically, inorganic-organic composites are inspired by the composite nature of natural bone. In particular, in such composites, the toughness of a polymer phase (organic phase) is combined with the stiffness and strength of an inorganic phase to produce bioactive materials with improved mechanical properties and degradation profiles [109]. Laurencin *et al.* [147] developed a bioresorbable HA/PLGA composite and demonstrated that the composite supported osteoblasts proliferation and differentiation suitable for bone tissue regeneration. In another study, Paxton *et al.* demonstrated that adding HA to poly (ethylene glycol) diacrylate (PEGDA) increased mechanical strength, cell attachment, and ability to form an interface with biological materials. Increase in HA content in hydroxyapatite-polyurethane (HA-PU) composite also enhanced cytocompatibility and osteogenesis capability [148]. However, incorporating high levels of HA also leads to composite brittleness [149].

Figure 2-12 presents a graphical representation of the relationship between toughness and modulus of HA-based composites compared to a natural bone, highlighting how the fracture toughness and elastic modulus of HA-polymer composites is comparable to that of human cortical bone. In this regard, Hydroxyapatite and polymer biomaterials, as components of composites for bone application, are described in more details below.

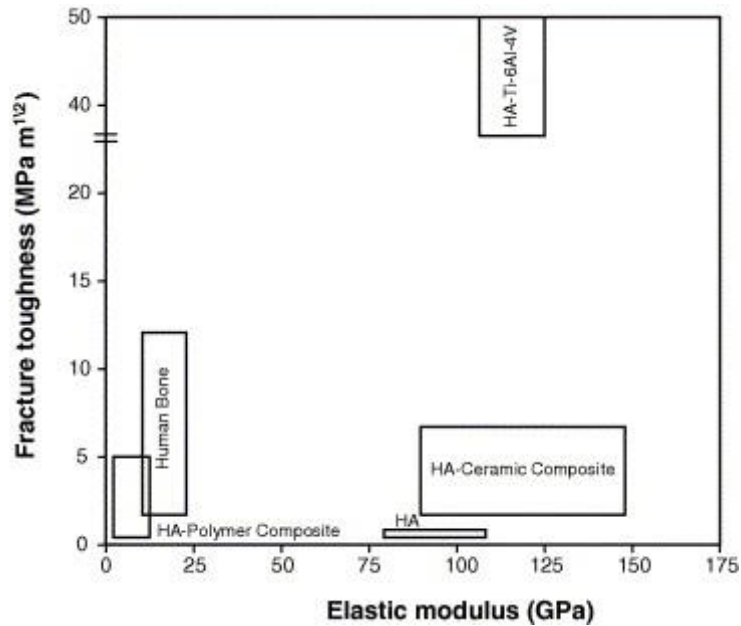


Figure 2-12. A graphical representation of relationship between toughness and modulus of various HA-based composite materials. Reprinted with permission from [150].

2.6.2.1 Hydroxyapatite

Calcium phosphate (Ca-P)-based materials are commonly used in orthopedic for their outstanding biocompatibility and bioactivity, specifically in the creation of cohesive bone bonding that results in effective and rapid osseointegration [151]. The mineral phase of the bone is mostly made up of microscopic crystals of calcium phosphates, in which the hydroxyapatite (HA) is the most important [152]. HA is one of the two calcium phosphate phases that is chemically stable at the human body's temperature and pH (37°C and around 7, respectively) [153].

Hydroxyapatite is a promising candidate for bone reconstruction because it is chemically comparable to the mineral component of mammalian bones [154]. The stoichiometric HA has a chemical composition of $\text{Ca}_{10}(\text{PO}_4)_6(\text{OH})_2$ with Ca/P ratio of 1.67. HA is biocompatible, has a high osteoinductivity, and is capable of bonding to bone tissue [155]. Non-cytotoxicity, non-inflammatory behaviour, non-immunogenicity, and direct bonding with new bone without the need for intermediate connective tissues are all appealing features of HA to be used in bone-related applications [153][155]. The main application of HA includes bone repair, filler to reconstruct bone defects (graft materials) [156][157], or coatings for implants [158][159] to promote bone ingrowth in orthopedic applications [150][160]. Despite the fact that

HA has been studied for clinical applications, it has not been used in cases where high load is applied because it is brittle, and it has mostly been used as coatings [161] [162]. Coatings on the surface of metallic implants, for example, have been developed to enhance the contact area of bone implants or to boost osteoblast activity [163][164]. In this way, HA coatings enhanced implant biological fixation, biocompatibility, and bioactivity of implants [166]. Various publications show that HA promotes bone formation by increasing cellular response [167]–[169]. Augmenting atrophic alveolar ridges, repairing long bone defects and ununited bone fractures, middle ear prostheses, spinal fusion, cranioplasty, craniofacial repair, and vertebral fusions are some of the few possible clinical uses for HA [31].

Recently, nanoscale HA (nHA, ~10-100 nm) has attracted much attention because of its enhanced functional properties, especially surface reactivity and ultra-fine structure, which are the most critical features for tissue-graft interaction upon implantation. During the past few years, nHA, compared to micro-HA, has been shown to promote osteoblast adhesion, differentiation, proliferation, osseointegration, and increase calcium-containing mineral deposition on its surface, resulting in enhanced new bone tissue formation in a shorter time [170]. Although HA is an outstanding bone graft material, its usage in some orthopedic applications has been limited due to its inherent low fracture toughness, particularly in heavy load-bearing situation [171]. To increase HA's reliability, it needs to be incorporated into new composite matrix materials with the appropriate mechanical properties, and intensive research is being conducted to develop HA-based composites with a polymer matrix material [31].

Some research studies have investigated the effect of incorporation of nHA into a polymer phase. An HA/collagen micro-composite was found to take longer to remodel into the bone and exhibited poor mechanical properties for load-bearing applications compared to its corresponding nanocomposite [172]. Jia Huang *et al.* showed that nano-hydroxyapatite-reinforced composites were bioactive and supported the growth and proliferation of primary human osteoblast cells [173]. In another study, Webster *et al.* reported that osteoblast proliferation was significantly greater on nHA after 3 and 5 days compared to conventional ceramics. More importantly, they observed that ALP synthesis and calcium-containing mineral deposition was significantly higher in osteoblasts cultured on nHA after 21 and 28 days [170]. In [174], Wei *et al.*

indicated that nano-HA/poly(lactic acid) (nHA/PLLA) composites had higher mechanical properties than their corresponding micro-composites and also provided a better substrate for attachment and migration of cells in bone tissue engineering. In [175], nano-HA/poly(amino acid) (nHA/PAA) effectively induced osteogenesis and led to the repair of long segmental bone defects *in vivo* in New Zealand White rabbits.

While all of these studies were performed with primary cells, other work has also used immortalized pre-osteoblast cell lines. Wang *et al.* developed 3D-printable GelMA-PEGDA-nHA composite hydrogel for bone defect repair and showed that the nanocomposite had good MC3T3-E1 cells' viability and proliferation [176]. Excellent biocompatibility was also observed with pre-osteoblast MC3T3-E1 cells interacting with bone-mimetic polysaccharide/nano-HA (nHCP/CG) composites [177]. However, while exhibiting excellent cell-material interactions, these composites hydrogels have poor mechanical properties, which make them unsuitable to replace bone.

Most of the research on nHA application in composites for bone applications has focussed on the interactions with cells of the osteoblast lineage. To the best of our knowledge, there is currently little literature available on osteoclast interactions with nHA-based composites. In 2017, Lu *et al.* developed nHA-poly (ester urethane) (nHA/PEUR) composites which had a strength comparable to non-resorbable PMMA bone cement and promoted bone healing at weight-bearing sites [29]. They also used a co-culture model with MC3T3 cells and RAW 264.7 cells and demonstrated that their composite not only promoted osteogenic differentiation but also showed signs of osteoclast-mediated resorption after 28 days as observed by SEM [29]. However, no controls without cells were presented which makes it difficult to clearly assess if the pits observed by SEM were osteoclast-mediated resorption pits and not material defects.

Although HA has excellent biocompatibility and bioactivity, the low fracture toughness and therefore tensile strength of HA compromise its use by itself for bone regeneration in structural applications [178]. In order to complement the limitations of HA, studies on bone regenerative applications have been conducted by mixing HA with soft materials such as polymers [161]. Several studies have found that combining HA with a biopolymer can significantly improve bone healing and HA's tensile strength [151], [155].

2.6.2.2 Polymers

Polymers are widely used as bone graft substitutes because of their biocompatibility, design flexibility, functional group availability, surface modifiability, lightweight, and ductile behavior [179][173]. Polymers can be either natural or synthetic. It is shown that natural polymers such as collagen, fibrin, gelatin, starch, hyaluronic acid, or chitosan exhibit good biocompatibility, biodegradability, and osteoconductivity [180][181]. This class of polymers is also bioactive since they can potentially interact with the host's tissue. They are often used in composites or chemically modified to increase their mechanical strength and reduce their high degradation rates [181].

On the other hand, synthetic polymers present great versatility since they can be synthesized with different porosities, pore sizes, degradation rates, and mechanical properties. The most commonly synthetic polymers used as bone grafts are poly-glycolic acid (PGA), poly-lactic acid (PLA), poly(lactic-co-glycolic acid) (PLGA), poly(caprolactone) (PCL), and poly(ethylene glycol) (PEG) [142]. Poly(ethylene glycol) diacrylate (PEGDA) is one of the most commonly used resins for biomedical biomaterials so far, although it has inherent bio-inert properties [182]. The main drawbacks of synthetic polymers are poor mechanical properties and high local concentrations of acidic degradation products. Consequently, this can affect cell differentiation on the substrate *in vitro* and trigger an inflammatory response *in vivo* [181]. Both natural and synthetic polymers have relatively poor load-bearing capacity when used alone compared to metallic and ceramic compounds. Incorporating HA into a polymer matrix as a filler has been an approach used to improve both bioactivity and mechanical properties, as discussed in the previous section [142][181].

Recently bio-based polymers have received more attention due to environmental issues [183]. Any polymer derived from living organisms such as plants, trees, and algae is classified as a bio-based polymer. Vegetable oils from both plants (soy, palm, and sunflower oils) and animals (fish oils) have attracted a lot of research interest because of their universal availability, inherent biodegradability, low toxicity, and price [184]. Plant oil-based polymers have also shown excellent cytocompatibility. For example, good cytocompatibility with murine fibroblasts was observed with phosphoester cross-linked vegetable oils and

their metabolites and the materials degraded and was absorbed entirely after 3-month sub-dermal implantation in rats [182].

2.6.2.2.1 Acrylated epoxidized soybean oil

Soybean oil is the most widely available biodegradable and sustainable edible vegetable oil [185]. It is a triglyceride with two dominant fatty acid residues, linoleic acid and oleic acid, and an average number of double bonds per molecule of 4.5 [184][185]. Acrylated epoxidized soybean oil (AESO) is a novel and renewable liquid resin made by the epoxidation of fatty acid double bond followed by epoxy ring acrylation (Figure 2-13) [186]. Additionally, AESO is an excellent option for 3D printing (section 2.7) and photopolymerization to fabricate complex structure for biomedical applications [187]. Multiple studies on AESO-based polymers have shown no cytotoxicity and promising success as biomedical scaffolds [182][185][188]. In [182], Miao *et al.* showed that AESO-based scaffolds were determined biocompatible following observations of high attachment and proliferation of human mesenchymal stem cells (hMSCs). Furthermore, AESO/nHA-based nanocomposite scaffolds with 20 vol% nHA and 2-Hydroxyethyl Acrylate (HEA) or PEGDA fabricated in our lab by Mondal *et al.* showed excellent viability and proliferation of human bone marrow-derived mesenchymal stem cells (BM-MSCs) on all compositions of scaffolds [187].

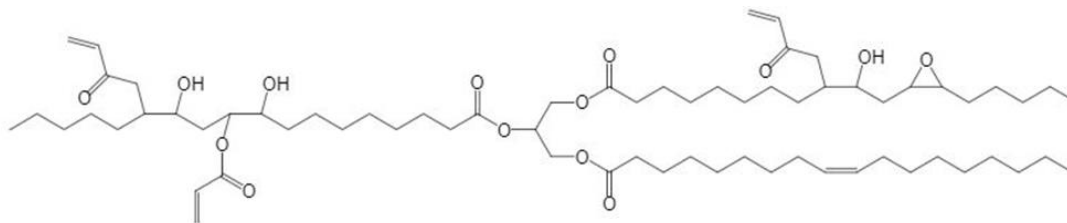


Figure 2-13. The chemical structure of AESO. Reprinted with permission from [186].

2.6.2.2.1.1 Functionalization of AESO

AESO is highly viscous at room temperature and has a low cross-linking capacity due to its aliphatic chains and low degree of unsaturation [189]. The physical properties can be controlled by varying the concentration of polymers, crosslinkers, and degree of crosslinking [190]. So, a reactive diluent (RD), such as a comonomer, is highly desired to help synthesize a low viscosity resin and form a three-

dimensional network with high cross-linking density after the resin is cured. Styrene is often used as an RD that is miscible with AESO and can cross-link efficiently; however, it is carcinogenic. Methyl methacrylate is a monomer that has been used to replace styrene in AESO resins to fabricate new bio-based composites (mAESO) [189]. Furthermore, methacrylated AESO (mAESO) is produced by reacting methacrylate anhydride to create more functional groups (Figure 2-14).

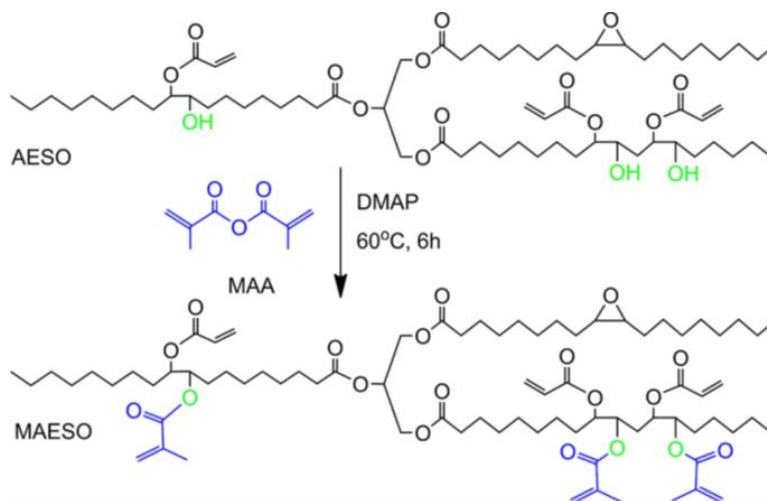


Figure 2-14. Reaction during the modification of AESO to synthesize mAESO. Reprinted with permission from [189].

In general, methacrylation has been reported to have some effects on cell proliferation and differentiation. Sukul *et al.* tested two degrees of methacrylation (69% and 84%) in gelatin methacrylated hydrogel on the growth and differentiation of primary human osteoblasts and observed that cell proliferation was higher on the material with the higher degree of methacrylation [190]. However, while the expression of early osteogenic marker (ALP) was not affected by the degree of methacrylation, the secretion of late osteogenic markers, such as osteoprotegerin, osteopontin, osteocalcin, and angiogenic factors was inversely related to the degree of methacrylation, with higher production observed with a lower degree of methacrylation [190]. Bencherif *et al.* studied the degree of methacrylation on hyaluronic acid hydrogels with a higher degree of methacrylation (60% compared to 32%) were also shown to be more mechanically robust as cross-linking density increased, but different degrees of methacrylation had a minimal effect on mouse muscle fibroblast C2C12 cell lines interactions (morphology, attachment, and proliferation) with the

hydrogels [191]. Overall results around methacrylation suggest that it could potentially have a positive effect on cell-material interactions.

2.7 Overview of 3D-printing

Several fabrication techniques exist to create 3D structures, including electrospinning, fiber bonding, casting, additive manufacturing, melt molding, extrusion, gas foaming, freeze-drying, and phase separation [192][193]. Among these methods, additive manufacturing, also known as 3D printing, has obtained more attention because of its low cost, high resolution, high precision, repeatability, and reproducibility [194][195][196][197]. 3D printing compared to traditional fabrication methods including casting, injection molding, etc., allows for more flexibility and freedom in design and manufacturing of complex, hierarchical, and patient-specific geometries [197].

The nanocomposite ink (AESO/nHA-based) developed by Mondal *et al.*, which will be used in this research study, has been 3D-printed with two additive manufacturing/3d printing techniques Direct Ink Writing (DIW) and masked stereolithography (mSLA) (Figure 2-15) [187][198][199]. The formation of constructs in the extrusion-based 3D printing of biomaterial inks depends on a balance of material viscosity and stabilization upon extrusion [200]. DIW can be used for 3D printing of natural or synthetic polymers containing photo-crosslinkable functional groups at room temperature [182]. This technique uses viscous ink to construct nanocomposite biomaterial grafts with complex structures [201]. In the DIW technique, once the ink is extruded on a build plate, it is solidified by polymerization in layer-by-layer assembly. The combination of DIW and UV irradiated photopolymerization techniques brings the possibility for easy fabrication of bioceramics-based nanocomposites into complex microstructures. It is worth mentioning that no post-fabrication processing is needed for the UV-cured nanocomposites. This helps maintain both ceramic and polymers' physiochemical and biological properties in the composites [187]. In a study by Mondal *et al.*, a 3D-printed AESO/nHA/PEGDA nanocomposites by DIW showed sufficient mechanical properties and cell-material interactions with bone marrow mesenchymal stem cell [187]. While time consuming, DIW is ideal for printing porous 3D scaffolds using AESO/nHA/PEGDA nanocomposite inks

with high HA content [187]. However, due to the rheological properties of the ink, it is challenging to print non-porous and defect-free nanocomposite grafts with complex and precise geometries [198].

Another additive manufacturing process is masked stereolithography (mSLA) which takes a design created in a 3D modeling software to print a 3D structure. mSLA, known as a form of photopolymerization-based stereolithography 3D printing, is a high-resolution light-assisted printing technique in which a light/UV sensitive liquid resin is solidified (cured) layer-by-layer by light/UV exposure. In the mSLA printing method, the machine has a vat that holds the resin and a build plate. The printing process is as follows: first, the build plate is submerged in the resin. Then, the resin surface is exposed to UV light, and polymerization of the liquid photopolymer occurs. The re-submerging of the build plate into the resin is repeated, and the 3D object is created layer by layer (Figure 2-15) [198][202]. In this technique, each layer prints all at once, making it a cost-effective, defect-free, and fast method compared to other techniques such as fused deposition modeling (FDM) or stereolithography (SLA) [203].

The critical matter in mSLA-based 3D printing is that the ink viscosity must be low enough to allow the build platform to move easily through the ink. The viscosity suggested for ceramic-based nanocomposite inks is 5 Pa.s or less [203][204]. The viscosity of AESO at room temperature is 25 Pa.s [205]. Adding PEGDA to AESO/nHA ink helps reduce the ink's total viscosity as it is a very low viscosity (0.025 Pa.s) reactive diluent. PEGDA has two acrylate groups which improve the mechanical properties by increasing the crosslinking density [198], and also improves nanoparticle dispersion [187]. Additionally, PEGDA can be used as a cross-linking agent in AESO/nHA nanocomposites to prepare polymer networks by UV-initiated free-radical polymerization with AESO [199].

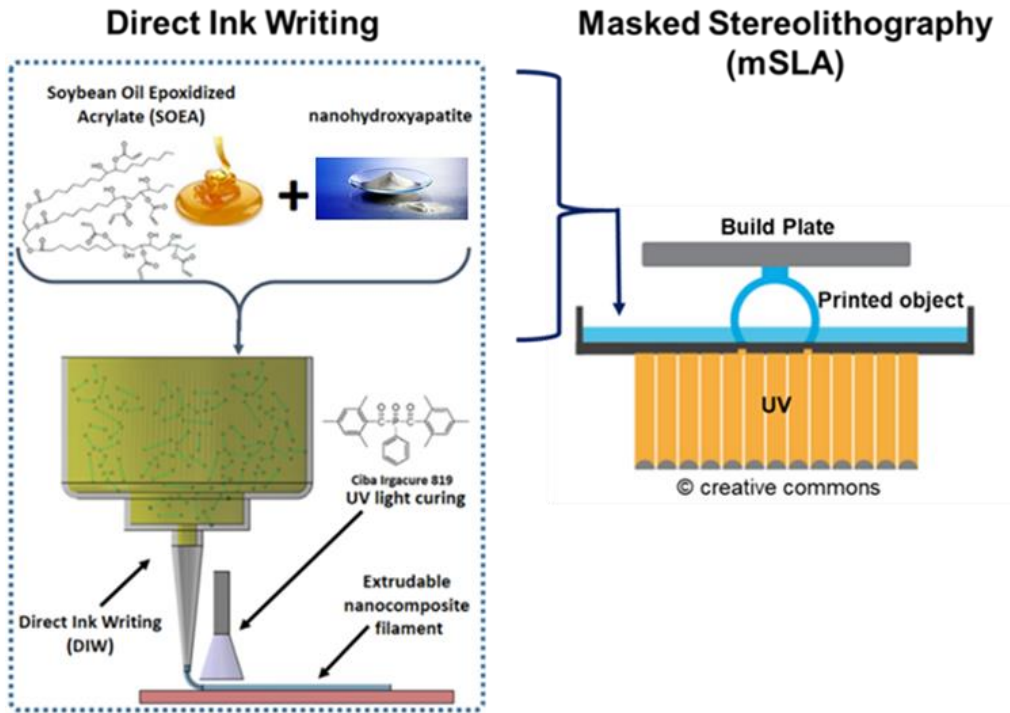


Figure 2-15. 3D printing methods: Direct Ink Writing and Masked Stereolithography. ©Composite Biomaterial Systems Laboratory, University of Waterloo

3 Objectives and Hypotheses

The Waterloo Composite Biomaterial Systems Laboratory, led by Prof. Willett, is developing 3D-printable synthetic biomaterials for the reconstruction of critically sized segmental bone defects. The biomaterial should be mechanically robust, osteoconductive, and support osteoblasts' attachment, proliferation, and differentiation. Moreover, the biomaterial should be remodeled by the normal physiological processes (osteoclast-mediated resorption) rather than degrade by hydrolysis or enzymolysis. The rate of the biomaterial's resorption should be compatible with the rate of new bone formation to maintain the balance between graft resorption and the generation of new bone.

In vitro studies allow for the initial evaluation of novel biomaterials. In this project, experimental protocols were developed and applied to evaluate the *in vitro* response of bone cells - both osteoblasts and osteoclasts - to the novel biomaterials. The composite system tested was the combination of the inorganic phase, calcium-deficient nano-hydroxyapatite nanorods, and an organic phase, acrylated epoxidized soybean oil (AESO) or methacrylated AESO (mAESO) with poly (ethylene glycol) diacrylate (PEGDA). Based on the two preceding chapters, the following objectives and hypotheses were developed for this thesis to contribute to achieving the bigger research program goal of developing competent 3D printable nanocomposite biomaterials for large bone defect reconstruction:

Objective #1: Evaluate *in vitro* osteoblast cells' interactions with the 3D-printed AESO-based nanocomposites.

Hypothesis 1.1: AESO/nHA-based nanocomposites support osteoblast adhesion, proliferation, and activity to the same level as an HA control.

Hypothesis 1.2: A greater volume fraction of nHA in the AESO-based nanocomposites will increase osteoblast adhesion, proliferation, and activity.

Hypothesis 1.3: Methacrylation of AESO (mAESO/nHA-based nanocomposites) will increase osteoblasts adhesion, proliferation, and activity.

Objective #2: Evaluate *in vitro* osteoclast interactions with the 3D-printed AESO/nHA-based nanocomposites

Hypothesis 2.1: AESO/nHA-based nanocomposites support osteoclast adhesion.

Hypothesis 2.2: Methacrylation of AESO will increase osteoclast adhesion.

Hypothesis 2.3: Osteoclasts will create resorption pits on the AESO/nHA-based and mAESO/nHA-based nanocomposites.

4 Materials and Methods

After making nanocomposite inks and discs, *in vitro* cell studies were conducted to evaluate the interaction of osteoblasts and osteoclasts with 3D-printed AESO/nHA-based nanocomposite discs. The first generation of the biomaterial tested was the combination of acrylated epoxidized soybean oil (AESO), nano-hydroxyapatite (nHA), and polyethylene glycol diacrylate (PEGDA, 250 MW). PEGDA was added as a diluent and dispersant, because AESO is too viscous for our printing methods and nHA dispersion is important for cell-material interactions and material strength. Its addition helps to reduce the viscosity, making the ink 3D-printable. In the second generation of the nanocomposite biomaterials, AESO was functionalized with methacrylate groups (mAESO) and AESO was replaced by mAESO in the nanocomposite inks. For the osteoblast study, mouse pre-osteoblast immortalized MC3T3-E1 cells were differentiated to osteoblasts (dMC3T3-OB). Alizarin Red staining assay was used to confirm that cells had differentiated into osteoblasts. To characterize osteoblast-like cells' interactions with biomaterials, cell proliferation (XTT), live/dead, and alkaline phosphatase (ALP) assays were performed on different nanocomposite compositions.

The nanocomposite biomaterial's cell-mediated resorption was assessed using *in vitro* culture of osteoclast cells. Mouse RAW 264.7 macrophages were differentiated to osteoclasts using RANKL and then purified by serum gradient purification (dRAW-OC). To characterize osteoclast-like cells' interaction with biomaterials, nuclei staining with 4',6-diamidino-2-phenylindole (DAPI), phalloidin staining, and detection of tartrate-resistant acid phosphatase (TRAP) were done on nanocomposites. A staining protocol was developed to stain the biomaterial's surface to visualize osteoclast-mediated resorption pits. The effect of methacrylated AESO on osteoclast-like cells' interaction with nanocomposites was studied. HA discs were used as our control biomaterial and a benchmark to compare against our novel nanocomposite biomaterials.

Greater detail of the materials and methods is provided in the next sub-sections.

4.1 Fabrication of 3D-printed nanocomposite discs

4.1.1 3D-printing nanocomposite discs with mSLA printer

The nanocomposite ink was produced, and cylindrical discs were printed in the WCBSL by Dr. Dibakar Mondal (postdoctoral fellow). The nanocomposite inks were a mixture of AESO or mAESO, PEGDA, and nHA. The calcium-deficient nano-hydroxyapatite powder (nHA, rod-shaped, approximately 120 nm long and 30-40 nm diameter) was obtained from MKNano (M K Impex Corp., Mississauga, Canada) and had a calcium-to-phosphorous ratio of 1.52, with a specific gravity of 2.92 and an approximate crystallinity index of 0.52-0.54 [187]. This nHA powder was used as the nanoparticle constituent of the nanocomposite inks. AESO was functionalized with methacrylate groups (mAESO), and the mixture of AESO or mAESO and PEGDA (Sigma Aldrich Co., St. Louis, USA) constituted the biopolymer matrix. Irgacure 819 (Phenylbis (2,4,6-trimethylbenzoyl) phosphine oxide, Sigma Aldrich Co.) was added to the material as a UV photoinitiator. More details on synthesis and chemical modifications can be found in [187][198].

For making the ink with different amount of nano-hydroxyapatite (0, 5, 10, and 30%), the photoinitiator Irgacure 819 was mixed with PEGDA with an ultrasonic homogenizer (Branson Sonifier 450, Emerson Inc., USA) until it dissolved. AESO was added to the mixture of Irgacure and PEGDA and was sonicated for 2 minutes. For the methacrylated nanocomposite inks, methacrylic anhydride (MAA, Sigma Aldrich) was combined with 4- (Dimethyl Amino) pyridine (DMAP) (Alfa Aesar) and added to the AESO, which produced a new biopolymer named mAESO. The same steps were followed for making the inks with mAESO. Once the nanocomposite ink was ready, it was printed as a cylindrical disc (8 mm diameter and 1 mm thickness) using an Anycubic Photon 3D printer with layer-by-layer UV curing (Figure 4-1). After printing discs, a UV post-print curing step was done in a Creative CADworks curing unit (CureZone, Canada). The nanocomposite discs were exposed to lower intensity UV light on each side for 5 minutes and then washed with acetone and 70% ethanol to remove any debris and uncured material on the surface.

Six nanocomposite inks were prepared as shown in (Table 4-1). The ratio of AESO/PEGDA in all compositions was 50/50.

Table 4-1. Compositions of nanocomposite inks

	nHA (vol%)	AESO (S) (vol%)	mAESO (mS) (vol%)	PEGDA (P) (vol%)
SP0	0	50	-	50
SP5	5	47.5	-	47.5
SP10	10	45	-	45
SP30	30	35	-	35
mSP10	10	-	45	45
mSP30	30	-	35	35

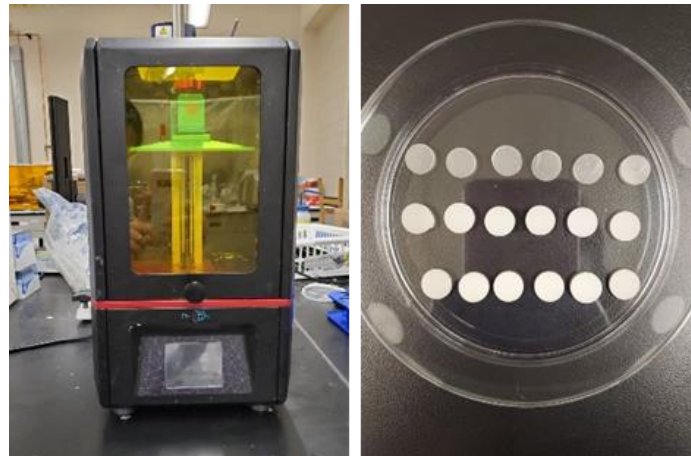


Figure 4-1. (Left) Image of the AnyCubic Photon mSLA 3D-printer and (Right) AESO-based nanocomposite discs printed using the AnyCubic Photon mSLA printer.

4.2 *In vitro* osteoblast study on nanocomposite biomaterials

4.2.1 Osteoblastic differentiation and alizarin red staining

Mouse pre-osteoblast immortalized MC3T3-E1 cells (ATCC, Manassas, Virginia, USA) were differentiated to osteoblasts using an osteogenesis assay kit (MilliporeSigma, Oakville, Ontario, Canada).

The kit contained osteogenesis-inducing biological compounds, including ascorbic acid 2-phosphate, β -glycerophosphate, and melatonin. The MC3T3-E1 cells were cultured in a cell incubator with 5% CO₂ at 37 °C and maintained in growth medium (α -MEM 89%, fetal bovine serum 10%, penicillin/streptomycin 1%) in a flask for 5-6 days, until 80-90% confluency. The cells were detached from the bottom of the flask using TrypLE Express and centrifuged at 300 \times g for 7 minutes to pellet the cells. After resuspending cells and counting cells using a hemocytometer, 1 \times 10⁵ cells per well were seeded in a 24-well plate. Once the cells became confluent, the osteogenesis induction medium#1 was added to each well and changed every 2-3 days to induce osteoblast differentiation. On day 6, the medium was replaced with osteogenesis induction medium#2 and changed every 2-3 days. The amount of each ingredient to make 10 ml of the medium is provided in Table 4-2.

Table 4-2: Ingredients to make 10 ml of osteogenesis induction media

OSTEOGENESIS INDUCTION MEDIUM #1			
Component	Stock Conc.	Amount	Final Conc.
Cell culture medium (e.g., α -MEM containing fetal bovine serum and antibiotics)	100%	9.88 ml	99% (approx.)
Ascorbic Acid 2-Phosphate Solution	0.1 M	20 μ L	0.2 mM
Glycerol 2-Phosphate Solution	1 M	100 μ L	10 mM
OSTEOGENESIS INDUCTION MEDIUM #2			
Cell culture medium (e.g., α -MEM containing fetal bovine serum and antibiotics)	100%	9.87 ml	98% (approx.)
Ascorbic Acid 2-Phosphate Solution	0.1 M	20 μ L	0.2 mM
Glycerol 2-Phosphate Solution	1 M	100 μ L	10 mM
Melatonin Solution	50 μ M	10 μ L	50 nM

Qualitative analysis using Alizarin Red was performed to confirm differentiation through the presence of calcium in the matrix deposited by osteoblasts. After 14 and 21 differentiation days, the cells were fixed and stained with Alizarin Red stain solution (EMD Millipore Corp., USA). Briefly, cells were washed with PBS and fixed with 10% formaldehyde for 15 minutes at room temperature (RT). Then, the cells were rinsed with distilled water three times, and 1 ml of Alizarin Red solution was added to each well. After 20 minutes, the excess dye was washed four times with deionized water. Visual inspection by microscope was then performed. Differentiated cells stain bright red once exposed to the Alizarin Red

solution, an indication of mineral deposition and thus confirming the osteoblast phenotype of dMC3T3 E1 cells after 21 days of differentiation (Figure 4-2).

The differentiated cells formed a layer at the bottom of each well after 21 days. These were collected and put in a flask (T75) in a growth medium to allow differentiated cells to migrate out of the layers and spread out. After two weeks of culture in osteogenesis medium #1, the cells were detached with TrypLE Express, and aliquots of differentiated MC3T3-E1 cells (dMC3T3-OB) were frozen in a liquid nitrogen tank for future experiments.

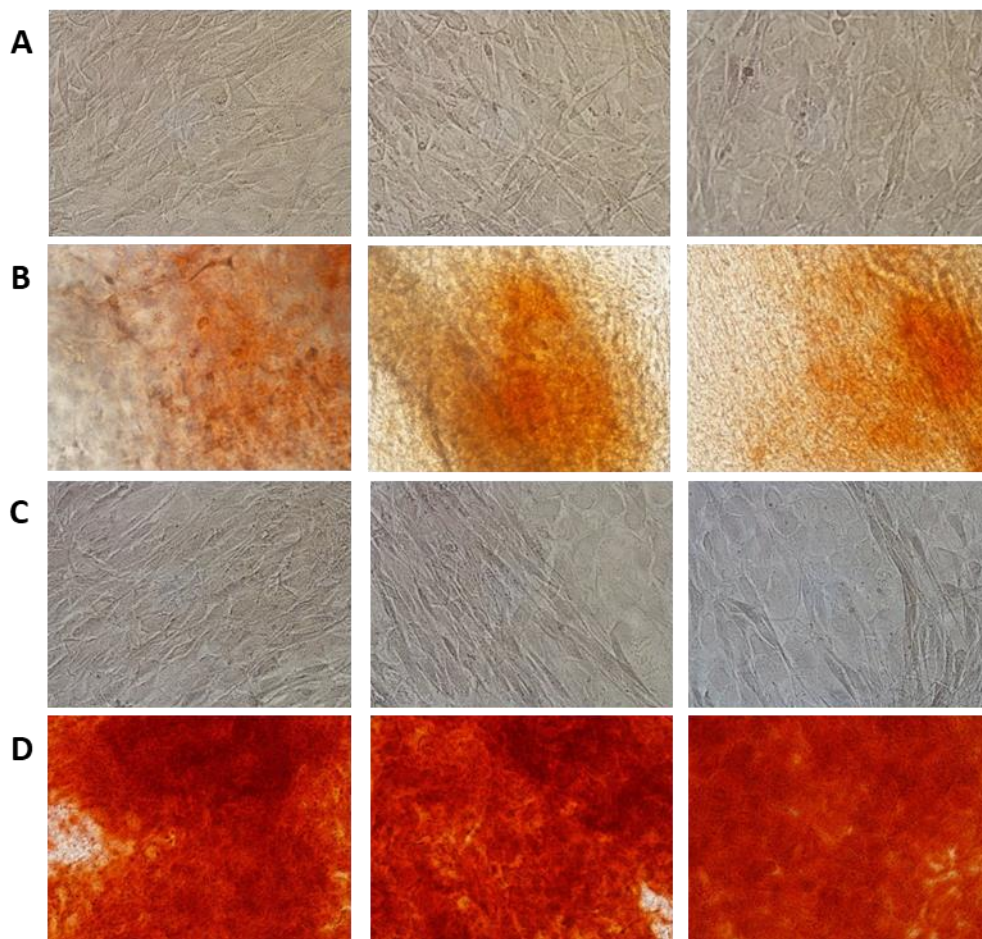


Figure 4-2. MC3T3-E1 after 14 (A, B) and 21 (C, D) days of osteogenic differentiation. Cells differentiated to a mature osteoblastic lineage as indicated by the Alizarin Red staining (B, D). Alizarin Red staining is not observed in undifferentiated MC3T3-E1 cells (A, C).

4.2.2 Culturing dMC3T3-OB cells on nanocomposite discs¹

A pilot study was performed for three different composition of nanocomposites printed by Direct Ink Writing (DIW) and allowed to develop the protocol for the osteoblast study (see Appendix 1 for more details). dMC3T3-OB cells were cultured in a growth medium composed of Minimum Essential Medium alpha (α -MEM) (Life Technologies, Burlington, Ontario, Canada) supplemented with 10% fetal bovine serum (FBS), 1% penicillin/streptomycin (P/S), 0.2 mM ascorbic acid-2-phosphate and 10 mM β -glycerophosphate. Cells from passages 2 to 6 were used for the experiments. In [206], Wang *et al.* claimed that non-mineralizing colonies formed when cells were repeatedly passaged. Therefore, passaging dMC3T3-OB cells too many times was avoided, and cells were used until passage 6, based on the literature [207].

To prepare for cell culture, the 3D printed discs were washed with 70% ethanol for 5 minutes and rinsed twice in sterile phosphate-buffered saline (PBS, 5 minutes each wash). Subsequently, discs were sterilized under UV light in a bio-safety cabinet for 20 min. Discs were then incubated in Minimum Essential Medium Alpha medium (α -MEM) containing 50% fetal bovine serum (FBS) and 1% penicillin-streptomycin (P/S) at 37 °C, 5% CO₂ overnight to improve cell adhesion due to protein adsorption. Commercially-available, sterile hydroxyapatite (HA) discs (8 mm in diameter and 2 mm in thickness, 3D Biotek, USA) were used as controls; they were treated the same way as nanocomposite discs except for the washing with ethanol and PBS.

After sterilizing and treating the samples, discs were placed in silicone rings (Dow Corning Silastic, HelixMark, USA, inner diameter 7.94 mm, outer diameter 12.7 mm) to keep cells on the discs during seeding and incubation times (Figure 4-3) and then this construct was added to a well of a 24-well plate. dMC3T3-OB cells were seeded at a density of 10,000 cells per disc (20,000 cells/cm²). Samples were incubated for 2 hours to allow cell attachment, and 0.25 ml of growth medium (α -MEM supplemented with

¹ This section has been published in "mSLA-based 3D Printing of Acrylated Epoxidized Soybean Oil-Nano-Hydroxyapatite Composites for Bone Repair." *Materials Science and Engineering: C (2021): 112456*, a paper in which I contributed to as a co-author (I performed and analysed all cell experiments) with D. Mondal, C. J. Huxman, S. Tanter, D. Sun, M. Gorbet, T. L. Willett.

10% FBS, 1% P/S, 0.1 mM ascorbic acid-2-phosphate, and 10 mM β -glycerophosphate) was then added. Samples were cultured for 1, 3, and 7 days and the growth medium was changed every day.

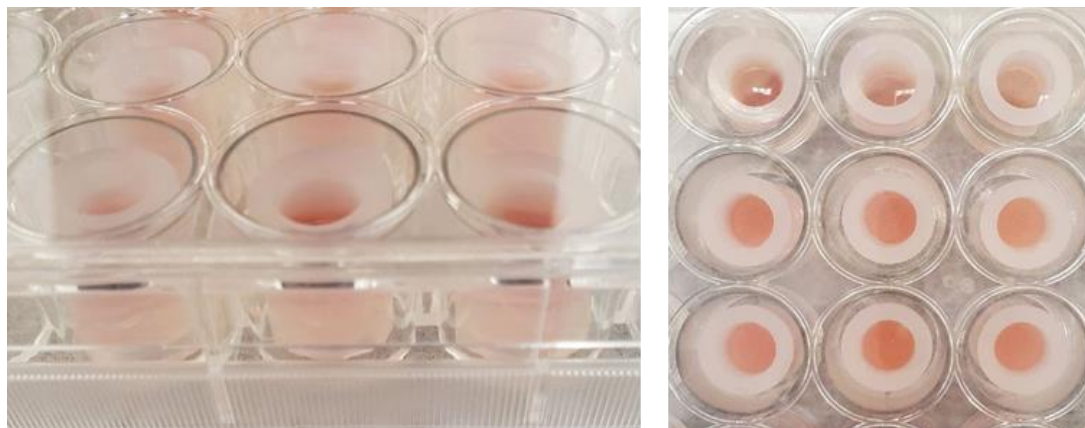


Figure 4-3: Discs in silicone tubes to keep cell suspension on the surface

4.2.3 Evaluation of dMC3T3-OB cells interaction with nanocomposite discs²

Various assays were performed to characterize the interactions of dMC3T3-OB with the 3D-printed nanocomposite discs. XTT and live/dead assays were performed on each sample to measure cell proliferation and viability at each time point. Cell proliferation after 1-, 3- and 7-days of culture was characterized using XTT (sodium 3'-[1-(phenylaminocarbonyl)-3,4-tetrazolium]-bis (4-methoxy6-nitro) benzene sulfonic acid hydrate; TACS XTT cell proliferation kit, R&D Systems, Minneapolis, USA). In the XTT assay, a yellow tetrazolium salt is cleaved by mitochondrial enzymes in metabolically active cells to a soluble orange formazan dye that is measured by absorbance at 490 nm in a microplate reader [208]. XTT working solution (XTT reagent and XTT activator dissolved in DMEM without phenol red) was added within the confines of each silicone ring construct, and the samples were incubated for 2.5 h at 37 °C. The supernatant was then transferred to a 96-well plate, and absorbance was measured at 490 nm with a reference wavelength of 630 nm on a SpectraMax Plus 384 Microplate Reader. Results were expressed as corrected absorbance values (*i.e.* working solution absorbance was subtracted from the sample absorbance).

² The first and second paragraph of this section have been published in "mSLA-based 3D Printing of Acrylated Epoxidized Soybean Oil-Nano-Hydroxyapatite Composites for Bone Repair." *Materials Science and Engineering: C (2021): 112456*, a paper in which I contributed to as a co-author (I performed and analysed all cell experiments) with D. Mondal, C. J. Huxman, S. Tanter, D. Sun, M. Gorbet, T. L. Willett.

Following the XTT assay, live/dead staining (Life Technologies Inc., CA) was performed. Live/dead staining is a two-color fluorescence cell viability assay that measures intracellular esterase activity and plasma membrane integrity of cells using calcein-AM and ethidium homodimer (EthD-1), respectively. The discs were incubated with a growth medium containing 4 μM EthD-1 (stains dead cells red) and 2 μM Calcein AM (stains live cells green) for 30 minutes at 37 $^{\circ}\text{C}$, directly followed by imaging with a Nikon Eclipse TS100 fluorescence microscope (Tokyo, Japan, Figure 4-4).



Figure 4-4: Nikon Eclipse TS100

As alkaline phosphatase (ALP) is a hallmark of osteoblast functionality, an ALP assay was performed to detect ALP production in dMC3T3-OB using the SensoLyte NPP Alkaline Phosphatase Assay Kit (AnaSpec, USA). In this assay, *p*NPP turns yellow when dephosphorylated and can be detected at an absorbance of 405 nm. At each time point, medium was aspirated, collagenase/trypsin solution (1ml for experiments 1-2, and 0.5 ml for experiments 3-4) was added to each well and incubated for 30 min at 37 $^{\circ}\text{C}$, followed by shaking the plate gently to remove the cells from the discs. Each cell suspension was transferred into a 2 ml Eppendorf tube and stored at -80 $^{\circ}\text{C}$. After collecting all time points, cell lysis was done using a freeze-thaw method, alternating three cycles of freezing at -80 $^{\circ}\text{C}$ (1 hr each) and thawing 37 $^{\circ}\text{C}$ 40 min). After centrifuging the suspension for 15 min at 10,000 rpm, a 50 μL aliquot of each supernatant was added to a well of 96-well plate. Then, 50 μL of *p*NPP substrate solution was added to each well, and the reagents were mixed gently by shaking the plate by hand for 30 sec. The absorbance was measured at 405 nm after incubating samples for 1 hr, 2 hr, 3 hr, 4 hr, 5 hr at RT. Then, the samples were placed in the

fridge and the absorbance was measured after 24hr. The data from 24hr was selected to report the ALP results; the low ALP concentrations in our samples required a longer incubation time with the chromogenic substrate to allow for better color development while still fitting the standard curve.

The flowchart (Figure 4-5) summarizes the steps and assays for characterizing the interactions of osteoblast-like cells with the 3D-printed nanocomposites.

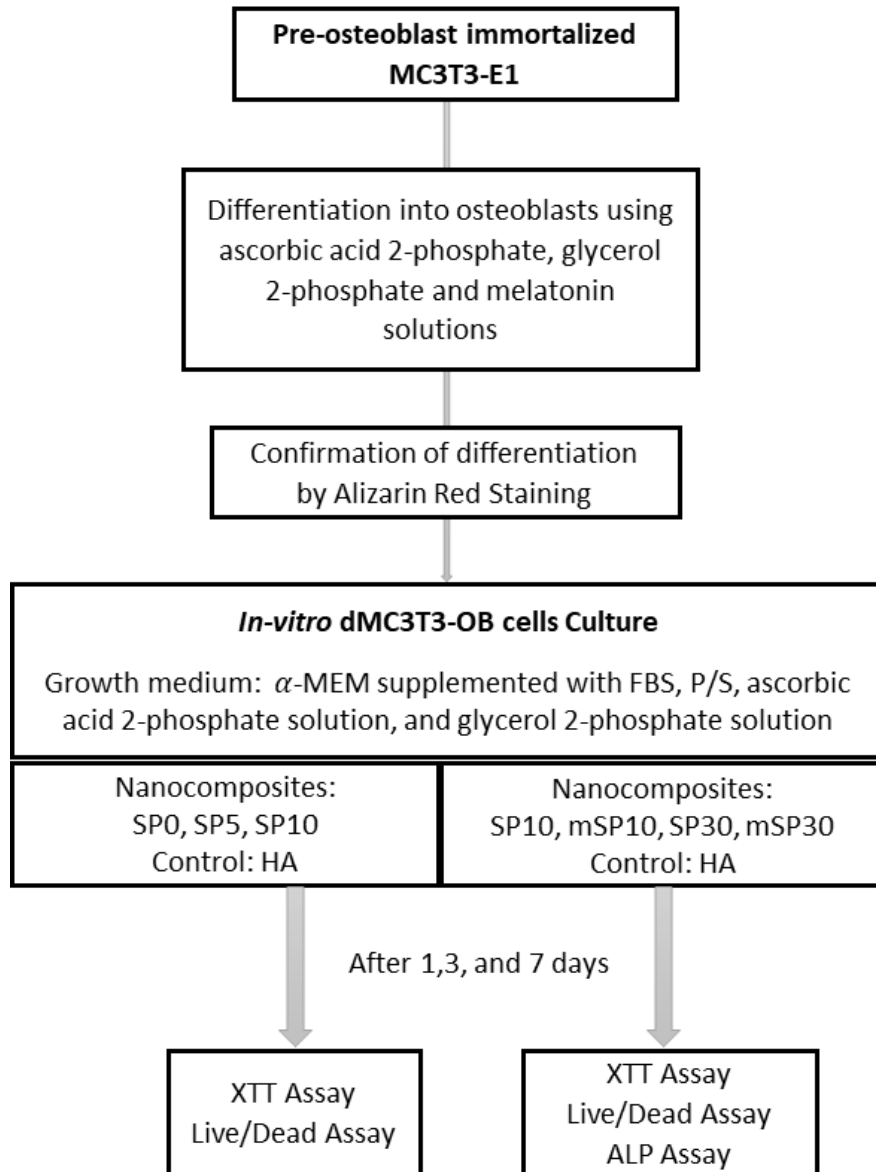


Figure 4-5. In vitro methodology to assess OB-like cells interactions with nanocomposites

4.3 *In-vitro* osteoclast study on nanocomposite biomaterials

4.3.1 Differentiation of RAW264.7 cells to osteoclasts and serum gradient purification

RAW264.7 murine macrophages (ATCC, Manassas, Virginia, USA) were differentiated to osteoclasts using RANKL (R&D Systems, Minneapolis, Minnesota, United States). RAW264.7 macrophages were cultured in a cell incubator with 5% CO₂ at 37°C and maintained in a growth medium Dulbecco's Modified Eagle Medium (DMEM) supplemented with 10% FBS and 1% P/S in a flask for 4-5 days until 80-90% confluency. The cells were detached from the bottom of the flask using TrypLE Express (10 min incubation), 10 ml DMEM was added and centrifuged at 100×g for 5 minutes to pellet the cells. After counting, RAW264.7 cells were seeded at a density of 1.5×10⁵ cells/cm² in a T25 flask and allowed to adhere for 4 hours, and culture media was then supplemented with 30 ng/ml RANKL. The differentiation medium with fresh RANKL was replaced on day 2 and day 3.

On day 4, serum gradient was used to purify the differentiated multinuclear RAW264.7 as per [80]. Differentiated RAW 264.7 cells were detached using 3 ml TrypLE Express (10 min incubation) and resuspended in 15 ml of Moscona's high carbonate (MHB) solution. The MHB solution consisted of 137 mM NaCl, 2.7 mM KCl, 0.4 mM NaH₂PO₄, 12 mM NaHCO₃, and 11 mM dextrose in water and had a pH of 7.2. A serum gradient was prepared by placing a layer of 15 ml 70% FBS solution in MHB at the bottom of a 50-ml conical tube. A layer of 15 ml 40% FBS solution was slowly added as a second layer. Then, 15 ml of cell suspension was added on top without disturbing the layers (Figure 4-6). The tube was capped and held undisturbed at RT for 30 min to allow cells to separate based on their density. Three layers were collected separately; top 17-ml layer, middle 16-ml layer, and bottom 12-ml layer. In the preliminary study, all three separate layers were collected and centrifuged at 500×g for 5 min, resuspended in culture medium, and seeded on a tissue culture plate at a density of 5000 cells/cm² overnight to identify cell population in each layer by performing TRAP staining.

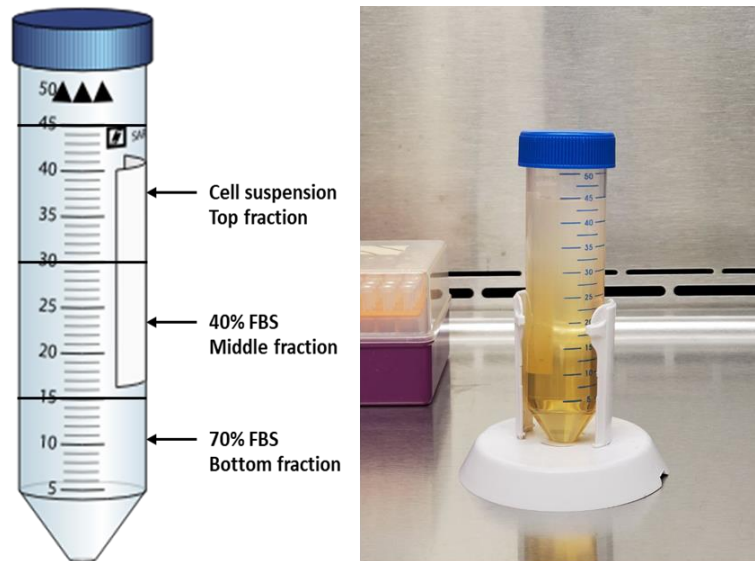


Figure 4-6. Serum gradient purification of differentiated RAW 264.7 cells in a 50 ml tube.

4.3.1.1 TRAP staining of purified cells

The cultured cells were stained for tartrate-resistant acid phosphatase (TRAP) to confirm the presence of differentiated osteoclasts using the Acid Phosphatase Leukocyte (TRAP) kit (Sigma Aldrich Co., St. Louis, USA). A TRAP staining solution containing 0.125 mg/ml Naphthol AS-BI Phosphate, 0.1M acetate buffer; 6.7 mM L(+)-tartrate, 1 mM sodium nitrite, and 0.07 mg/ml diazotized Fast Garnet GBC Solution was prepared. After fixing cells in 4% formaldehyde, the medium was aspirated, and 1 ml of staining solution was added to each well. After staining at 37°C for 1 h, cells were counterstained 2 minutes in hematoxylin solution at room temperature. Then, each well was rinsed three times with deionized water and allowed to air dry before imaging.

Although all layers contained RAW264.7 cells staining TRAP-positive, not all of these cells fused into multinuclear cells. After serum gradient purification, the top fraction of the serum gradient comprised mostly of mononuclear cells (Figure 4-7-A). A mix of mononuclear and multinuclear cells were observed in the middle fraction (Figure 4-7-B). In the bottom fraction, more multinuclear cells with a very small portion of mononuclear cells were seen (Figure 4-7-C-H). TRAP staining and multinuclearity of cells indicated that cells differentiated into multinuclear osteoclasts. Based on these results, only the bottom layer (dRAW-OC cells) was collected to perform osteoclast experiments with the nanocomposites.

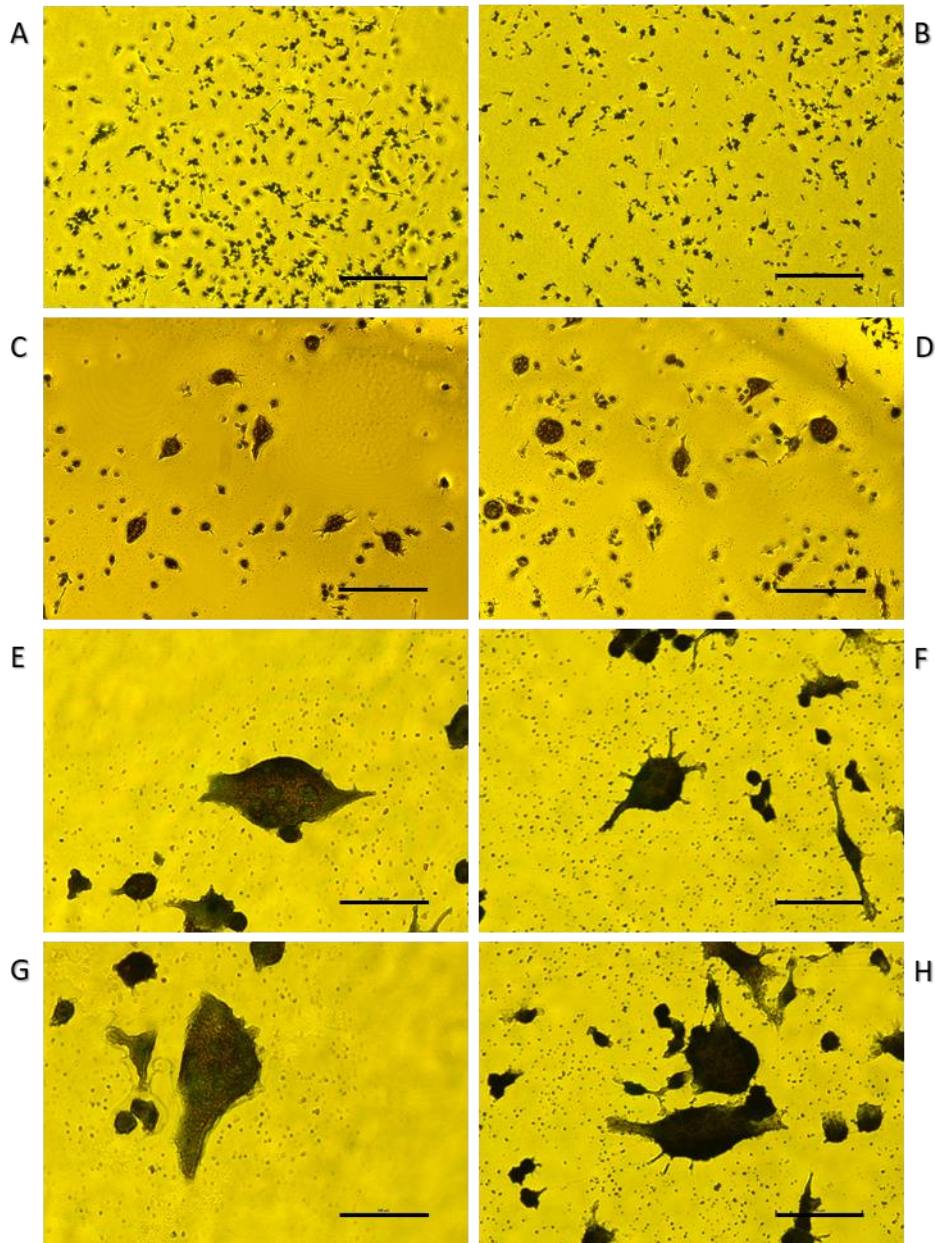


Figure 4-7. Isolated TRAP-positive dRAW264.7 osteoclasts by serum gradient. Nuclei stained with hematoxylin solution. After separation by serum gradient, (A) the top fraction contained mostly mononuclear cells. (B) The middle fraction of the gradient contained a mix of mononuclear and multinuclear cells. (C-H) The majority of cells in the bottom fraction were multinuclear cells. (A D:10X, scale bar: 200 μ m), (E-H:40X, scale bar: 50 μ m).

4.3.2 Culturing dRAW-OC cells on SP30 and mSP30 nanocomposite discs

After sterilizing the 3D nanocomposite discs, in the same manner as described in section 4.2.2, discs were incubated in DMEM containing 50% FBS and 1% P/S at 37°C, 5% CO₂ overnight. Sterile HA

discs were used as controls. After sterilizing and treating the samples, discs were placed in silicone rings and then added to a well of 24-well plate. For each experiment, RAW264.7 cells were differentiated in a flask and then isolated by serum gradient the day of the experiment. dRAW-OC cells were seeded at a density of 3,000 cells per disc (6,000 cells/cm²). Cells were allowed to adhere on the samples for 2 hours in the incubator, and then 0.5 mL of growth medium (DMEM supplemented with 10% FBS, 1% P/S, and 30 ng/ml RANKL) was added. Samples were cultured for 7 days, and the growth medium was changed every other day.

4.3.3 Evaluation of dRAW-OC cells interaction with SP30 and mSP30 nanocomposite discs

Different assays were performed to characterize the interactions of dRAW-OC cells with SP30, mSP30, and HA discs. TRAP, F-actin and nuclei staining, and a resorption pit assay were performed to characterize multinucleated osteoclasts and their activity on the surface. Different discs were used for each assay.

4.3.3.1 TRAP Staining

The TRAP staining kit (Cosmo Bio USA, Inc.) was used to stain tartrate-resistant acid phosphatase in osteoclasts. Based on the kit protocol, on day 7, the culture medium was aspirated, and cells were washed with PBS. Then, 4% formaldehyde was added to each well to fix cells at room temperature for 20 minutes. After fixation, cells were washed with deionized water three times. One vial of Chromogenic Substrate from the kit was dissolved with 5 ml of Tartrate-containing Buffer, and 500 μ l was added to each disc. After a 20-minute incubation at 37°C, the discs were washed with deionized water to stop the reaction. Visual inspection by microscope was then performed. Figure 4-8 shows TRAP-positive dRAW264.7-OC-OC cells from the bottom fraction of serum gradient purification.

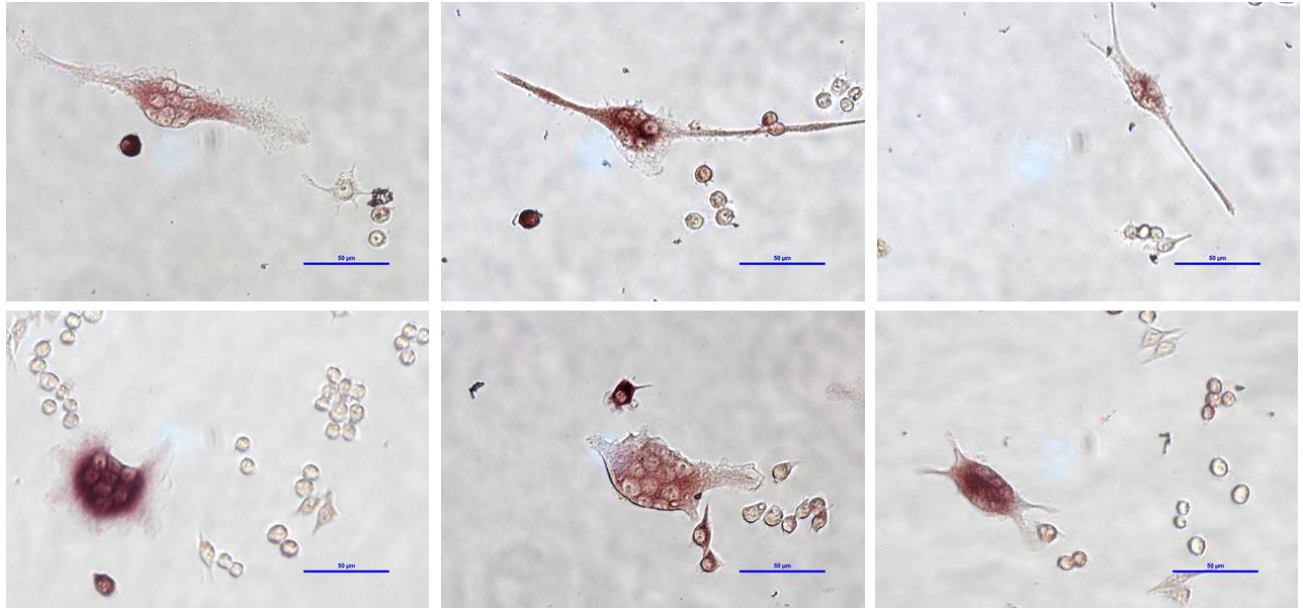


Figure 4-8. TRAP-positive dRAW264.7 osteoclasts from the bottom fraction of the serum gradient purification. Staining was performed with Cosmo Bio kit (scale bar: 50 μ m).

4.3.3.2 F-Actin and Nuclei Staining

Phalloidin is a high-affinity filamentous actin (F-actin) probe that can be coupled to the green-fluorescent Alexa Fluor 488 dye. Alexa 488 phalloidin (Invitrogen, Massachusetts, United States) was used to detect actin rings to indicate sealing zones formed by dRAW-OC on the discs' surface. 4',6-diamidino-2-phenylindole (DAPI) (Dojindo Molecular Technologies, Inc., Rockville, United States) is a fluorescent stain that labels DNA and stains both live cells and fixed/dead cells (DAPI can pass through an intact cell membrane) and was used as a nuclear stain.

On day 7, for F-actin and nuclei staining, cells were rinsed with 37°C PBS and then fixed with 4% formaldehyde for 20 minutes at RT. After washing three times with PBS (5 minutes each time), cells were permeabilized with 0.1% Triton X-100 (Thermo Fisher Scientific, Massachusetts, United States) in PBS for 10 minutes. Cells were washed three times with PBS (5 minutes each time), and a solution of 1.5% Bovine Serum Albumin (BSA, Sigma Aldrich Co.) in PBS was added to each well and incubated for an hour at RT to prevent nonspecific binding. For staining, 5 μ l of dissolved stock solution of Phalloidin stain in 200 μ l of PBS was added to each well and the plate was incubated for 30 min in the dark (covering the plate with aluminum foil) at RT. Then, the nuclei of cells were stained with DAPI at a 1:1000 dilution in

PBS for 2 min at RT. As a final step, cells were washed twice with PBS, and the stained nuclei and F-actin were visualized by fluorescence microscopy (Nikon Eclipse TS100).

The osteoclast number (more than three nuclei), F-actin size ring (diameter), and number of nuclei per osteoclast were quantified using NIS-Elements Software. The nuclei number of each osteoclast was counted for three discs. Size of actin ring, number of osteoclasts per square centimeter, number of nuclei per osteoclast were averaged for each nanocomposite and control. Up to 100 osteoclasts were characterized on each specimen [209].

4.3.3.3 Resorption pit assay

Calcein is a calcium-binding fluorescent molecule that was proposed to detect calcium hydroxyapatite 15 years ago [210]. From calcein powder (C0875, Sigma-Aldrich), a 10 mM calcein solution was prepared in 0.1 M of NaOH. A 1 mM working solution was prepared in deionized water and sterile filtered using a 0.2 μm pore filter. On day 7, cells were removed from the nanocomposite discs by incubating in TrypLE Express for 20 min at 37°C and then putting on a shaker for 10 minutes with a speed of 250 rpm. The discs were rinsed with deionized water and then calcein solution was added directly to the discs for 5 hr at RT. Before imaging, each disc was washed with deionized water 3 times, and then the stained surface was imaged with a Nikon Eclipse TS100 fluorescence microscope.

4.3.3.4 Confocal laser microscopy and analysis

Images of stained surfaces were collected using a confocal laser scanning microscope (Leica TCS SP5 system, Germany in Molecular and Cellular Imaging Facility, University of Guelph) with an upright Leica DM 6000B microscope using LAS AF software. To identify pits, an oil 20 \times lens was employed. Samples were exposed to 458 nm laser light, and the reflected signal was collected in one detector. Z-stacks were collected at 20 \times and a step size of 3 μm . Volume viewing was performed using Nikon Imaging Software NIS-Elements AR (Nikon Canada, Mississauga, ON, Canada).

The flowchart (Figure 4-9) summarizes the steps and assays for characterizing the interactions of the osteoclast-like cell with the 3D-printed nanocomposites.

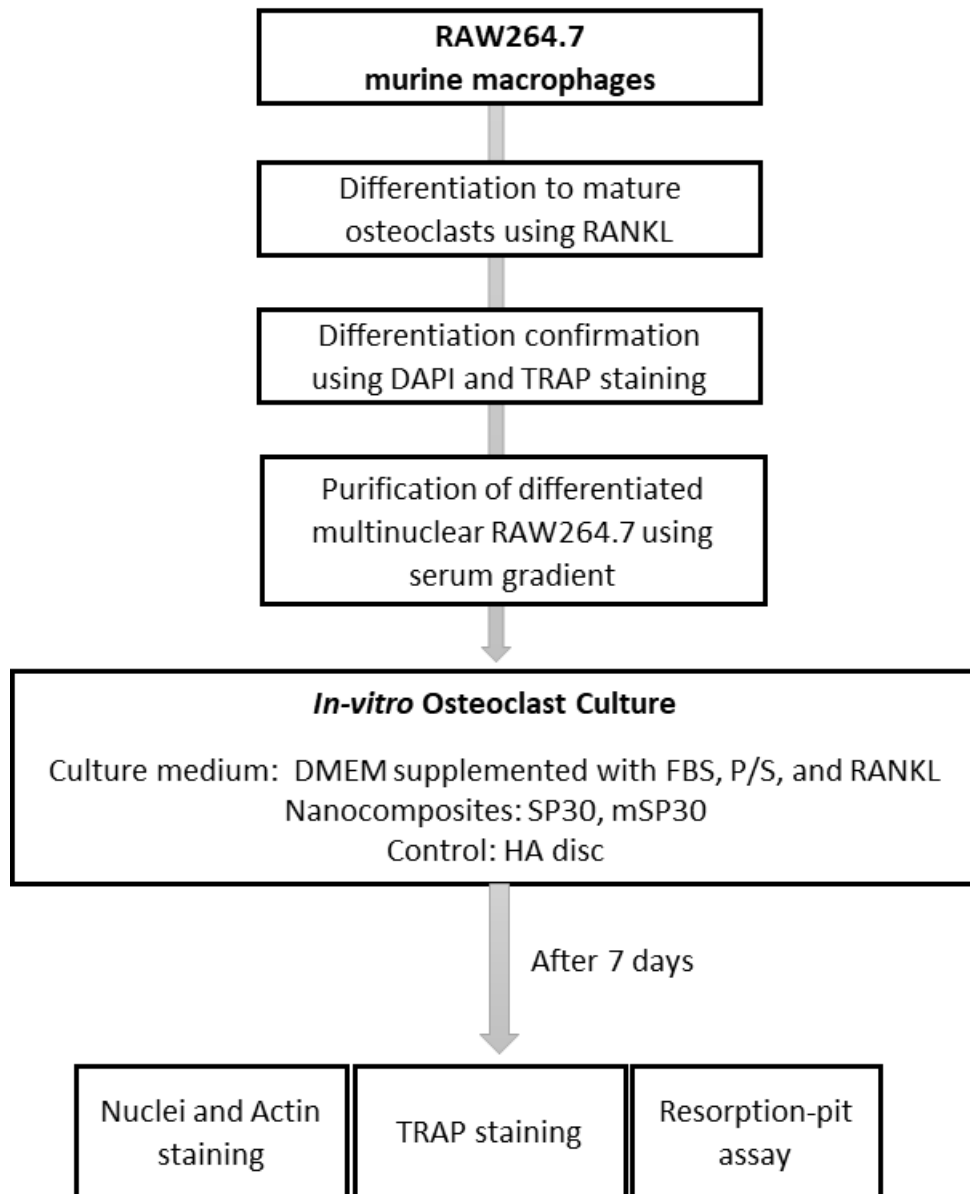


Figure 4-9. *In vitro* methodology to assess OC-like cells interactions with nanocomposites

4.4 Statistical Analysis

Data are presented as mean \pm standard deviation (SD). All data were analyzed using SigmaStat (Version 4.0, Systat Software Inc., CA, USA). Means were compared using one-way or two-way analysis of variance (ANOVA) followed by post hoc Tukey's multiple comparison test. Differences between means were considered statistically significant at $p < 0.05$.

5 Evaluation of dMC3T3-OB cells responses to the 3D-printed nanocomposite discs: results and discussion

Two studies were performed to evaluate dMC3T3-OB cell interactions with nanocomposites 3D-printed using masked-stereolithography (mSLA). The first study focussed on SP0, SP5, and SP10 nanocomposite discs to assess the effect of hydroxyapatite and AESO amount on cell viability and proliferation. In the second study, dMC3T3-OB cells were cultured on SP10, SP30, mSP10, and mSP30 discs to investigate the effect of hydroxyapatite amount and methacrylation of AESO on viability, proliferation, and ALP activity of cells.

5.1 dMC3T3-OB cells proliferation and viability on SP0, SP5, and SP10 nanocomposite discs³

Cell proliferation and viability on the three nanocomposites were assessed after 1, 3, and 7 days of culture. As shown in Figure 5-1, differentiated MC3T3-E1 osteoblasts showed excellent viability on SP0, SP5, and SP10 surfaces at all time points. A few dead cells were observed using live/dead staining. Cells seeded on SP5 and SP10 demonstrated excellent morphology at day 1. While a higher cell density could be observed on SP0 compared to SP5, SP10, and HA discs after day 1, a significant increase in proliferation ($p < 0.05$) was only observed on SP5, SP10, and HA discs at day 3 and day 7 (Figure 5-2).

³ This section has been published in "mSLA-based 3D Printing of Acrylated Epoxidized Soybean Oil-Nano-Hydroxyapatite Composites for Bone Repair." *Materials Science and Engineering: C* (2021): 112456, a paper in which I contributed to as a co-author (I performed and analysed all cell experiments) with D. Mondal, C. J. Huxman, S. Tanter, D. Sun, M. Gorbet, and T. L. Willett.

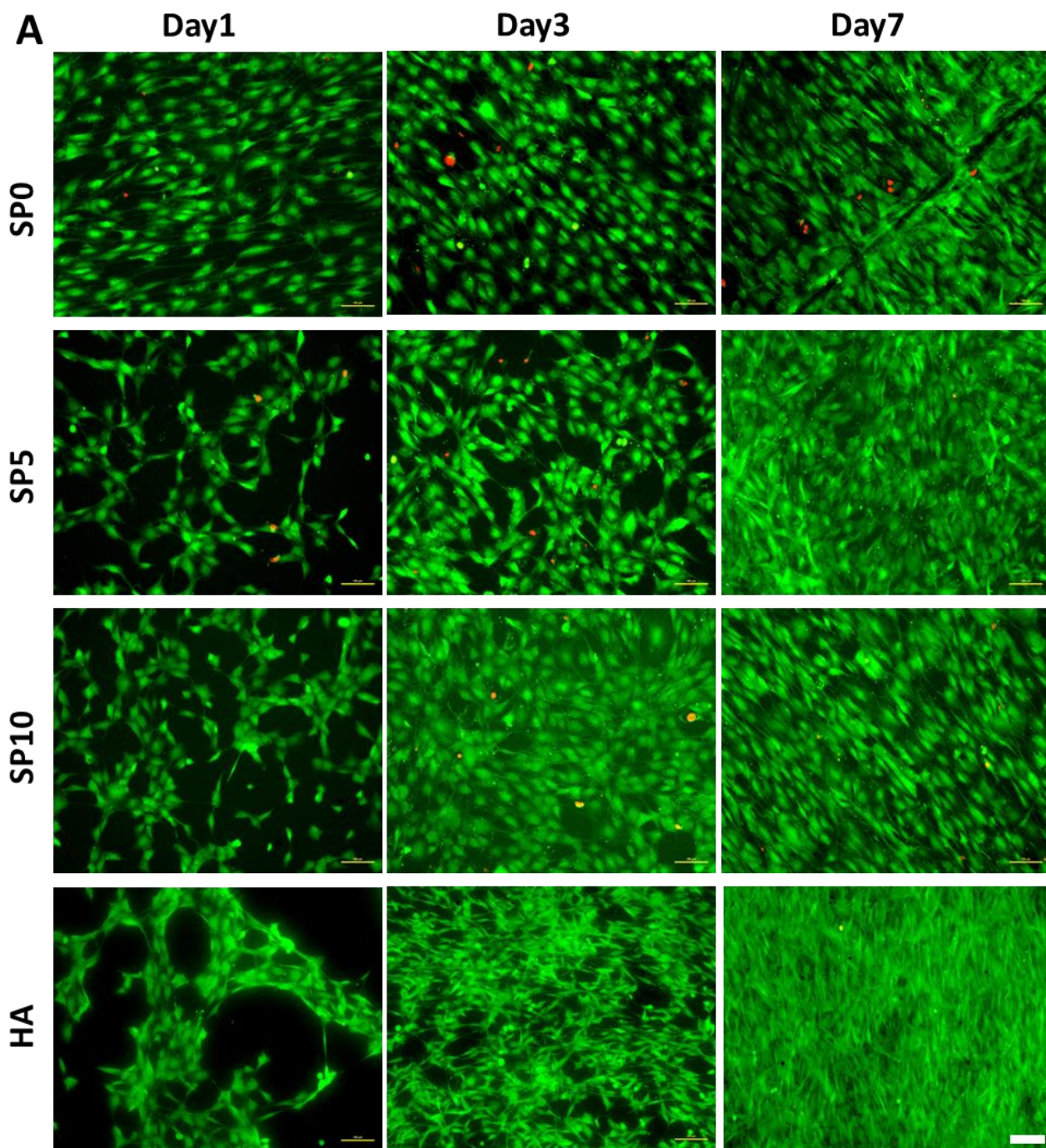


Figure 5-1: Differentiated MC3T3-E1 osteoblast cell viability and adhesion on 3D printed nanocomposite discs. Representative images of live/dead staining of cells on SP0 (0% nHA), SP5 (5% nHA), SP10 (10% nHA), and HA (control) discs at day 1, 3, and 7 days after seeding. Calcein AM stains live cells green, and EthD-1 stains dead cells red. Scale bar represents 100 μm [198].

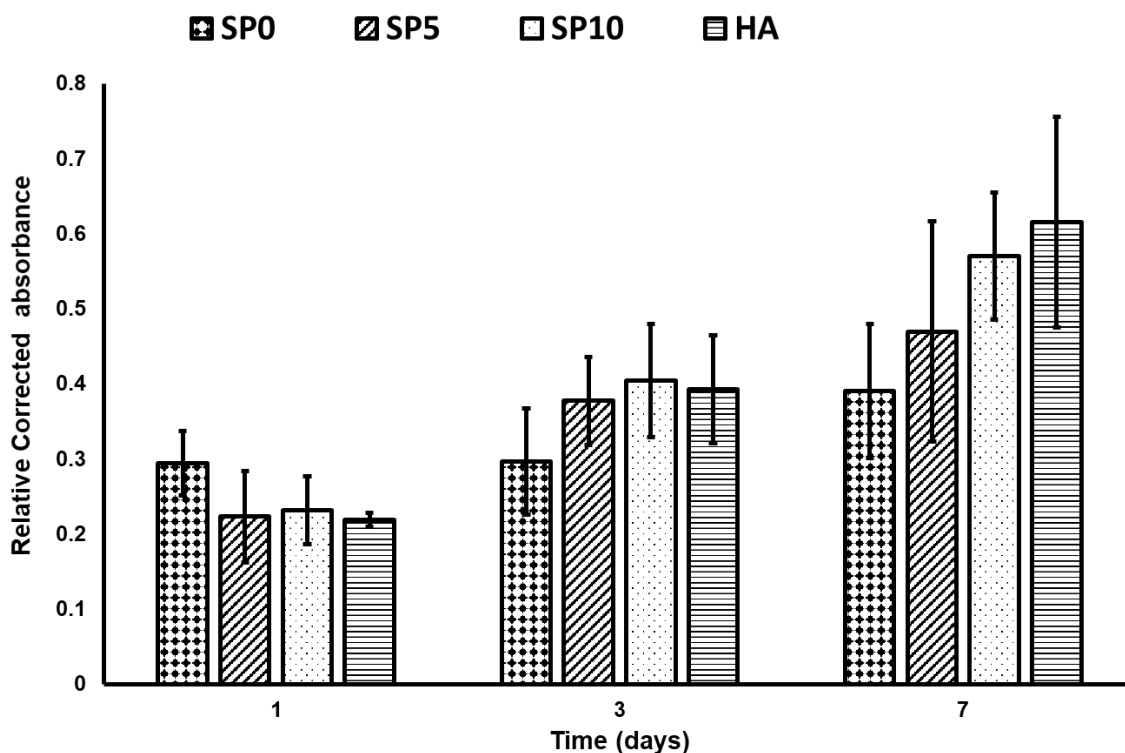


Figure 5-2. Differentiated MC3T3-E1 osteoblast cell proliferation on 3D printed nanocomposite discs; SP0 (0% nHA), SP5 (5% nHA), SP10 (10% nHA) and HA (control). Proliferation of dMC3T3-OB cells as measured using the XTT assay. Data are means \pm SD ($n = 7$ for nanocomposite discs and $n = 4$ for HA discs, from 3 experiments, *** statistically significant $p \leq 0.001$) [198].

5.2 dMC3T3-OB cells proliferation, viability, and ALP activity on SP10, mSP10, SP30, and mSP30 nanocomposite discs

dMC3T3-OB cells were seeded on the surfaces of non-porous nanocomposites discs and cell viability, proliferation, and ALP activity on the four nanocomposite types were assessed after 1, 3, and 7 days. Live-dead staining showed high cell viability on all nanocomposite discs, with most cells alive (Figure 5-3). Cells on SP10, mSP10, SP30, and mSP30 showed excellent morphology at day 1. A high cell density was observed on all nanocomposites and HA discs after day 1, 3, and 7. On day 1, HA showed less proliferation compared to SP10, mSP10, SP30, and mSP30, and it was significantly different from mSP30 ($p < 0.05$). There was a significant increase in proliferation ($p < 0.05$) observed on SP10, mSP10, SP30, mSP30, and HA discs at day 3 and day 7 compared to day 1 (Figure 5-4). On day 3, mSP30 showed the highest proliferation compared to all other groups ($p < 0.01$). On day 7, mSP30 and HA were significantly

different from SP10, mSP10, and SP30 ($p < 0.05$); and there was no statistically detectable difference between mSP30 and HA.

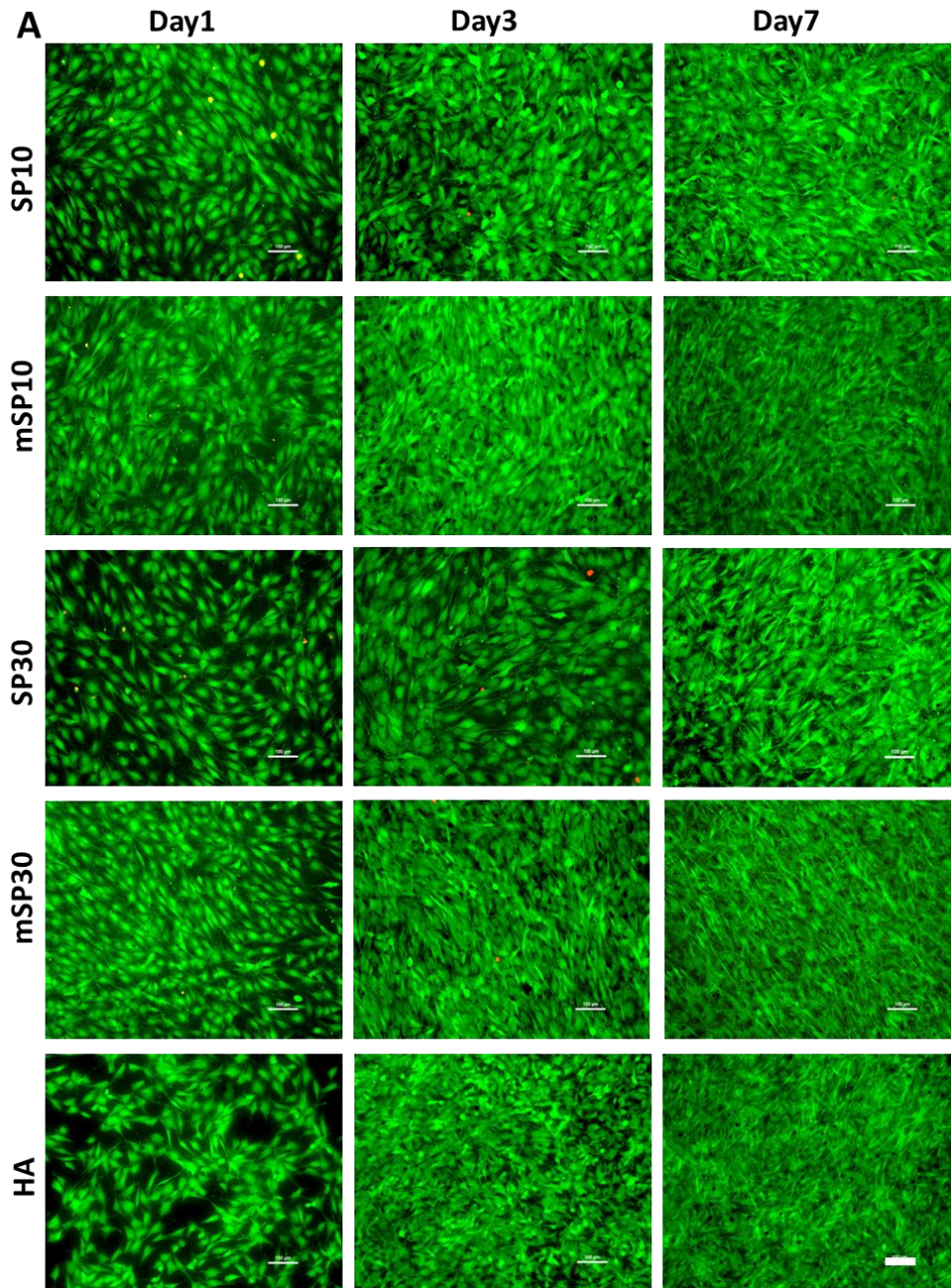


Figure 5-3. Differentiated MC3T3-E1 osteoblast cell viability and adhesion on 3D printed nanocomposite discs. Representative images of live/dead staining of cells on SP10 (10% nHA), mSP10 (methacrylated AESO and 10% nHA), SP30 (30% nHA), mSP30 (methacrylated AESO and 30% nHA) and HA (control) discs at day 1, 3, and 7 days after seeding. Calcein AM stains live cells green, and EthD-1 stains dead cells red. Scale bar represents 100 μm .

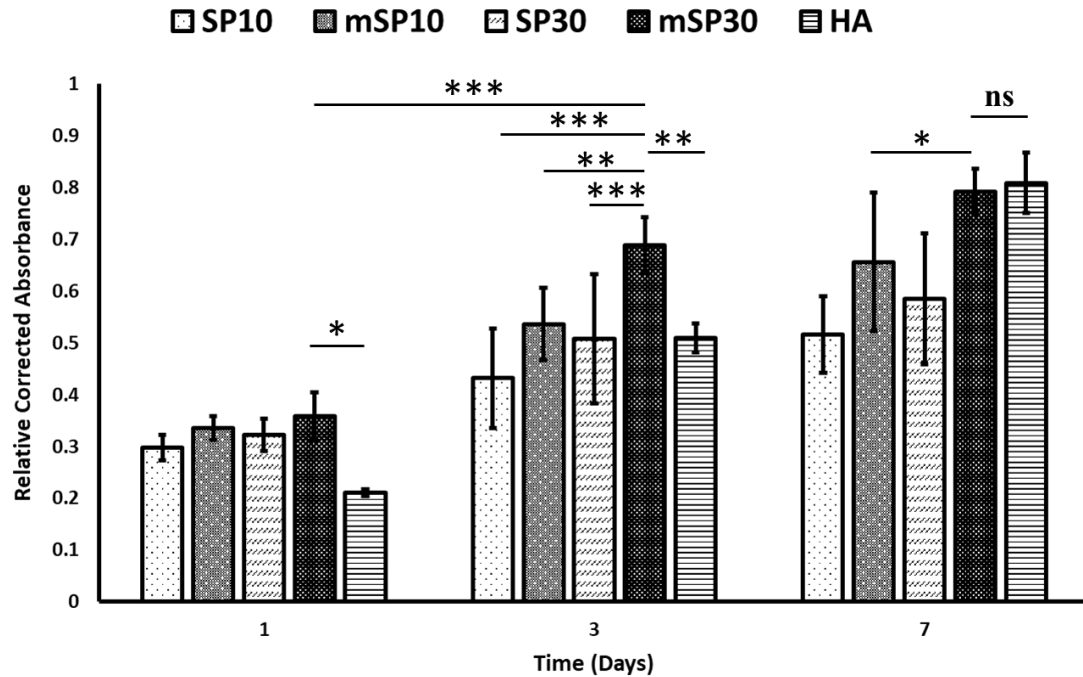


Figure 5-4. Differentiated MC3T3-E1 osteoblast cell proliferation on 3D printed nanocomposite discs; SP10 (10% nHA), mSP10 (methacrylated AESO and 10% nHA), SP30 (30% nHA), mSP30 (methacrylated AESO and 30% nHA) and HA (control). Proliferation of dMC3T3-OB cells as measured by XTT assay. Data are means \pm SD ($n = 8$ for nanocomposite discs and $n = 5$ for HA discs, from 4 experiments), (statistically significant $* p \leq 0.05$, $** p \leq 0.01$, $*** p \leq 0.001$).

The alkaline phosphatase assay was performed over 4 experiments. The data for the first two experiments are not shown as the samples were too diluted (1 ml collagenase/trypsin had been used for collecting cells). The data for the third and fourth experiments are shown in which 0.5 ml collagenase/trypsin was used to collect the cells for running the ALP assay (Figure 5-5). The amount of ALP expressed by the dMC3T3-OB cells by day 3 was decreased relative to day 1 ($p \leq 0.001$). The ALP amount on all nanocomposites except SP30 and HA control increased by day 7 compared to day 1 ($p \leq 0.01$). The effect of nanocomposite composition on ALP data was clearly visible by day 7. dMC3T3-OB cells on mSP10 and mSP30 nanocomposites expressed significantly higher ALP amount compared to SP10, mSP10, and HA discs ($p \leq 0.001$).

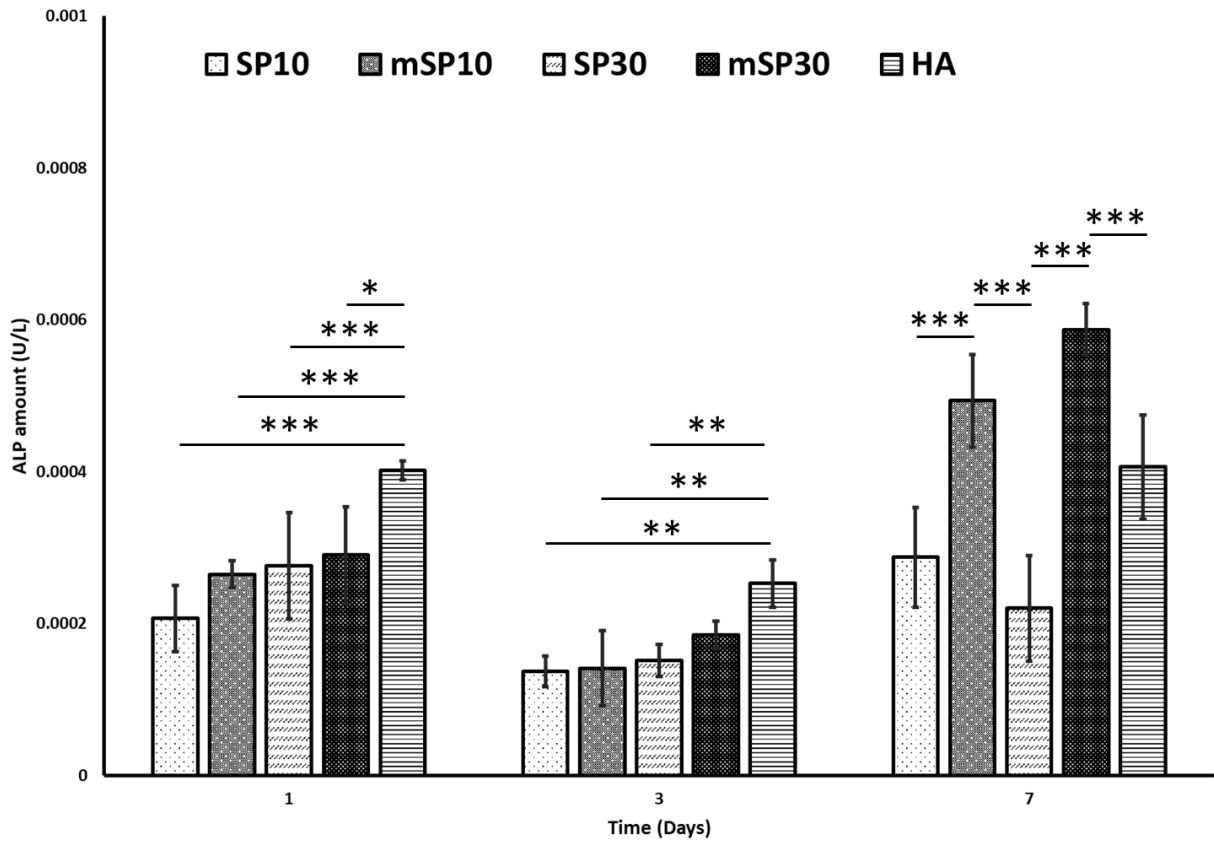


Figure 5-5. ALP expressed by differentiated MC3T3-E1 osteoblast cells cultured on the nanocomposite discs; SP10 (10% nHA), mSP10 (methacrylated AESO and 10% nHA), SP30 (30% nHA), mSP30 (methacrylated AESO and 30% nHA) and HA (control). Data are presented as mean \pm SD ($n = 4$ specimens of each composition and $n=3$ for HA control, from 4 experiments), (statistically significant * $p \leq 0.05$, ** $p \leq 0.01$, *** $p \leq 0.001$).

The amount of ALP is generally reported as ALP activity, which is normalized to the cell number using the amount of DNA from the picogreen assay [187], [211], [212]. The picogreen assay was not performed in this study, and therefore ALP activity was calculated as the amount of ALP normalized to the XTT data, as XTT data can be related to cell number (Figure 5-6). The ALP activity on day 1 on the HA discs was significantly different from the nanocomposites ($p \leq 0.001$). After 7 days, the ALP activity was decreased significantly for SP30 and HA discs ($p \leq 0.001$). On day 7, the ALP activity on mSP10 and mSP30 were significantly higher than the SP30 discs ($p \leq 0.01$). The two-way ANOVA analysis showed that there was a significant difference within composition and time-points, and the interaction between composition and time was significant ($p < 0.001$) which means our different compositions were creating different responses over time.

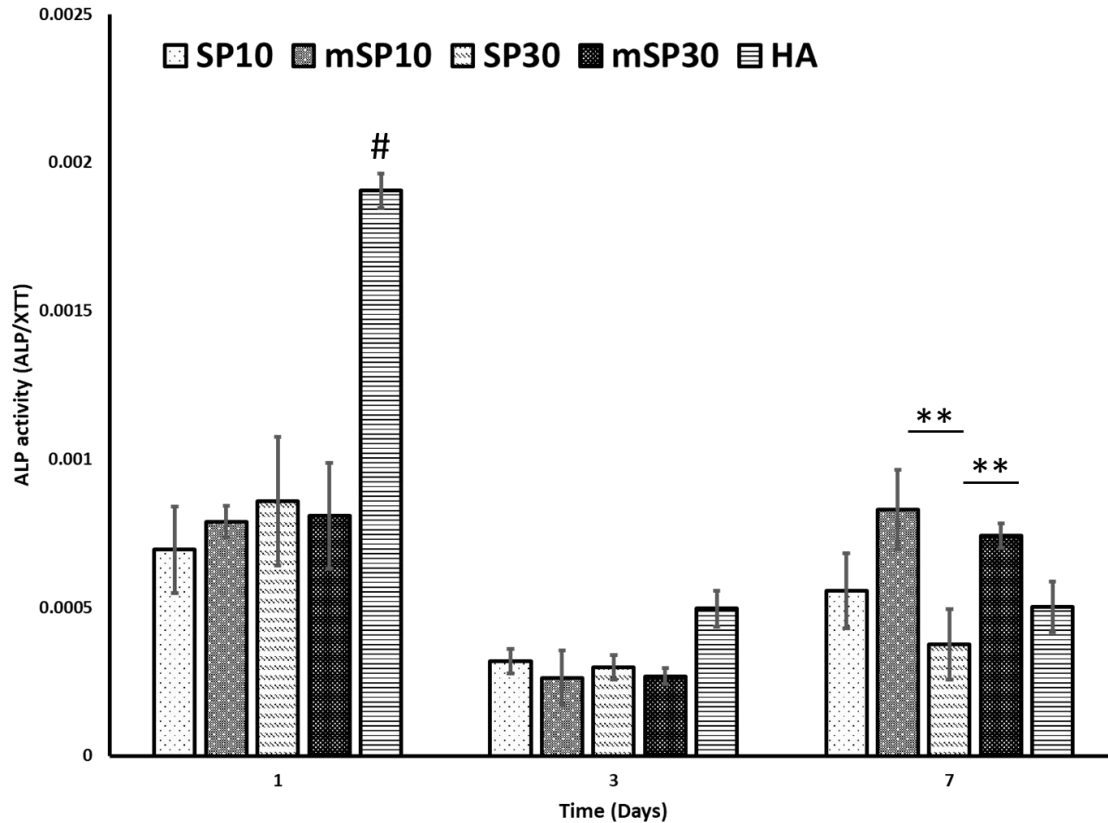


Figure 5-6. ALP activity of dMC3T3-OB cells cultured on the nanocomposite discs; SP10 (10% nHA), mSP10 (methacrylated AESO and 10% nHA), SP30 (30% nHA), mSP30 (methacrylated AESO and 30% nHA) and HA (control). The amount of ALP was normalized to XTT data. Data are presented as mean \pm SD ($n = 4$ specimens of each composition and $n=3$ for HA control, from 4 experiments), (statistically significant $** \leq 0.01$, statistically significant from all nanocomposites $\# < 0.001$).

5.3 Discussion

The MC3T3-E1 pre-osteoblast cells are widely used as a cell line to evaluate the biocompatibility of implantable biomaterials [213]. These cells are recognized as an osteoblast progenitor committed to a specific lineage [214] and MC3T3-E1 cells can only differentiate to osteoblasts [215], representing a good proxy for characterizing cell-material interactions with our nanocomposites. Mineral deposition capability is a late-stage marker of osteogenic differentiation used to confirm that the MC3T3-E1 cells had reached the mineralization phase to deposit mineralized ECM [216]. Fu *et al.* observed that Alizarin red staining of differentiated MC3T3-E1 cells was enhanced at day 21 on graphene oxide-impregnated poly (lactic-co-glycolic acid)-gelatin nanofibrous matrices in comparison to only slight reddish dots observed in cells at

day 14 [216]. This indicated that the osteogenic differentiation of MC3T3-E1 cells on their biomaterials increased by day 21 as more calcium content was identified (through Alizarin staining) in the deposited minerals. This confirmed our own observation for the differentiation of MC3T3-E1 cells and also highlights the importance of time in culture to allow the cells to lay down enough mineralized matrix to be detectable and measurable. Many studies [216]–[220] culture MC3T3-E1 cells on the surface of biomaterials with osteoblast differentiation medium. In this study, differentiated MC3T3-E1 cells (dMC3T3-OB) were seeded directly onto our nanocomposites to assess the ability of the nanocomposites to support osteoblast proliferation. While some studies have shown that differentiation may take place within 14 days [206][221], in accordance with previous studies on differentiation [215][222], dMC3T3-OB were obtained after differentiation for 21 days in this work.

The first step in the interaction of cells with substrate materials is cell attachment which can affect cell growth and proliferation on biomaterial surfaces [223][224]. Three factors affect cell behavior on polymer substrates: surface chemical, topological, and mechanical features [225]–[228]. Functional groups and grafted chains, surface characteristics and density of surface charges, surface energy, and adsorbing proteins' capability are considered chemical parameters [225]–[227]. Surface roughness and patterns at the micro- and nanoscales are related to topological factors [225]–[227]. The mechanical features of a polymer substrate, such as substrate stiffness, have also been linked to cellular functions. The actin-myosin interactions on the cell membrane can detect mechanical signals and transmit them to the nucleus, which can then adjust Ca^{2+} flux to control cell spreading, proliferation, and apoptosis [229]–[231].

HA can stimulate and enhance the proliferation of human and animal osteoblasts [219] and it was hypothesized that a higher amount of nHA in the AESO-based nanocomposites would increase the osteoblasts' adhesion, proliferation, and activity. Our results show that the addition of 10 vol% of nHA (SP10 nanocomposite) in the first study, and 30 vol% of nHA to the methacrylated AESO (mSP30 nanocomposite) in the second study, significantly increased cell viability and proliferation, verifying our hypotheses around the effect of nHA in the 3D-printed nanocomposites on osteoblast-like cells. Our results also further confirm previous studies that have shown that nHA promotes cell adhesion and proliferation.

The presence of exposed (i.e., on the surface) HA particles has been reported by Cia *et al.* [219] to impact surface chemistry, increasing hydrophilicity and protein adsorption with higher amount of HA. Ma *et al.* showed that adding nHA into polyetheretherketone (PEEK) also increased the composite's hydrophilicity (nHA is more hydrophilic than PEEK), which improved the functions of osteoblasts [222]. The effect of nHA on cells was studied by Lee *et al.* and suggested that nHA supported better initial attachment of MC3T3-E1 cells [232]. Furthermore, nHA has been reported to promote MC3T3-E1 cell attachment, proliferation, and differentiation on nanocomposites of photo-crosslinked poly(ϵ -caprolactone) diacrylate [219].

In this study, the ability of the nanocomposites to promote osteogenic differentiation of MC3T3-E1 cells was not evaluated because differentiated cells were directly seeded on the nanocomposites. Prior studies have demonstrated that HA is bioactive and can induce and enhance osteogenic differentiation of osteoblasts [219] on biomaterials, particularly nHA [170][233]. Further work is needed to characterize osteogenic differentiation on the nHA-AESO nanocomposites.

The other component in our novel nanocomposites is PEGDA. Son *et al.* investigated the potential of PEGDA as a hydrophilic co-monomer and crosslinker to increase biological properties of poly(N-isopropylacrylamide) hydrogels [234]. It has been found that PEG-based hydrogels have great biocompatibility, hydrophilicity, and able to prevent protein adsorption and cell adhesion [235][236]. In this regard, the addition of nHA and PEGDA would have made the nanocomposites more hydrophilic, making the surface more suitable for cell attachment and proliferation. In future work, the water contact angle should be measured to confirm the presumed hydrophilicity of our nanocomposites.

The addition of methacrylate groups to the AESO (mSP10 and mSP30) increased the proliferation and ALP activity of dMC3T3-OB cells compared to the non-methacrylated AESO-only composites. Our results corroborate the study of Sukul *et al.* [190], which reported that a higher degree of methacrylation in gelatin methacrylate hydrogels led to higher proliferation of primary human osteoblasts. Unlike our results, they showed that the expression of ALP in the primary osteoblasts was not affected by the degree of methacrylation of the hydrogels. The higher proliferation of cells on the mAESO nanocomposites might be

due to increased stiffness; the stiffness of the matrix enhances cell proliferation and the cytoskeleton of cells on stiffer matrices are more organized, and focal adhesions are more stable [229]. Nichol *et al.* found that increasing the degree of methacrylation increased the stiffness of gelatin methacrylate (GelMA) [237]. Increased stiffness due to methacrylation was also observed on our samples, with a modulus of 3.5 GPa and 10.8 GPa for SP30 and mSP30, respectively (personal communication, Dr D. Mondal, November 2021). Taken together, the higher cell viability, proliferation, and activity on the mAESO composites containing 30% vol nHA are likely due to the greater hydrophilicity (due to greater nHA volume fraction) and greater stiffness (due to methacrylation of the AESO) in the nanocomposites.

ALP expression and activity of dMC3T3-OB cells on our nanocomposites were measured. The ALP activity decreased on all samples by day 7 as cell growth and proliferation increased. Ascorbic acid and β -glycerophosphate have been reported to play essential roles in stimulating extracellular matrix formation, synthesis of osteoblast-related protein, and increasing alkaline phosphatase [238], [239]. In our study, the growth medium was supplemented with both ascorbic acid and β -glycerophosphate in higher concentration. Hence, the reduction in ALP activity is not due to a lack of nutrients. In [222], cultured MC3T3-E1 cells on nHA/PEEK composites showed ALP mRNA levels that increased after 14 days but decreased at day 21. Yazid *et al.* observed that MC3T3-E1 cell differentiation was significantly impacted by variations in cell seeding density, with lower initial seeding density resulting in increased ALP activity [215]. Increasing seeding density of mesenchymal stem cells increased cell viability and cell growth inhibition but resulted in reduction in cell function with higher density during cell culture. Therefore, these data suggest that in order to run a longer-term study to measure ALP activity on the nanocomposites, cell seeding density should be lowered.

As hypothesized, it was shown that AESO-based nanocomposites support osteoblast adhesion, proliferation, and activity. Furthermore, increased nHA volume fraction combined with methacrylation of the AESO resulted in an increase in dMC3T3-OB adhesion and proliferation; however, it did not affect ALP cell activity (ALP/XTT index). On the other hand, ALP activity results at day 7 indicate that

methacrylation of AESO increased dMC3T3-OB cell activity, presumably due to greater stiffness, as increased stiffness was observed between SP10 and mSP10 as well SP30 and mSP30.

6 Evaluation of dRAW-OC cells responses to the 3D-printed nanocomposite discs: results and discussion

In order to evaluate dRAW-OC cell interactions with our 3D-printed nanocomposites, RAW264.7 cells were differentiated, and isolated through serum gradient purification. dRAW-OC cells were cultured on SP30 and mSP30 discs to investigate the effect of methacrylation of AESO on cell response.

6.1 Characterization of dRAW-OC cells on SP30 and mSP30 nanocomposite discs

6.1.1 TRAP staining of dRAW-OC cells on nanocomposite discs

TRAP staining was used to assess the osteoclastic nature of the multinucleated cells on the SP30 and mSP30 nanocomposites after 7 days of culture and compared to HA controls. As shown in Figure 6-1, TRAP-positive cells were observed on the disc surfaces and TRAP-positive cells were bigger and in higher numbers on the mSP30 nanocomposite disc compared to SP30. It was challenging to compare TRAP staining with HA disc due to the poor visibility under light microscopy, as shown in the figure below.

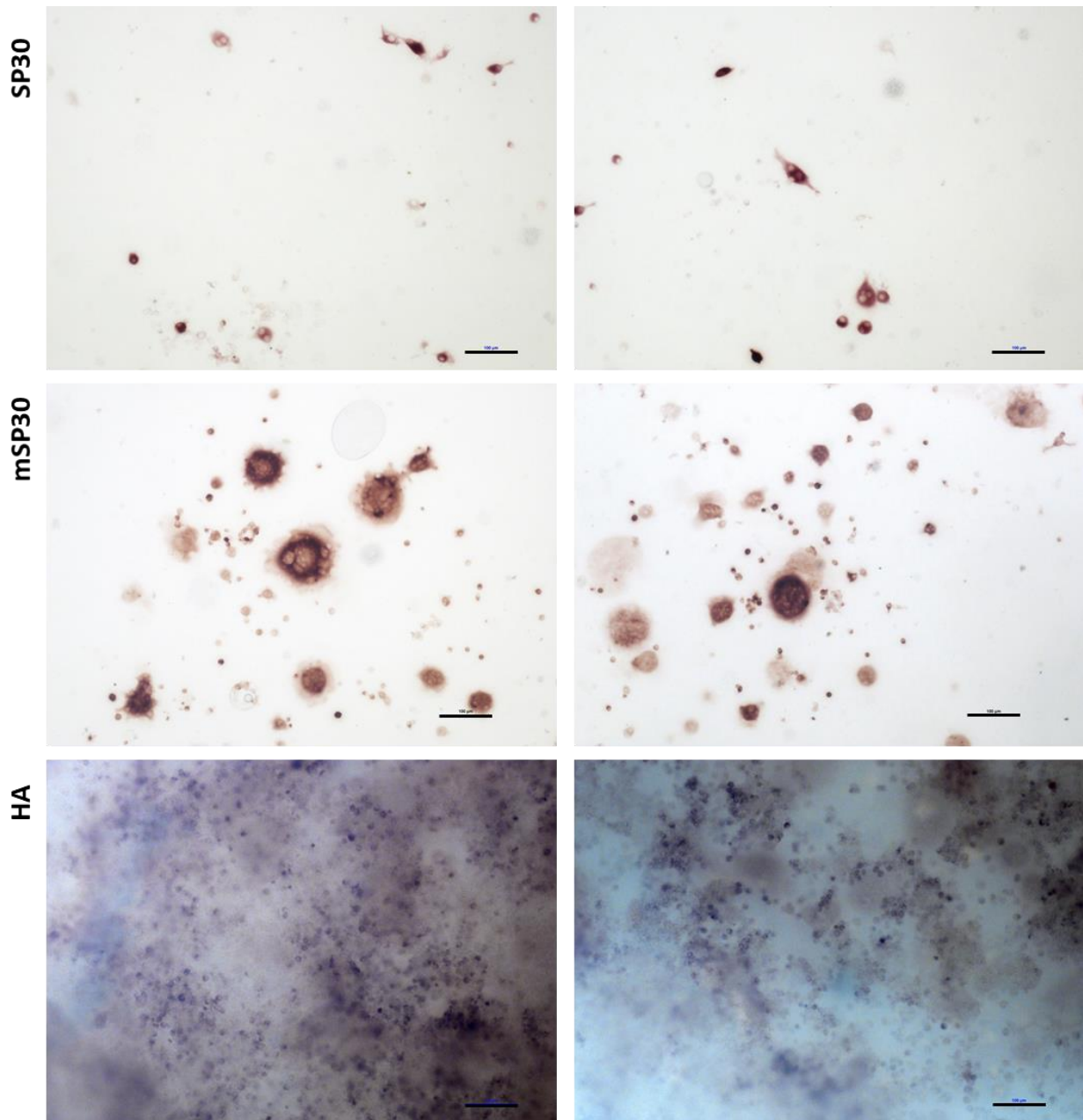


Figure 6-1. dRAW-OC cells were cultured on nanocomposite discs with RANKL for 7 days and stained for TRAP. Representative images of TRAP staining on SP30 (30% nHA), mSP30 (methacrylated AESO and 30% nHA) and HA (control) discs on day 7 ($n=3$). The TRAP staining of the dRAW-OC cells on the HA discs was challenging to observe due to background staining. Scale bar represents 100 μm .

6.1.2 F-Actin/DAPI staining of dRAW-OC cells on nanocomposite discs

The number of dRAW-OC cells on the two nanocomposites discs and the HA controls was measured. A significantly greater number of osteoclast-like cells was measured on mSP30 (average 174.67 osteoclasts/ cm^2) compared to SP30 (average 0.66 osteoclasts/ cm^2) ($p < 0.001$) and HA (average 63.33

osteoclasts/cm²) ($p < 0.05$). It is important to note that it was difficult to count all osteoclast-like cells on the HA disc due to excessive proliferation of macrophages that covered the multinucleated cells on the surface. Therefore, the number of osteoclast-like cells on the HA may be an underestimation. The number of nuclei in each osteoclast-like cell was counted and as shown in Figure 6-2, the average number of nuclei number on mSP30 and HA was significantly higher than that on the SP30 discs ($p < 0.05$). In order to count nuclei, images were taken in the green channel as it was impossible to quantify the nuclei in the blue channel (Figure 6-3).

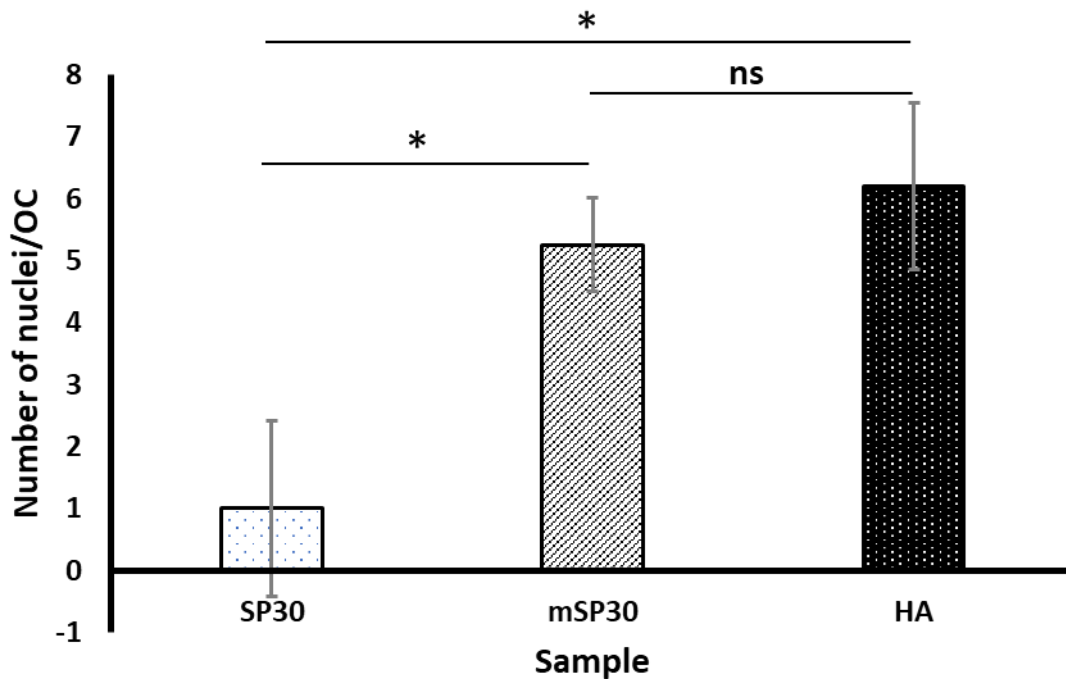


Figure 6-2. *d*RAW-OC cells were cultured on SP30 (30% nHA), mSP30 (methacrylated AESO and 30% nHA) and HA (control) discs for 7 days. Osteoclast-like cells were stained with DAPI and Alexa Fluor 488-Phalloidin, and the number of nuclei per osteoclast was counted (3 discs per composition, on average 87 osteoclasts for mSP30, 32 for HA and 1 for SP30 on discs).

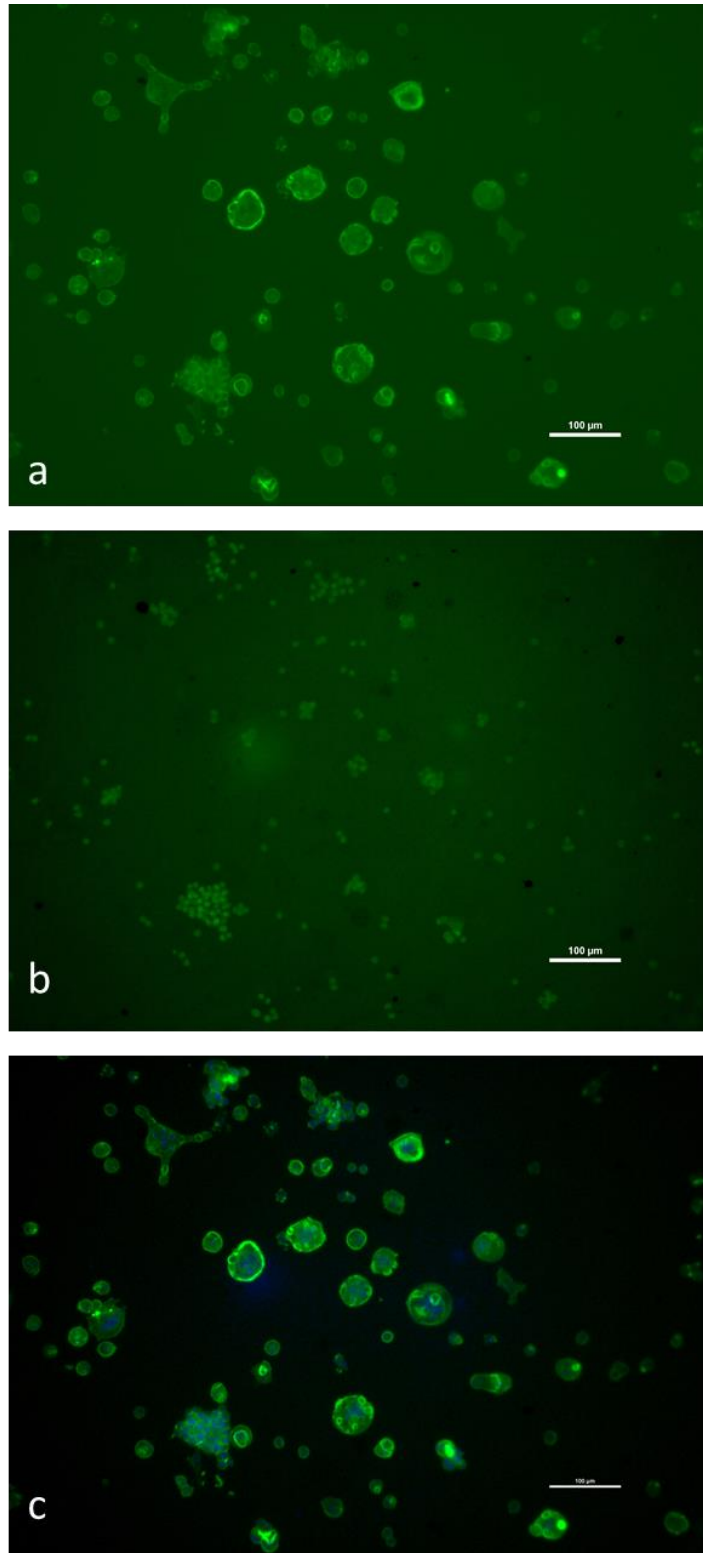


Figure 6-3. Morphology evaluation of osteoclast-like cells on mSP30 (methacrylated AESO and 30% nHA) nanocomposite disc. dRAW-OC cells were stained with a) Alexa Fluor 488-Phalloidin (for the visualization of F-actin filaments), b) DAPI staining (for the visualization of the cell nuclei) imaged in the green channel, and c) merged green and blue channels. (scale bar represents 100 μm)

Mature osteoclasts form clusters of dynamic, F-actin-rich adhesion structures with integrin receptors called podosomes that self organize into actin rings at the cytomembrane periphery [240]. We observed the effects of composition on actin ring formation using phalloidin staining (which binds to F-actin) in combination with a nuclear stain (DAPI) to confirm the presence of multiple nuclei. As shown in Figure 6-4, dRAW-OC cells, with multiple nuclei, formed F-actin rings on mSP30 and HA discs. The sizes of actin rings on mSP30 and HA discs were similar but were significantly different from SP30 discs. As shown in Figure 6-5, dRAW-OC cells formed significantly larger actin rings on mSP30 and HA than dRAW-OC cells on SP30 ($p < 0.05$).

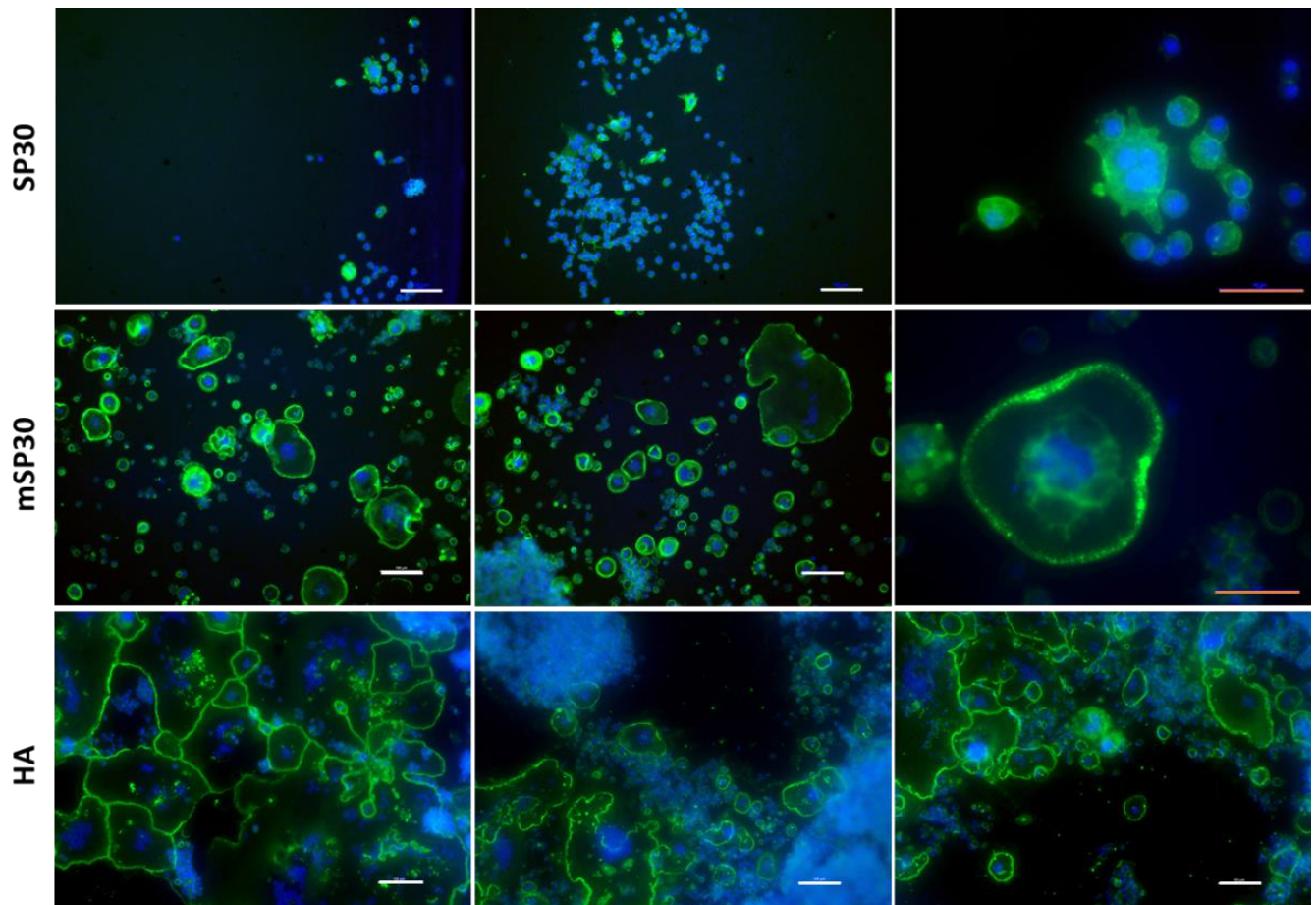


Figure 6-4. Morphological evaluation of osteoclast-like cells cultured on SP30 (30% nHA), mSP30 (methacrylated AESO and 30% nHA) and HA (control) discs, stained with DAPI (for the visualization of the cell nuclei) and Alexa Fluor 488-Phalloidin (for the visualization of F-actin filaments) ($n=3$). White and red scale bars represent 100 μm and 50 μm , respectively.

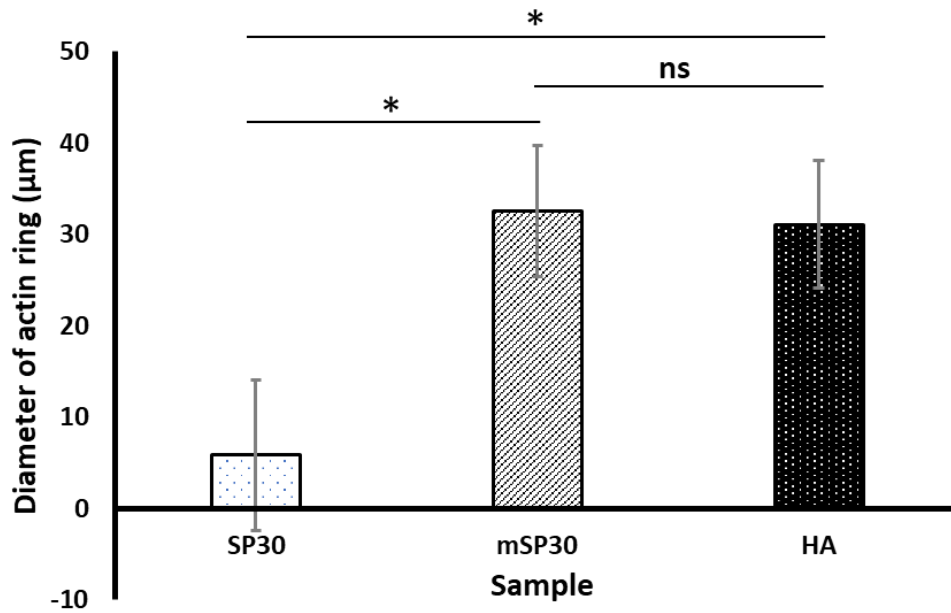


Figure 6-5. dRAW-OC cells were cultured on SP30 (30% nHA), mSP30 (methacrylated AESO and 30% nHA) and HA (control) discs for 7 days. Osteoclast-like cells were stained with DAPI and Alexa Fluor 488-Phalloidin, and the diameter of actin rings on multinucleated cells was determined (3 discs per composition).

6.1.3 Calcein staining of nanocomposite's surface to observe resorption pits

dRAW-OC cells were seeded on the surface of non-porous nanocomposite discs and cultured for 7 days. After removing the cells, the surface was stained with calcein to assess the formation of osteoclast-mediated resorption pits. For each specimen, a control with no cells was also included whereby the disc was treated and sterilized in the same manner and incubated in culture medium without RANKL (to reduce cost) at 37°C, 5% CO₂. As shown in Figure 6-6, no resorption pits on nanocomposite discs, SP30 and mSP30, and HA were identified with calcein staining. A pit-like shape was observed on one SP30 disc; however, this was identified as a defect from 3D-printing as similar pit-like structures could be observed on the control disc (no cells). Similarly, pit-like structures were observed on HA discs with and without cells, suggesting that no osteoclast-mediated resorption pits had formed on HA after 7 days of culture.

While we were unable to obtain an osteoclast-mediated resorption pit, a confocal image of a pit-like structure was obtained as a proof-of-concept to perform image analysis and volume calculation (Figure 6-7). The calcein staining of the surface enabled us to visualize the pit on the nanocomposite discs. The pit

and its depth can be viewed in slice, tiled, and 3D view in NIS-Elements AR software. In Figure 6-8, the intensity profile of the surface is shown.

For measuring the volume, first the area of the pit was measured by using the draw function in the ImageJ software. The highest visible point is on frame 7, and the lowest visible point is on frame 21. The area for each frame was calculated and their sum was $31836.55 \mu\text{m}^2$. This number was multiplied by 2.98 micron (the distance between each frame), and the volume of the pit shown in Figure 6-7 is $94872.91 \mu\text{m}^3$.

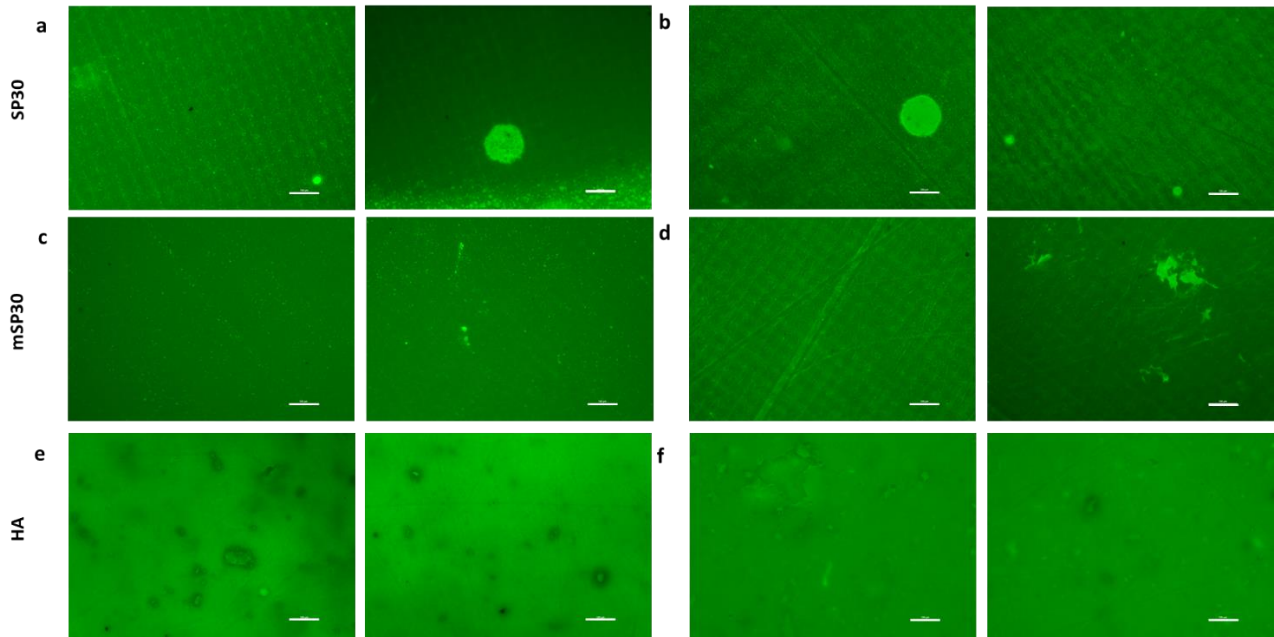


Figure 6-6. Representative images of calcein staining of nanocomposite discs ($n=4$) by fluorescence microscope. *dRAW-OC* cells were cultured on SP30 (30% nHA), mSP30 (methacrylated AESO and 30% nHA) and HA (control) discs for 7 days. Cells were removed from the surface and discs were stained with calcein (a, c, e). SP30, mSP30, and HA control discs were incubated in media only (no cells) (b, d, f). Scale bar represents $100 \mu\text{m}$.

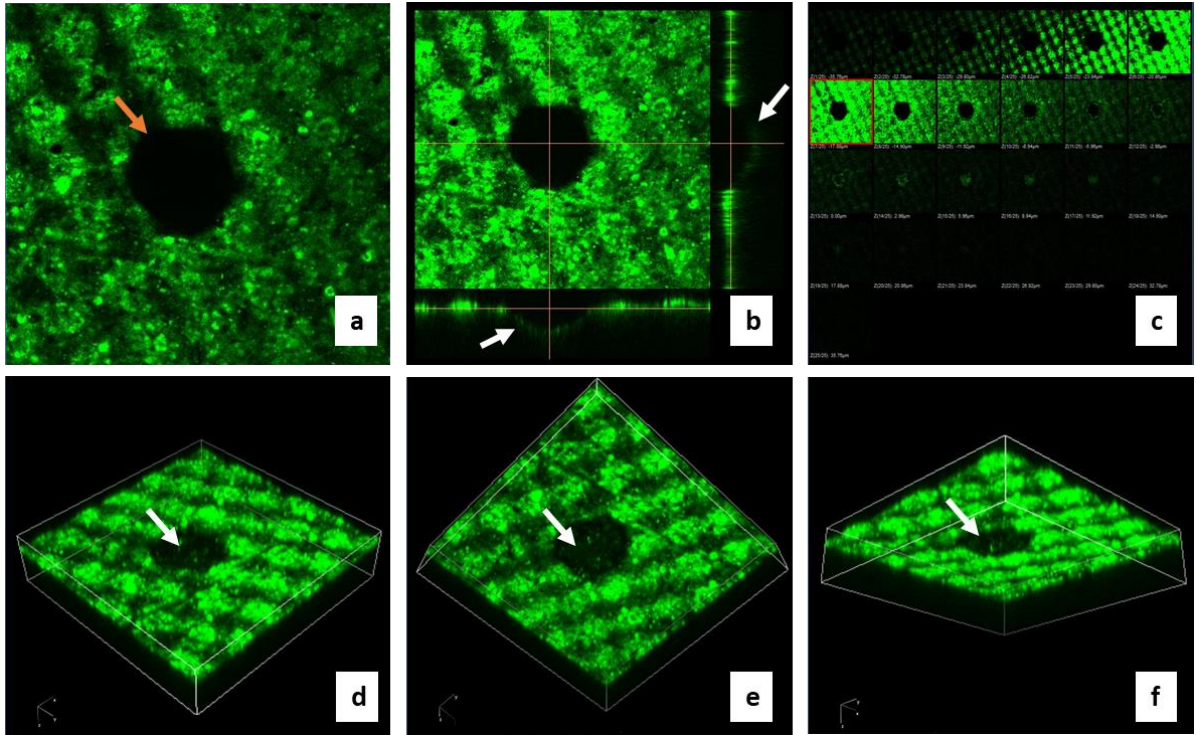


Figure 6-7. Pit 3D visualization by confocal microscopy on SP30 (30% nHA) disc. Calcein staining was done, and confocal image stacks of fluorescence were collected. (a) Orange arrow shows the pit on the surface. (b) Slice view showing depth of pit with white arrows. (c) Montage showing a sampling of single plane images (frames 1–25) collected at 2.28 μm z-steps. (d, e, f) Volume view of pit.

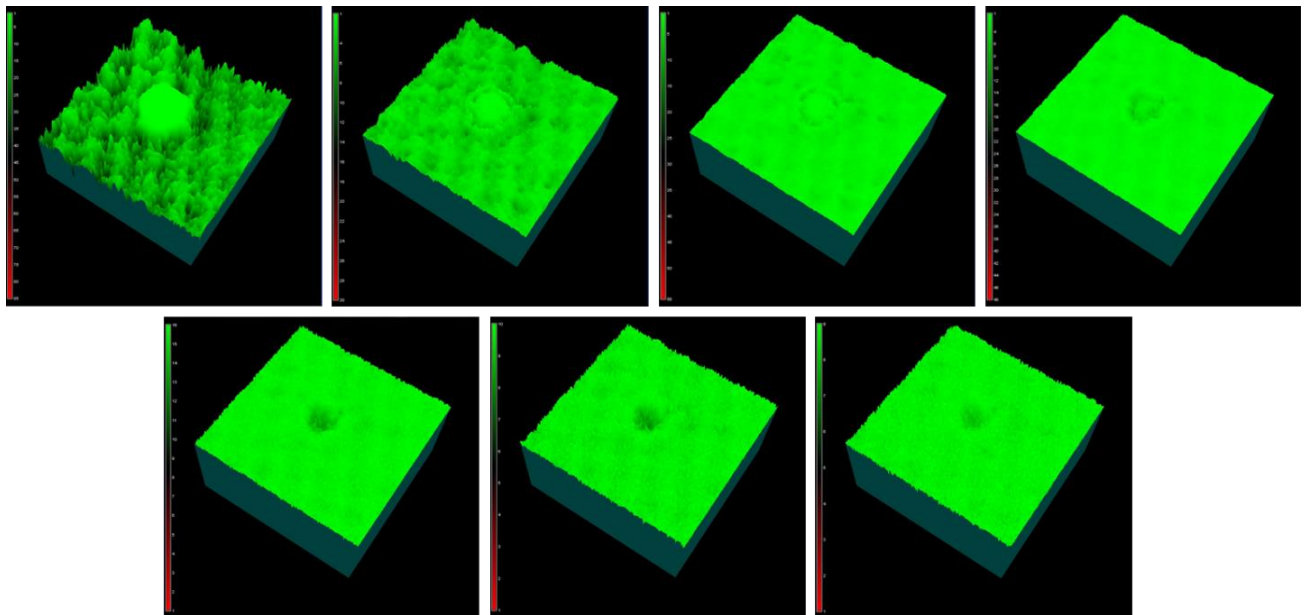


Figure 6-8. Pit 3D visualization by confocal microscopy on SP30 (30% nHA) disc. Intensity surface profile showing the pit on the disc.

6.2 Discussion

The concept of using osteoclasts to resorb bone graft materials while also directing new bone formation and vascularization is based on bone biology principles [241]. This is the first study of osteoclast interactions with AESO and mAESO-based nanocomposites. Many studies [29], [40], [68], [242], [243], [244] have cultured RAW264.7 cells on the surface of biomaterials with osteoclasts differentiation medium to assess osteoclast differentiation and cell-material interactions. In this study, RAW 264.7 macrophages were differentiated first, purified, and the resulting dRAW-OC cells were seeded directly onto our nanocomposites to directly assess the interaction of osteoclasts with the nanocomposites and their resorbability by osteoclast activity. Different material may not support osteoclast differentiation to the same extent and this variability was removed by seeding osteoclasts directly on the surfaces of our novel biomaterials.

As this was the first time differentiated osteoclasts were used in our research group, the protocol needed some optimization. Among others, based on our seeding density, RANKL concentration was adjusted to 30 ng/ml as Song *et al.* reported that different commercial media and RANKL may result in a different dosages of stimulator required for osteoclast induction [81]. Furthermore, several cell culture times and seeding densities were tested. Density-gradient purified dRAW-OC were seeded at 5×10^4 cells/cm² with 30 ng/ml RANKL and cultured for 14 days. Significant color change (indicating increase acidity in the medium) was observed in the medium starting at day 7 and samples were thus removed from the silicone tube to allow for more medium to be added and ensure cells had enough nutrients. On day 14, F-actin and nuclei staining was performed, and no cells were observed on the nanocomposites tested (in these pilot studies, AESO, SP0, and SP30 discs) and excessive numbers of non-multinucleated cells were seen on the HA. In a follow-up experiment, lower cell concentration (1×10^4 cells/cm²) was used and XTT and SEM were performed to assess cell proliferation (2, 7, and 14 days) and morphology (14 days) (see Appendix 2 for more details). Due to cell death observed on day 14 on HA, interaction with the biomaterials was limited to 7 days in all further experiments. Results with HA concurred with Chen *et al.*, where massive cell apoptosis occurred after 7 days [245]. Furthermore, they also observed resorption

pits on HA discs at day 6-7 of culture, suggesting that this was a reasonable time frame for our experiments. Based on this and our observations from the osteoblast study and the better mechanical properties of the methacrylated nanocomposites, SP30 and mSP30 nanocomposites were thus chosen for a 7-day osteoclast study.

Nanocrystalline HA and human bone mineral show similar interactions with osteoclasts and osteoblasts and thus, nanocrystalline HA can be used as a synthetic material similar to natural bone in order to improve a variety of orthopedic applications [246]. When compared to the HA control biomaterial, mSP30, containing 30% nHA, showed similar or even better interaction with osteoclasts, further suggesting the value of this nanocomposite for bone applications.

Osteoclast numbers, the presence of an actin ring and resorption pits are important measures of OC development and activity that have not yet been investigated on AESO/nHA-based nanocomposites. Our results showed that there was a significantly higher number of dRAW-OC cells on mSP30 and HA than on the SP30 nanocomposite. It is possible that differences in surface roughness may have led to such a difference, as Zhang *et al.* demonstrated that osteoclasts are sensitive to surface roughness [209]. They found that smoother surfaces induced more osteoclast differentiation than rougher surfaces, as shown by increased TRAP activity and higher gene expression of osteoclastogenic markers [209]. Prior studies also claimed that greater surface roughness reduced osteoclast-associated parameters such as TRAP activity and resorption capability [247], [248]. Based on these studies, we may hypothesize that the reduced adhesion of osteoclasts on SP30 may be due to a rougher surface, but this should be confirmed by AFM. The methacrylation may also lead to a smoother surface or may induce a specific response in osteoclasts. One may also hypothesize that the increase in osteoclast adhesion and viability on mSP30 was due to increased stiffness, since, as discussed in section 5.3, mSP30 is stiffer than SP30 ($E_{SP30} = 3.47$ GPa, $E_{mSP30} = 10.81$ GPa) and that increase in stiffness has been reported to lead to higher bone cell viability and proliferation. However, such effect of stiffness has only been reported for osteoblasts [190].

The effect of roughness has also been shown to play an important role on the actin ring. Functionality of osteoclasts depends on the podosome belt which has an actin-rich integrin adhesion

structure that allows tight adhesion of osteoclasts to the bone surface. The formation of the podosome belt is strongly dependent on the local environment [249]. In [209], on smoother surfaces, larger actin rings were identified, whereas on rougher surfaces, smaller actin rings were detected. The surface roughness was also reported to affect the number of nuclei per osteoclast and size and number of osteoclasts. Smoother surfaces had a higher number of nuclei per osteoclasts, larger size but a smaller number of osteoclasts than rougher surfaces [209]. The larger size is explained by the fact that there are no topographical features on smoother surfaces that impede cell fusion process; as a result, cells efficiently fuse to make fewer and bigger osteoclasts [250]. The higher number of nuclei and larger actin rings observed on mSP30 and HA but not SP30 may be explained by a difference in surface roughness, however as mentioned above, this needs to be confirmed by AFM. An important point to note is that Zhang *et al.* also observed that primary osteoclasts on glass surface did not show actin rings, possibly due to a short-lived actin ring formation [251]. The actin ring might appear and disappear on the glass after 4 days of osteoclastogenic induction. This observation underlines the importance of culture protocols and treatment time when studying osteoclasts and suggest that our protocols for the nanocomposites were well defined, as we were able to observe the actin ring during our cell culture experiments.

While many osteoclasts with actin rings were observed on mSP30 and HA, no resorption pits were identified. Chen *et al.* have reported that nano-topography may impair the stability of the sealing zones for resorption [245] and thus affect the formation of resorption pits due to “leakage”. However, this study [245] and another [252] also indicated that nano-structured HA discs compared to the submicron-scale dimension significantly impaired osteoclastic formation and function, as seen by inhibited cell fusion, reduced osteoclast size, less-defined actin ring, increased osteoclast apoptosis, suppressed expression of osteoclast specific genes and proteins, decreased TRAP-positive cells [245], which contradicts our observation with mSP30, showing excellent osteoclast survival, defined actin rings and large multinucleated osteoclasts. Thus, the sealing zones may be stable and other factors could be at play. If nHA leads to resorption impairment, dRAW-OC cells could be cultured on mSP10 and mSP30 nanocomposite discs to further characterize the effect of nHA in nanocomposite composition.

Osteoclasts secrete reactive oxygen species (ROS) during bone remodeling. A prior study by Lu et al has shown that nanocrystalline hydroxyapatite-lysine triisocyanate (nHA-LTI) nanocomposite degraded faster than LTI-poly(ϵ -caprolactone) triol polymer in oxidative medium (20% H_2O_2 + $CoCl_2$), which was consistent with the observed resorption of nHA-LIT by osteoclasts [29]. Thus, assessing the oxidative degradation rate can help in evaluating the potential resorption rate by osteoclasts. In our previous study on biodegradation of AESO-based nanocomposites containing 0%, 5%, and 10% nHA in oxidative medium, no significant biodegradation was observed after 28 days, suggesting limited oxidative degradation of the nHA nanocomposites [198]. While we have not yet performed a degradation study in oxidative medium, the lack of resorption pits on mSP30 may be due to a low oxidative degradation after 7 days.

The lack of resorption pits on our control HA material was unexpected. The adhesion, cytoskeletal changes and resorptive activity of rat osteoclasts on crystalline synthetic hydroxyapatite (HA), carbonated hydroxyapatite (C-HA) and natural calcium carbonate (C) have been investigated previously by Redey *et al.* [253]. Actin rings, which are essential for resorption and were also observed on our HA material, developed on all three biomaterials tested. The size of the actin ring and osteoclast spreading were higher in osteoclasts cultured on HA and C-HA than C. Interestingly, despite this, HA and C-HA were not resorbed, while C was. This was believed to be directly related to the biomaterial's solubility. Further characterization of the HA discs by Dr. Dibakar Mondal showed that these discs were 100% crystalline which explains a lack of resorption of our control HA biomaterial.

HA and mSP30 supported dRAW264.7 cells adhesion and differentiation as evidenced by the presence of a cell population with TRAP activity and multinucleated cells with well-defined actin rings. However, foreign-body multinucleated giant cells (FBGCs), another multinucleated cell type, are frequently generated at implant/graft sites and related to foreign-body responses. FBGCs are formed by the fusion of monocytes/macrophages, and hence have many properties similar to osteoclasts, such as multinuclearity, TRAP expression, and actin rings [254]. The main difference between these two cell types is that only osteoclasts express the matrix-degrading enzyme, Cathepsin K (CTSK) [254]. Thus, it is also possible that our differentiated RAW cells were not osteoclast but FBGCs. While we should confirm the

osteoclast phenotypes of our differentiated cells by measuring their CTSK gene expression, the lack of resorption pits is an indication that the nanocomposites could not undergo cell-mediated degradation as FBGCs also release degradation enzymes [255].

We assessed the utility of calcein as a marker for staining the nanocomposite discs and established that this fluorescent probe is suitable for visualizing resorption pits on the surface. The idea of staining the surface and visualizing the pit was obtained from Goldberg *et al.* study which used confocal imaging technique to image resorption lacunae stained with Picro Sirius Red on dentin slices [68]. In our study, there were no osteoclast-mediated resorption pits observed on the surface of nanocomposite discs. The confocal microscope and NIS-Elements AR software will enable us to observe any pits on the surface and the Extended Depth of Focus (EDF) module will eventually be needed to do volume rendering of the confocal image stack using z-depth color coding which reveals the three-dimensional shape of the Rpit and allow for the measure of its volume. The current pit that was measured had no three-dimensional shape as it was a simple hole due to a printing defect; as previously reported by Goldberg *et al.* an osteoclast-mediated resorption pit will have a complex/uneven structure, which volume will not be as easily calculated with the current approach [68].

7 Conclusion, Limitations, and Recommendation for Future Work

7.1 Conclusion

The results presented in Chapter 5 and 6 verified most of the hypotheses that were presented in Chapter 3. The increasing nHA concentration in the nanocomposites improved osteoblast-like cell viability, proliferation, and activity, verifying our hypothesis 1.2. Osteoblast-like cell-interactions with our 30% nHA composite (SP30) were comparable to the HA control (related directly to hypothesis 1.1). Moreover, the additional functionalization of AESO (through methacrylation of residual hydroxyl group) resulted in a significant effect with higher cell adhesion and proliferation, although it didn't have detectable effect on the cell activity, as measured by ALP (Hypothesis 1.3). At all time points (except day 1 and 3 for ALP/XTT index), mSP30 performed similarly or even better than HA when interacting with the osteoblast-like cells, dMC3T3-OB (Hypothesis 1.1). In the osteoclast study, compared to the AESO-based nanocomposite SP30, the mAESO-based nanocomposite showed significantly greater cell adhesion, actin ring formation and multinucleated cells, comparable to HA controls (Hypotheses 2.1 and 2.2).

In conclusion, osteoblast-like and osteoclast-like cells showed excellent interactions with the mAESO-based composite containing 30% nHA. These interactions were comparable to the HA controls. This suggests the future suitability of our novel nanocomposites as implantable biomaterial for reconstruction of large bone defects upon further development. *In vivo* studies will be required to conclude on the potential of our nanocomposites. Osteoclast-mediated resorption pits did not form on any of our materials (AESO, mAESO, HA), suggesting that further work is required to better understand the limitations of our current experimental model and of the biomaterials being tested.

7.2 Limitations

While this thesis makes significant contributions in the area of protocol development and identification of suitable nanocomposite biomaterials for critical-size bone defects, there are limitations to the studies that should be noted.

One of the major limitations of our *in vitro* experiments was the sole use of bone cell lines to assess cell-material interactions. As these cells have infinite growth potential, in the osteoclast study, although serum gradient purification was performed to isolate differentiated cells, non-differentiated RAW264.7 cells (macrophages) on the discs were continuously observed on the discs and they proliferated over time despite the presence of the differentiating agent RANKL. Similarly, in the osteoblast study, while dMC3T3-OB cells were frozen after differentiation, the stage of differentiation (maturity of the cells) was not assessed and as proliferation was observed in our experiments, the dMC3T3-OB may not have been fully differentiated. While this does not affect the conclusion of our studies around cell-material interactions, a better understanding of the maturity state of the cells after freezing would be valuable information.

In this study, a single cell type was cultured on nanocomposites to study the interaction of cells with biomaterials. Several studies [256][257][258] have highlighted the importance of cross-talk between osteoblasts and osteoclasts *in vitro* and the mechanism of molecular cooperation in order to mimic bone turnover.

There are different factors affecting bone formation, bone resorption, and bone remodeling such as blood components (platelet factors, leukocyte inflammatory molecules), different enzymes, and mechanical stimuli [259]–[261]. All the experiments in this study were done under static conditions, in the absence of any exogenous inflammatory factors, which have been shown previously to play a role in bone cell-material interactions.

The 3D printed biomaterial discs were non-porous, and thus cells were not cultured on porous material, or scaffold, with a homogeneous interconnected pore network, which is not only useful for tissue engineering but also better mimic the physiological structure of bone.

In vitro tests are only a first step in the evaluation of a biomaterial, and pre-clinical animal trials are required en route to clinical trial to finally prove a biomaterial and the clinical procedure associated. In the *in vivo* experiments, the condition is not static and the effect of different factors such as exogenous inflammatory factors on cell-material interactions can be investigated.

7.3 Recommendation and Future Works

Based on the identified limitations of the studies as well as the results of the studies, there are many questions that remain unanswered and thus the following recommendations for future work are presented.

- The *in vitro* model to characterize cell material interaction can be further improved by developing a co-culture model and/or a model that allows for cells to be mechanically stimulated.
- *In vitro* experiments should be performed with human primary cells in addition to immortalized cell lines. Although primary cells have a limited lifespan, it offers some advantages compared to cell lines including consideration of age, medical history, race, and sex of donors.

For the osteoblast study:

- Osteogenic differentiation should be assessed by culturing and differentiating MC3T3-E1 cells on nHA-(m)AESO nanocomposites. While it is important to assess the interactions with osteoblast cells, differentiation of progenitor cells also plays an important role in biocompatibility and thus should be assessed.
- Osteoblast-like cells should also be seeded at lower density in order to run longer-time studies to better assess ALP activity.
- As hydrophilicity and surface roughness may play a role in bone cell-material interactions, characterizing these properties of the 3D printed nanocomposite discs should become standard practice in order to understand the plausible role of surface properties.
- Also, Picogreen assay is needed to perform quantitative analysis of DNA. This provides the accurate number for ALP activity as the ALP amount should be normalized to corresponding DNA content from the Picogreen assay.

For the osteoclast study:

- Culture of dRAW-OC cells on SP10 and mSP10 should be performed in order to determine the effect of a lower nHA amount in comparison to the mSP30 nanocomposite.

- The expression of digestive enzymes such as Cathepsin K by dRAW-OC cells should be measured to distinguish these cells from foreign-body multinucleated giant cells.
- The expression of integrins, such as $\alpha_v\beta_3$ could be characterized to confirm the attachment of dRAW-OC cells to the biomaterial surface and a sealed zone for the formation of resorption pits.
- Due to the limitations encountered with the HA control disc in relation to resorption pits (no pits detected), the ability of dRAW-OC cells to resorb bone should be confirmed by culturing these cells on Osteo Assay Surface plate (a commercially-available plate designed for resorption assays).
- The oxidative degradation of SP30 and mSP30 should also be evaluated to further confirm if the nanocomposites are susceptible to such degradation.
- The nanocomposite could be designed to undergo controlled resorption by osteoclasts [262] by incorporating a Cathepsin K peptide or Matrix Metalloproteinases into the nanocomposite. A volume-based method should be developed to do the depth and volume measurements of resorption pits using calcein staining.

Letter of Copyright Permission

Figure 1-1:

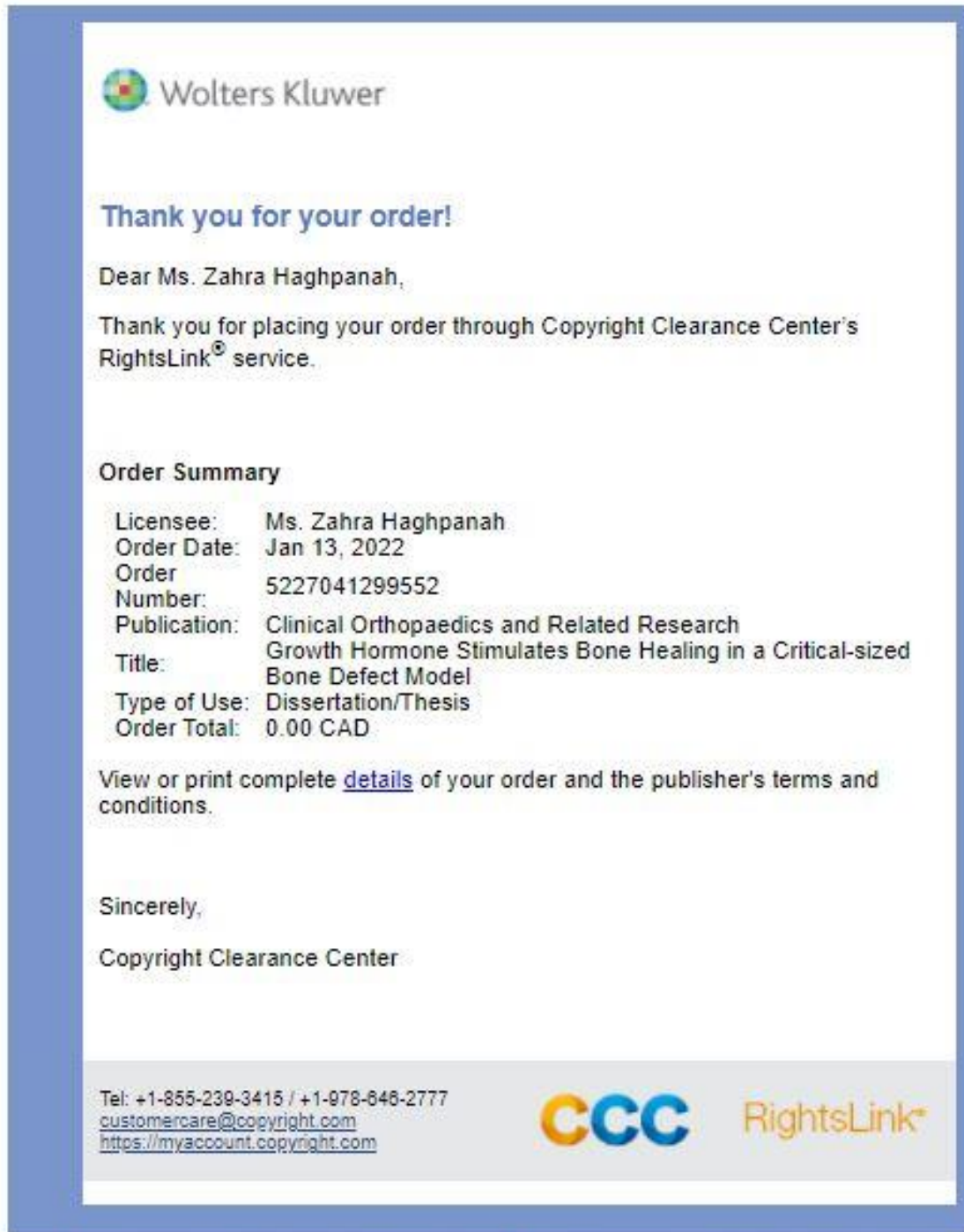


Figure 1-2-a:

Illustration of an autograft harvested from iliac crest.

 [BruceBlaus](#). When using this image in external sources it can be cited as: Blausen.com staff (2014). "Medical gallery of Blausen Medical 2014". *WikiJournal of Medicine* 1 (2). DOI:10.15347/wjm/2014.010. ISSN 2002-4436. - Own work

Bone Graft. See a [related animation](#) of this medical topic.

Permission details

This work is **free** and may be used by anyone for any purpose. If you wish to **use this content**, you do not need to request permission as long as you follow any licensing requirements mentioned on this page.

The Wikimedia Foundation has received an e-mail confirming that the copyright holder has approved publication under the terms mentioned on this page. This correspondence has been **reviewed** by a [Volunteer Response Team \(VRT\) member](#) and stored in our [permission archive](#). The correspondence is available to trusted volunteers as **ticket #2013061010006654**.

If you have questions about the archived correspondence, please use the [VRT noticeboard](#). Ticket link: <https://ticket.wikimedia.org/otrs/index.pl?Action=AgentTicketZoom&TicketNumber=2013061010006654>

Figure 1-2-b:

Summary [\[edit\]](#)

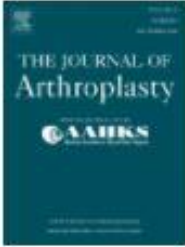
Description	English: A upper right femur Bone-allograft with associated tissues around the hip joint.
Date	17 June 2009
Source	Own work
Author	BennyK95

Licensing [\[edit\]](#)



I, the copyright holder of this work, release this work into the **public domain**. This applies worldwide.
In some countries this may not be legally possible; if so:
*I grant anyone the right to use this work **for any purpose**, without any conditions, unless such conditions are required by law.*

Figure 1-2-c:



Thank you for your order!

Dear Ms. Zahra Haghpanah,

Thank you for placing your order through Copyright Clearance Center's RightsLink® service.

Order Summary

Licensee:	Ms. Zahra Haghpanah
Order Date:	Jan 13, 2022
Order Number:	5227051128534
Publication:	The Journal of Arthroplasty
Title:	The Influence of the Alloy of Megaprotheses on Infection Rate
Type of Use:	reuse in a thesis/dissertation
Order Total:	0.00 CAD

View or print complete [details](#) of your order and the publisher's terms and conditions.

Sincerely,

Copyright Clearance Center

Tel: +1-855-239-3415 / +1-978-646-2777
customer@copyright.com
<https://myaccount.copyright.com>



Figure 2-1:



Thank you for your order!

Dear Ms. Zahra Haghpanah,

Thank you for placing your order through Copyright Clearance Center's RightsLink[®] service.

Order Summary

Licensee: Ms. Zahra Haghpanah
Order Date: Jan 13, 2022
Order Number: 5227011146018
Publication: Medical Engineering & Physics
Title: Mechanical properties and the hierarchical structure of bone
Type of Use: reuse in a thesis/dissertation
Order Total: 0.00 CAD

View or print complete [details](#) of your order and the publisher's terms and conditions.

Sincerely,

Copyright Clearance Center

Tel: +1-855-239-3415 / +1-978-648-2777
customer-care@copyright.com
<https://myaccount.copyright.com>

 RightsLink[®]

Figure 2-2:

Open Access Review

Mechanical Properties of Compact Bone Defined by the Stress-Strain Curve Measured Using Uniaxial Tensile Test: A Concise Review and Practical Guide

by  Che-Yu Lin ^{1,*}  and  Jiunn-Horng Kang ^{2,3,4,*} 

¹ Institute of Applied Mechanics, College of Engineering, National Taiwan University, No. 1, Sec. 4, Roosevelt Road, Taipei 10617, Taiwan

² Department of Physical Medicine and Rehabilitation, Taipei Medical University Hospital, 252 Wuxing Str., Taipei 11031, Taiwan

³ Department of Physical Medicine and Rehabilitation, School of Medicine, College of Medicine, Taipei Medical University, 250 Wuxing Str., Taipei 11031, Taiwan

⁴ Research Center of Artificial Intelligence in Medicine, Taipei Medical University, 250 Wuxing Str., Taipei 11031, Taiwan

* Authors to whom correspondence should be addressed.

Academic Editor: Antonio J. Salinas

Materials **2021**, *14*(15), 4224; <https://doi.org/10.3390/ma14154224>

Received: 28 June 2021 / Revised: 23 July 2021 / Accepted: 27 July 2021 / Published: 28 July 2021

(This article belongs to the Special Issue **Novel Hybrid Hydrogels for Bone Tissue Engineering Applications**)

Permissions

No special permission is required to reuse all or part of article published by MDPI, including figures and tables. For articles published under an open access Creative Common CC BY license, any part of the article may be reused without permission provided that the original article is clearly cited. Reuse of an article does not imply endorsement by the authors or MDPI.

Figure 2-3-a:

OpenStax College, Biology. October 17, 2013. **Provided by:** OpenStax CNX. **Located at:** <http://cnx.org/content/m44789/latest/?collection=col11448/latest>. **License:** [CC BY: Attribution](#)

Figure 2-3-b:

OpenStax. (2017). *Anatomy and Psychology*. [online textbook]. Retrieved from <https://cnx.org/contents/FPtK1z mh @8.81:kwbeYj9S @4/Bone-Structure>. **License:** [CC BY: Attribution](#)



Attribution 4.0 International (CC BY 4.0)

This is a human-readable summary of (and not a substitute for) the [license](#). [Disclaimer](#).

You are free to:

Share — copy and redistribute the material in any medium or format

Adapt — remix, transform, and build upon the material for any purpose, even commercially.

The licensor cannot revoke these freedoms as long as you follow the license terms.



Figure 2-4:

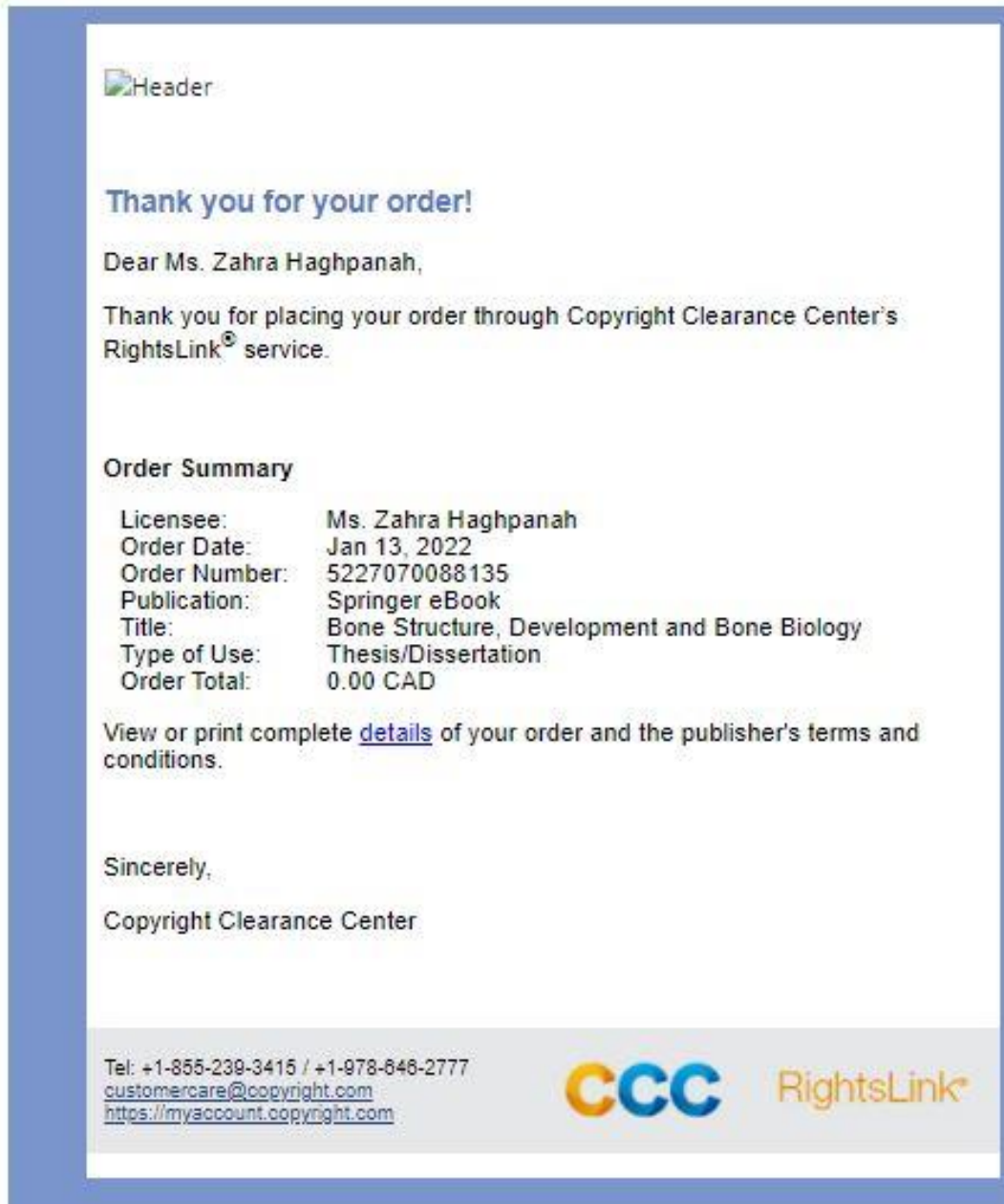


Figure 2-5: “Bone | Boundless Biology.” [Online]. Available: <https://courses.lumenlearning.com/boundless-biology/chapter/bone/>. [Accessed: 18-Mar-2021].

Summary [edit]

Description	English: Illustration from Anatomy & Physiology, Connexions Web site. http://cnx.org/content/col11496/1.6/ , Jun 19, 2013.
Date	3 April 2013, 01:34:09
Source	Anatomy & Physiology, Connexions Web site. http://cnx.org/content/col11496/1.6/ , Jun 19, 2013.
Author	OpenStax College
Other versions	 tamil

Licensing [edit]

This file is licensed under the [Creative Commons Attribution 3.0 Unported](https://creativecommons.org/licenses/by/4.0/) license.

 You are free:

- **to share** – to copy, distribute and transmit the work
- **to remix** – to adapt the work

Under the following conditions:

- **attribution** – You must give appropriate credit, provide a link to the license, and indicate if changes were made. You may do so in any reasonable manner, but not in any way that suggests the licensor endorses you or your use.

Figure 2-6 & Figure 2-7:

Osteoblast-Osteoclast Communication and Bone Homeostasis

[Jung-Min Kim](#),¹ [Chujiao Lin](#),¹ [Zheni Stavre](#),¹ [Matthew B. Greenblatt](#),² and [Jae-Hyuck Shim](#)^{1,3,*}

► [Author information](#) ► [Article notes](#) ▼ [Copyright and License information](#) [Disclaimer](#)

[Copyright](#) © 2020 by the authors.

Licensee MDPI, Basel, Switzerland. This article is an open access article distributed under the terms and conditions of the Creative Commons Attribution (CC BY) license (<http://creativecommons.org/licenses/by/4.0/>).

Permissions

No special permission is required to reuse all or part of article published by MDPI, including figures and tables. For articles published under an open access Creative Common CC BY license, any part of the article may be reused without permission provided that the original article is clearly cited. Reuse of an article does not imply endorsement by the authors or MDPI.

Figure 2-8:

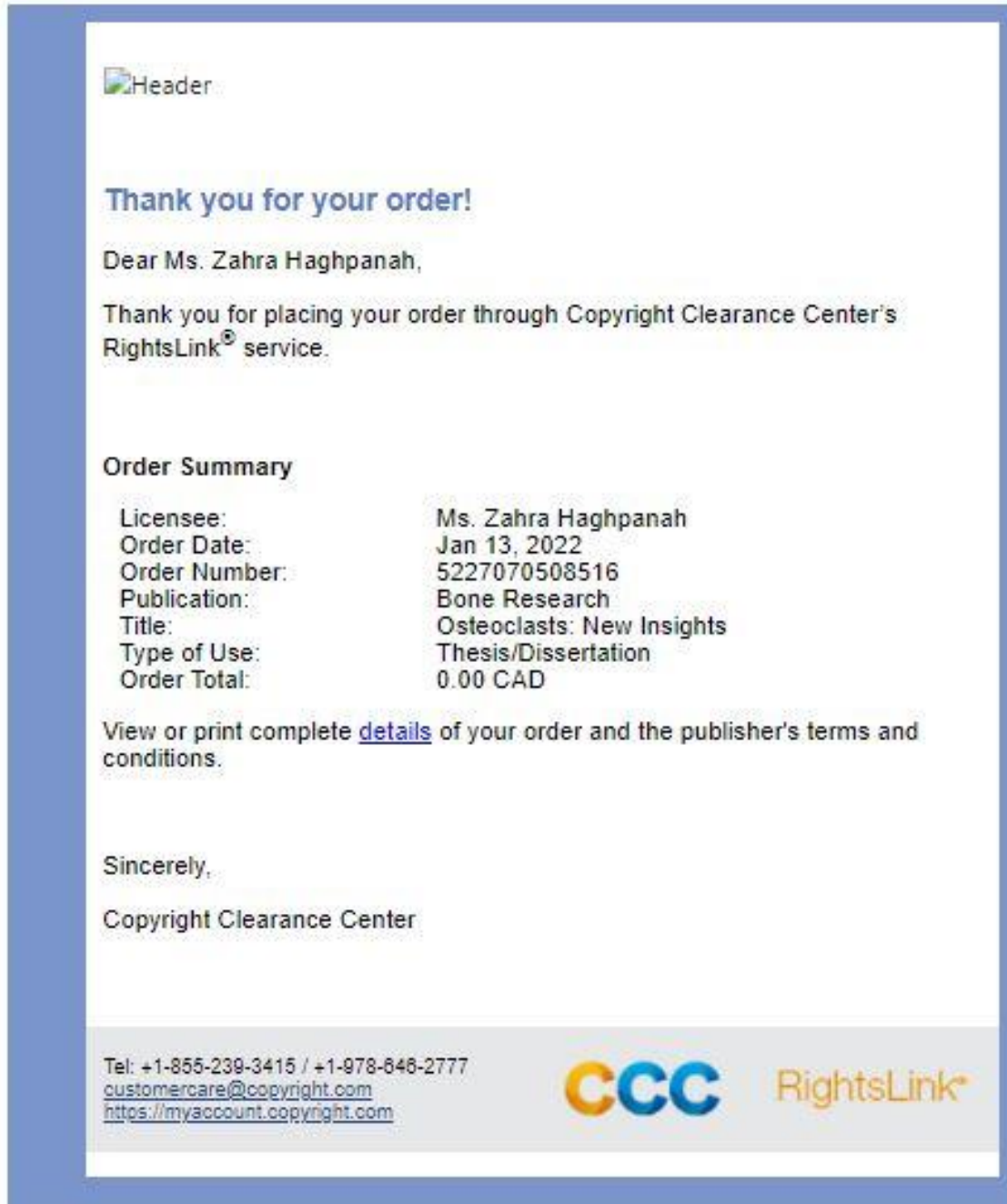
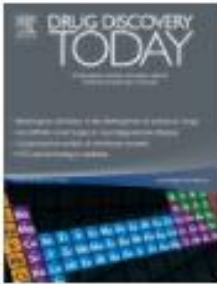


Figure 2-9:



Figure 2-10:



Thank you for your order!

Dear Ms. Zahra Haghpanah,

Thank you for placing your order through Copyright Clearance Center's RightsLink® service.

Order Summary

Licensee:	Ms. Zahra Haghpanah
Order Date:	Jan 13, 2022
Order Number:	5227070983858
Publication:	Drug Discovery Today
Title:	Angiogenesis and bone repair
Type of Use:	reuse in a thesis/dissertation
Order Total:	0.00 CAD

View or print complete [details](#) of your order and the publisher's terms and conditions.

Sincerely,

Copyright Clearance Center

Tel: +1-855-239-3415 / +1-978-646-2777
customercare@copyright.com
<https://myaccount.copyright.com>



Figure 2-11-a, b:

 Header

Thank you for your order!

Dear Ms. Zahra Haghpanah,

Thank you for placing your order through Copyright Clearance Center's RightsLink® service.

Order Summary

Licensee: Ms. Zahra Haghpanah
Order Date: Jan 13, 2022
Order Number: 5227071460937
Publication: European Journal of Orthopaedic Surgery & Traumatology
Title: Megaprosthesis reconstruction for periprosthetic or highly comminuted fractures of the hip and knee
Type of Use: Thesis/Dissertation
Order Total: 0.00 CAD

View or print complete [details](#) of your order and the publisher's terms and conditions.

Sincerely,

Copyright Clearance Center

Tel: +1-855-239-3415 / +1-978-646-2777
customercare@copyright.com
<https://myaccount.copyright.com>

Figure 2-11-c:

 Header

Thank you for your order!

Dear Ms. Zahra Haghpanah,

Thank you for placing your order through Copyright Clearance Center's RightsLink[®] service.

Order Summary

Licensee: Ms. Zahra Haghpanah
Order Date: Jan 13, 2022
Order Number: 5227080309733
Publication: International Orthopaedics
Title: Megaprotheses for the treatment of malignant bone tumours of the lower limbs
Type of Use: Thesis/Dissertation
Order Total: 0.00 CAD

View or print complete [details](#) of your order and the publisher's terms and conditions.

Sincerely,

Copyright Clearance Center

Tel: +1-855-239-3415 / +1-978-848-2777
customercare@copyright.com
<https://myaccount.copyright.com>

Figure 2-12:

 Header

Thank you for your order!

Dear Ms. Zahra Haghpanah,

Thank you for placing your order through Copyright Clearance Center's RightsLink[®] service.

Order Summary

Licensee: Ms. Zahra Haghpanah
Order Date: Jan 13, 2022
Order Number: 5227250173557
Publication: Journal of Materials Research
Title: Processing and properties of hydroxyapatite-based biomaterials for use as hard tissue replacement implants
Type of Use: Thesis/Dissertation
Order Total: 0.00 CAD

View or print complete [details](#) of your order and the publisher's terms and conditions.

Sincerely,

Copyright Clearance Center

Tel: +1-855-239-3415 / +1-978-646-2777
customercare@copyright.com
<https://myaccount.copyright.com>

Figure 2-13:

Photoinitiator Free Resins Composed of Plant-Derived Monomers for the Optical μ -3D Printing of Thermosets

[Migle Lebedevaite](#),¹ [Jolita Ostrauskaite](#),^{1,*} [Edvinas Skliutas](#),² and [Mangirdas Malinauskas](#)²

▶ [Author information](#) ▶ [Article notes](#) ▶ [Copyright and License information](#) ▶ [Disclaimer](#)

[Copyright](#) © 2019 by the authors.

Licensee MDPI, Basel, Switzerland. This article is an open access article distributed under the terms and conditions of the Creative Commons Attribution (CC BY) license (<http://creativecommons.org/licenses/by/4.0/>).

Permissions

No special permission is required to reuse all or part of article published by MDPI, including figures and tables. For articles published under an open access Creative Common CC BY license, any part of the article may be reused without permission provided that the original article is clearly cited. Reuse of an article does not imply endorsement by the authors or MDPI.

Figure 2-14:

Biobased Thermosets Prepared from Rigid Isosorbide and Flexible Soybean Oil Derivatives

Author: Wendi Liu, Tianshun Xie, Renhui Qiu

Publication: ACS Sustainable Chemistry & Engineering

Publisher: American Chemical Society

Date: Jan 1, 2017

Copyright © 2017, American Chemical Society



PERMISSION/LICENSE IS GRANTED FOR YOUR ORDER AT NO CHARGE

This type of permission/license, instead of the standard Terms and Conditions, is sent to you because no fee is being charged for your order. Please note the following:

- Permission is granted for your request in both print and electronic formats, and translations.
- If figures and/or tables were requested, they may be adapted or used in part.
- Please print this page for your records and send a copy of it to your publisher/graduate school.
- Appropriate credit for the requested material should be given as follows: "Reprinted (adapted) with permission from {COMPLETE REFERENCE CITATION}. Copyright {YEAR} American Chemical Society." Insert appropriate information in place of the capitalized words.
- One-time permission is granted only for the use specified in your RightsLink request. No additional uses are granted (such as derivative works or other editions). For any uses, please submit a new request.

If credit is given to another source for the material you requested from RightsLink, permission must be obtained from that source.

BACK

CLOSE WINDOW

Table 2-1, 2-2:



Thank you for your order!

Dear Ms. Zahra Haghanah,

Thank you for placing your order through Copyright Clearance Center's RightsLink[®] service.

Order Summary

Licensee:	Ms. Zahra Haghanah
Order Date:	Jan 13, 2022
Order Number:	5227030477340
Publication:	Composites Science and Technology
Title:	Development of nanocomposites for bone grafting
Type of Use:	reuse in a thesis/dissertation
Order Total:	0.00 CAD

View or print complete [details](#) of your order and the publisher's terms and conditions.

Sincerely,

Copyright Clearance Center

Tel: +1-855-239-3415 / +1-978-646-2777
customer@copyright.com
<https://myaccount.copyright.com>



References

- [1] E. Roddy, M. R. DeBaun, A. Daoud-Gray, Y. P. Yang, and M. J. Gardner, "Treatment of critical-sized bone defects: clinical and tissue engineering perspectives," *European Journal of Orthopaedic Surgery and Traumatology*, vol. 28, no. 3. Springer-Verlag France, pp. 351–362, 01-Apr-2018.
- [2] R. Yunus Basha, S. K. Sampath, and M. Doble, "Design of biocomposite materials for bone tissue regeneration," *Mater. Sci. Eng. C*, vol. 57, pp. 452–463, 2015.
- [3] J. C. Aurégan and T. Bégué, "Induced membrane for treatment of critical sized bone defect: A review of experimental and clinical experiences," *International Orthopaedics*, vol. 38, no. 9. Int Orthop, pp. 1971–1978, 2014.
- [4] E. H. Schemitsch, "Size Matters: Defining Critical in Bone Defect Size!," *J. Orthop. Trauma*, vol. 31, pp. S20–S22, Oct. 2017.
- [5] C. Heisel, S. Kinkel, L. Bernd, and V. Ewerbeck, "Megaprotheses for the treatment of malignant bone tumours of the lower limbs," *Int. Orthop.*, vol. 30, no. 6, pp. 452–457, 2006.
- [6] Z. Zhang *et al.*, "Cell-based resorption assays for bone graft substitutes," *Acta Biomater.*, vol. 8, no. 1, pp. 13–19, 2012.
- [7] M. Bohner, "Resorbable biomaterials as bone graft substitutes," *Materials Today*, vol. 13, no. 1–2. Elsevier, pp. 24–30, 01-Jan-2010.
- [8] T. Kurien, R. G. Pearson, and B. E. Scammell, "Bone graft substitutes currently available in orthopaedic practice: the evidence for their use," *Bone Joint J.*, vol. 95-B, no. 5, pp. 583–597, 2013.
- [9] R. Dimitriou, E. Jones, D. McGonagle, and P. V. Giannoudis, "Bone regeneration: Current concepts and future directions," *BMC Medicine*, vol. 9. BMC Med, 31-May-2011.
- [10] L. F. H. Theyse, M. A. Oosterlaken-Dijksterhuis, J. Van Doorn, W. J. A. Dhert, and H. A. W. Hazewinkel, "Growth hormone stimulates bone healing in a critical-sized bone defect model," *Clin. Orthop. Relat. Res.*, vol. 446, no. 446, pp. 259–267, 2006.
- [11] P. V. Giannoudis, H. Dinopoulos, and E. Tsiridis, "Bone substitutes: An update," *Injury*, vol. 36, no. 3, pp. S20–S27, 2005.
- [12] C. Laurencin, Y. Khan, and S. F. El-Amin, "Bone graft substitutes," *Expert Review of Medical Devices*, vol. 3, no. 1. pp. 49–57, Jan-2006.
- [13] M. E. Oest, K. M. Dupont, H. J. Kong, D. J. Mooney, and R. E. Guldberg, "Quantitative assessment of scaffold and growth factor-mediated repair of critically sized bone defects," *J. Orthop. Res.*, vol. 25, no. 7, pp. 941–950, Jul. 2007.
- [14] M. P. A. Bus *et al.*, "Intercalary allograft reconstructions following resection of primary bone tumors: A nationwide multicenter study," *J. Bone Jt. Surg. - Ser. A*, vol. 96, no. 4, Feb. 2014.

- [15] S. A. Lietman, W. W. Tomford, M. C. Gebhardt, D. S. Springfieldand, and H. J. Mankin, “Complications of irradiated allografts in orthopaedic tumor surgery,” *Clin. Orthop. Relat. Res.*, no. 375, pp. 214–217, 2000.
- [16] R. Agarwal and A. J. García, “Biomaterial strategies for engineering implants for enhanced osseointegration and bone repair,” *Adv. Drug Deliv. Rev.*, vol. 94, pp. 53–62, 2015.
- [17] G. Gosheger, C. Goetze, J. Harges, U. Joosten, W. Winkelmann, and C. von Eiff, “The Influence of the Alloy of Megaprotheses on Infection Rate,” *J. Arthroplasty*, vol. 23, no. 6, pp. 916–920, Sep. 2008.
- [18] H. Pilge, G. Gradl, R. von Eisenhart-Rothe, and H. Gollwitzer, “Incidence and outcome after infection of megaprotheses,” *HIP Int.*, vol. 22, no. SUPPL.8, Jul. 2012.
- [19] A. F. Mavrogenis, P. Ruggieri, M. Mercuri, and P. J. Papagelopoulos, “Megaprosthesis reconstruction for malignant bone tumors: Complications and outcomes,” *Journal of Long-Term Effects of Medical Implants*, vol. 18, no. 3. Begell House Inc., pp. 239–251, 2008.
- [20] H. Fritzsche, J. Goronzy, K. D. Schaser, C. Hofbauer, A. E. Postler, and K. P. Günther, “Complication profile and revision concepts for megaprosthesis reconstruction following tumour resection at the hip,” *Orthopade*, vol. 49, no. 2. Springer Medizin, pp. 123–132, 01-Feb-2020.
- [21] W. Contributors, “Medical gallery of Blausen Medical,” *WikiJournal of Medicine*, 2014. [Online]. Available: https://en.wikiversity.org/w/index.php?title=WikiJournal_of_Medicine/Medical_gallery_of_Blausen_Medical_2014&oldid=2187649. [Accessed: 18-Jan-2022].
- [22] “Bone grafting - Wikipedia.” [Online]. Available: https://en.wikipedia.org/wiki/Bone_grafting. [Accessed: 19-Mar-2021].
- [23] G. Gosheger, C. Goetze, J. Harges, U. Joosten, W. Winkelmann, and C. von Eiff, “The Influence of the Alloy of Megaprotheses on Infection Rate,” *J. Arthroplasty*, vol. 23, no. 6, pp. 916–920, Sep. 2008.
- [24] M. M. Stevens, “Biomaterials for bone tissue engineering,” *Mater. Today*, vol. 11, no. 5, pp. 18–25, 2008.
- [25] T. Kokubo and H. Takadama, “How useful is SBF in predicting in vivo bone bioactivity?,” *Biomaterials*, vol. 27, no. 15, pp. 2907–2915, May 2006.
- [26] M. Bohner, “Resorbable biomaterials as bone graft substitutes,” *Mater. Today*, vol. 13, no. 1–2, pp. 24–30, Jan. 2010.
- [27] N. C. Nguyen, W. J. Maloney, and R. H. Dauskardt, “Reliability of PMMA bone cement fixation: Fracture and fatigue crack-growth behaviour,” *J. Mater. Sci. Mater. Med.*, vol. 8, no. 8, pp. 473–483, Aug. 1997.

- [28] A. Bettencourt *et al.*, “Surface studies on acrylic bone cement,” *Int. J. Pharm.*, vol. 278, no. 1, pp. 181–186, Jun. 2004.
- [29] S. Lu, M. A. P. McGough, B. R. Rogers, J. C. Wenke, D. Shimko, and S. A. Guelcher, “Resorbable nanocomposites with bone-like strength and enhanced cellular activity,” *J. Mater. Chem. B*, vol. 5, no. 22, pp. 4198–4206, 2017.
- [30] M. Bohner, “Design of ceramic-based cements and putties for bone graft substitution,” *Eur. Cells Mater.*, vol. 20, pp. 1–12, Jul. 2010.
- [31] R. Murugan and S. Ramakrishna, “Development of nanocomposites for bone grafting,” *Compos. Sci. Technol.*, vol. 65, no. 15-16 SPEC. ISS., pp. 2385–2406, 2005.
- [32] M. Liu and Y. Lv, “Reconstructing bone with natural bone graft: A review of in vivo studies in bone defect animal model,” *Nanomaterials*, vol. 8, no. 12. MDPI AG, 01-Dec-2018.
- [33] S. Miar *et al.*, “Regeneration enhanced in critical-sized bone defects using bone-specific extracellular matrix protein,” *J. Biomed. Mater. Res. - Part B Appl. Biomater.*, 2020.
- [34] D. A. Puleo and A. Nanci, “Understanding and controlling the bone-implant interface,” *Biomaterials*, vol. 20, no. 23–24, pp. 2311–2321, 1999.
- [35] P. Zhou, F. He, B. Liu, and S. Wei, “Nerve electrical stimulation enhances osseointegration of implants in the beagle,” *Sci. Rep.*, vol. 9, no. 1, Dec. 2019.
- [36] A. F. Schilling, S. Filke, S. Brink, H. Korbmacher, M. Amling, and J. M. Rueger, “Osteoclasts and biomaterials,” *Eur. J. Trauma*, vol. 32, no. 2, pp. 107–113, 2006.
- [37] J. Kular, J. Tickner, S. M. Chim, and J. Xu, “An overview of the regulation of bone remodelling at the cellular level,” *Clinical Biochemistry*, vol. 45, no. 12. Elsevier, pp. 863–873, 01-Aug-2012.
- [38] A. J. Wagoner Johnson and B. A. Herschler, “A review of the mechanical behavior of CaP and CaP/polymer composites for applications in bone replacement and repair,” *Acta Biomaterialia*, vol. 7, no. 1. Elsevier, pp. 16–30, 01-Jan-2011.
- [39] K. Väänänen, “Mechanism of osteoclast mediated bone resorption - Rationale for the design of new therapeutics,” *Adv. Drug Deliv. Rev.*, vol. 57, no. 7, pp. 959–971, 2005.
- [40] C. Steffi, Z. Shi, C. H. Kong, and W. Wang, “Modulation of osteoclast interactions with orthopaedic biomaterials,” *J. Funct. Biomater.*, vol. 9, no. 1, 2018.
- [41] T. J. Martin and K. W. Ng, “Mechanisms by which cells of the osteoblast lineage control osteoclast formation and activity,” *J. Cell. Biochem.*, vol. 56, pp. 357–366, 1994.
- [42] W. J. Boyle, W. S. Simonet, and D. L. Lacey, “Osteoclast differentiation and activation,” vol. 423, no. May, pp. 337–342, 2003.
- [43] S. Viguier-Carrin, P. Garnero, and P. D. Delmas, “The role of collagen in bone strength,” *Osteoporos. Int.*, vol. 17, no. 3, pp. 319–336, Mar. 2006.

- [44] R. James, M. Deng, C. T. Laurencin, and S. G. Kumbar, "Nanocomposites and bone regeneration," *Front. Mater. Sci.*, vol. 5, no. 4, pp. 342–357, 2011.
- [45] A. R. Costa-Pinto, R. L. Reis, and N. M. Neves, "Scaffolds based bone tissue engineering: The role of chitosan," *Tissue Eng. - Part B Rev.*, vol. 17, no. 5, pp. 331–347, 2011.
- [46] G. A. Rodan, "Introduction to bone biology," *Bone*, vol. 13, pp. S3–S6, 1992.
- [47] J. Y. Rho, L. Kuhn-Spearing, and P. Zioupos, "Mechanical properties and the hierarchical structure of bone," *Med. Eng. Phys.*, vol. 20, no. 2, pp. 92–102, Mar. 1998.
- [48] C. Y. Lin and J. H. Kang, "Mechanical Properties of Compact Bone Defined by the Stress-Strain Curve Measured Using Uniaxial Tensile Test: A Concise Review and Practical Guide," *Mater. (Basel, Switzerland)*, vol. 14, no. 15, Aug. 2021.
- [49] A. Hasan *et al.*, "Advances in osteobiologic materials for bone substitutes," *J. Tissue Eng. Regen. Med.*, vol. 12, no. 6, pp. 1448–1468, 2018.
- [50] S. C. Cowin, *Bone Mechanics Handbook*. CRC Press, 2001.
- [51] "Bone | Boundless Biology." [Online]. Available: <https://courses.lumenlearning.com/boundless-biology/chapter/bone/>. [Accessed: 18-Mar-2021].
- [52] "Spongy Bone (Cancellous Bone) - Definition & Function | Biology." [Online]. Available: <https://biologydictionary.net/spongy-bone/>. [Accessed: 19-Mar-2021].
- [53] F. F. Safadi *et al.*, "Bone structure, development and bone biology," in *Bone Pathology*, Humana Press, 2009, pp. 1–50.
- [54] A. M. F. S. Mohamed, "An Overview of Bone Cells and their Regulating Factors of Differentiation," *Malays. J. Med. Sci.*, vol. 15, no. 1, p. 4, 2008.
- [55] M. Capulli, R. Paone, and N. Rucci, "Osteoblast and osteocyte: Games without frontiers," *Archives of Biochemistry and Biophysics*, vol. 561. Academic Press Inc., pp. 3–12, 01-Nov-2014.
- [56] M. Owen, "Marrow stromal stem cells," *J. Cell Sci.*, vol. 10, no. SSUPL. 10, pp. 63–76, 1988.
- [57] F. Granero-Moltó *et al.*, "Regenerative Effects of Transplanted Mesenchymal Stem Cells in Fracture Healing," *Stem Cells*, vol. 27, no. 8, pp. 1887–1898, Aug. 2009.
- [58] R. Florencio-Silva, G. R. D. S. Sasso, E. Sasso-Cerri, M. J. Simões, and P. S. Cerri, "Biology of Bone Tissue: Structure, Function, and Factors That Influence Bone Cells," *BioMed Research International*, vol. 2015. Hindawi Publishing Corporation, 2015.
- [59] A. Infante and C. I. Rodríguez, "Osteogenesis and aging: lessons from mesenchymal stem cells," *Stem cell research & therapy*, vol. 9, no. 1. NLM (Medline), p. 244, 26-Sep-2018.
- [60] J. M. Kim, C. Lin, Z. Stavre, M. B. Greenblatt, and J. H. Shim, "Osteoblast-Osteoclast Communication and Bone Homeostasis," *Cells*, vol. 9, no. 9. NLM (Medline), 10-Sep-2020.
- [61] M. Fakhry, "Molecular mechanisms of mesenchymal stem cell differentiation towards osteoblasts,"

- World J. Stem Cells*, vol. 5, no. 4, p. 136, 2013.
- [62] L. F. Bonewald, “The amazing osteocyte,” *J. Bone Miner. Res.*, vol. 26, no. 2, pp. 229–238, Feb. 2011.
- [63] M. Manfrini *et al.*, “Mesenchymal stem cells from patients to assay bone graft substitutes,” *J. Cell. Physiol.*, vol. 228, no. 6, pp. 1229–1237, Jun. 2013.
- [64] “Human primary cells versus cell lines: differences and advantages| PromoCell.” [Online]. Available: <https://www.promocell.com/in-the-lab/human-primary-cells-and-immortal-cell-lines/>. [Accessed: 18-Mar-2021].
- [65] P. W. Hwang and J. A. Horton, “Variable osteogenic performance of MC3T3-E1 subclones impacts their utility as models of osteoblast biology,” *Sci. Rep.*, vol. 9, no. 1, Dec. 2019.
- [66] J.-M. Lee *et al.*, “The effect of biomechanical stimulation on osteoblast differentiation of human jaw periosteum-derived stem cells,” *Maxillofac. Plast. Reconstr. Surg.*, vol. 39, no. 1, Dec. 2017.
- [67] J. B. Lian and G. S. Stein, “Osteoblast Biology,” in *Osteoporosis, Two-Volume Set*, Elsevier Inc., 2008, pp. 93–150.
- [68] S. R. Goldberg, J. Georgiou, M. Glogauer, and M. D. Grynepas, “A 3D scanning confocal imaging method measures pit volume and captures the role of Rac in osteoclast function,” *Bone*, vol. 51, no. 1, pp. 145–152, 2012.
- [69] G. D. ROODMAN, “Advances in Bone Biology: The Osteoclast*,” *Endocr. Rev.*, vol. 17, no. 4, pp. 308–332, Aug. 1996.
- [70] K. Tiedemann, D. Le Nihouannen, J. E. Fong, O. Hussein, J. E. Barralet, and S. V. Komarova, “Regulation of osteoclast growth and fusion by mTOR/raptor and mTOR/riCTOR/Akt,” *Front. Cell Dev. Biol.*, vol. 5, no. MAY, p. 54, May 2017.
- [71] N. S. Soysa, N. Alles, K. Aoki, and K. Ohya, “Osteoclast formation and differentiation: An overview,” *J. Med. Dent. Sci.*, vol. 59, no. 3, pp. 65–74, 2012.
- [72] B. F. Boyce, D. E. Hughes, K. R. Wright, L. Xing, and A. Dai, “Recent advances in bone biology provide insight into the pathogenesis of bone diseases,” *Laboratory Investigation*, vol. 79, no. 2, pp. 83–94, 01-Feb-1999.
- [73] M. P. Yavropoulou and J. G. Yovos, “Osteoclastogenesis - Current knowledge and future perspectives,” *J. Musculoskelet. Neuronal Interact.*, vol. 8, no. 3, pp. 204–216, 2008.
- [74] J. Kikuta and M. Ishii, “Osteoclast migration, differentiation and function: Novel therapeutic targets for rheumatic diseases,” *Rheumatol. (United Kingdom)*, vol. 52, no. 2, pp. 226–234, Feb. 2013.
- [75] Q. T. Phan *et al.*, “Cxcl9 and Cxcr3.2 regulate recruitment of osteoclast progenitors to bone matrix in a medaka osteoporosis model,” *Proc. Natl. Acad. Sci. U. S. A.*, vol. 117, no. 32, pp. 19276–19286, Aug. 2020.

- [76] A. H. Lutter *et al.*, “A novel resorption assay for osteoclast functionality based on an osteoblast-derived native extracellular matrix,” *J. Cell. Biochem.*, vol. 109, no. 5, pp. 1025–1032, Apr. 2010.
- [77] F. Xu and S. L. Teitelbaum, “Osteoclasts: New Insights,” *Bone Research*, vol. 1, no. 1. Sichuan University, pp. 11–26, 29-Mar-2013.
- [78] K. Henriksen *et al.*, “Degradation of the Organic Phase of Bone by Osteoclasts: A Secondary Role for Lysosomal Acidification,” *J. Bone Miner. Res.*, vol. 21, no. 1, pp. 58–66, Sep. 2005.
- [79] S. Marino, J. G. Logan, D. Mellis, and M. Capulli, “Generation and culture of osteoclasts,” *Bonekey Rep.*, vol. 3, no. July, pp. 1–9, 2014.
- [80] P. Collin-Osdoby and P. Osdoby, “RANKL-mediated osteoclast formation from murine RAW 264.7 cells,” *Methods Mol. Biol.*, vol. 816, pp. 187–202, 2012.
- [81] C. Song *et al.*, “Evaluation of efficacy on RANKL induced osteoclast from RAW264.7 cells,” *J. Cell. Physiol.*, vol. 234, no. 7, pp. 11969–11975, 2019.
- [82] R. Owen and G. C. Reilly, “In vitro models of bone remodelling and associated disorders,” *Front. Bioeng. Biotechnol.*, vol. 6, no. OCT, pp. 1–22, 2018.
- [83] K. Fuller, J. T. L. Thong, B. C. Breton, and T. J. Chambers, “Automated three-dimensional characterization of osteoclastic resorption lacunae by stereoscopic scanning electron microscopy,” *J. Bone Miner. Res.*, vol. 9, no. 1, pp. 17–23, 1994.
- [84] T. Suda, E. Jimi, I. Nakamura, and N. Takahashi, “Role of 1 alpha,25-dihydroxyvitamin D3 in osteoclast differentiation and function,” *Methods Enzymol.*, vol. 282, pp. 223–235, 1997.
- [85] L. You *et al.*, “Osteocytes as mechanosensors in the inhibition of bone resorption due to mechanical loading,” *Bone*, vol. 42, no. 1, pp. 172–179, Jan. 2008.
- [86] N. S. Soysa, N. Alles, K. Aoki, and K. Ohya, “Three-dimensional characterization of osteoclast bone-resorbing activity in the resorption lacunae,” 2009.
- [87] T. Hassenkam, H. L. Jørgensen, and J. B. Lauritzen, “Mapping the imprint of bone remodeling by atomic force microscopy,” *Anat. Rec. - Part A Discov. Mol. Cell. Evol. Biol.*, vol. 288, no. 10, pp. 1087–1094, Oct. 2006.
- [88] L. Bozec *et al.*, “Atomic force microscopy of collagen structure in bone and dentine revealed by osteoclastic resorption,” *Ultramicroscopy*, vol. 105, no. 1–4, pp. 79–89, Nov. 2005.
- [89] G. Grimandi *et al.*, “Quantitative and reliable in vitro method combining scanning electron microscopy and image analysis for the screening of osteotropic modulators,” *Microsc. Res. Tech.*, vol. 69, no. 8, pp. 606–612, Aug. 2006.
- [90] J. Vanderroost, “From histology to micro-CT: Measuring and modeling resorption cavities and their relation to bone competence,” *World J. Radiol.*, vol. 6, no. 9, p. 643, 2014.
- [91] R. J. Friederichs, R. A. Brooks, M. Ueda, and S. M. Best, “In vitro osteoclast formation and

- resorption of silicon-substituted hydroxyapatite ceramics,” *J. Biomed. Mater. Res. - Part A*, vol. 103, no. 10, pp. 3312–3322, Oct. 2015.
- [92] R. Zhang *et al.*, “Bone Resorption by Osteoclasts,” vol. 289, no. September, pp. 1504–1509, 2000.
- [93] T. Hefti, M. Frischherz, N. D. Spencer, H. Hall, and F. Schlottig, “A comparison of osteoclast resorption pits on bone with titanium and zirconia surfaces,” *Biomaterials*, vol. 31, no. 28, pp. 7321–7331, Oct. 2010.
- [94] T. R. Arnett and D. W. Dempster, “A comparative study of disaggregated chick and rat osteoclasts in vitro: effects of calcitonin and prostaglandins,” *Endocrinology*, vol. 120, no. 2, pp. 602–608, 1987.
- [95] R. J. Murrills and D. W. Dempster, “The effects of stimulators of intracellular cyclic AMP on rat and chick osteoclasts in vitro: validation of a simplified light microscope assay of bone resorption,” *Bone*, vol. 11, no. 5, pp. 333–344, 1990.
- [96] A. J. Fenton *et al.*, “A carboxyl-terminal peptide from the parathyroid hormone-related protein inhibits bone resorption by osteoclasts,” *Endocrinology*, vol. 129, no. 4, pp. 1762–1768, 1991.
- [97] A. Okuda, L. M. Taylor, and J. N. M. Heersche, “Prostaglandin E2 initially inhibits and then stimulates bone resorption in isolated rabbit osteoclast cultures,” *Bone Miner.*, vol. 7, no. 3, pp. 255–266, 1989.
- [98] T. R. Arnett and D. W. Dempster, “Effect of pH on bone resorption by rat osteoclasts in vitro,” *Endocrinology*, vol. 119, no. 1, pp. 119–124, 1986.
- [99] B. R. Rifkin, A. T. Vernillo, A. P. Kleckner, J. M. Auszmann, L. R. Rosenberg, and M. Zimmerman, “Cathepsin B and L activities in isolated osteoclasts,” *Biochem. Biophys. Res. Commun.*, vol. 179, no. 1, pp. 63–69, Aug. 1991.
- [100] J. M. Delaisse *et al.*, “The effects of inhibitors of cysteine-proteinases and collagenase on the resorptive activity of isolated osteoclasts,” *Bone*, vol. 8, no. 5, pp. 305–313, 1987.
- [101] M. L. Taylor, E. Maconnachie, K. Frank, A. Boyde, and S. J. Jones, “The effect of fluoride on the resorption of dentine by osteoclasts in vitro,” *J. Bone Miner. Res.*, vol. 5 Suppl 1, no. 1 S, pp. S121–S130, 1990.
- [102] S. J. Jones *et al.*, “Variation in the Sizes of Resorption Lacunae made in Vitro,” *Scan. Electron Microsc.*, vol. 33, no. 4, p. 33, 1986.
- [103] J. M. Delaisse *et al.*, “The effects of inhibitors of cysteine-proteinases and collagenase on the resorptive activity of isolated osteoclasts,” *Bone*, vol. 8, no. 5, pp. 305–313, Jan. 1987.
- [104] Y. Yamada, A. Ito, M. Sakane, S. Miyakawa, and T. Uemura, “Laser microscopic measurement of osteoclastic resorption pits on biomaterials,” *Mater. Sci. Eng. C*, vol. 27, no. 4, pp. 762–766, May 2007.

- [105] J. E. Dumas, K. Zienkiewicz, S. A. Tanner, E. M. Prieto, S. Bhattacharyya, and S. A. Guelcher, "Synthesis and characterization of an injectable allograft bone/polymer composite bone void filler with tunable mechanical properties," *Tissue Eng. Part A*, vol. 16, no. 8, pp. 2505–2518, Aug. 2010.
- [106] "An Introduction to Nutrition v. 1.0."
- [107] "Bone Structure and Function." [Online]. Available: <https://2012books.lardbucket.org/books/an-introduction-to-nutrition/s13-01-bone-structure-and-function.html>. [Accessed: 18-Mar-2021].
- [108] K. Kapinas and A. M. Delany, "MicroRNA biogenesis and regulation of bone remodeling," *Arthritis Research and Therapy*, vol. 13, no. 3. BioMed Central, p. 220, 27-May-2011.
- [109] E. F. Eriksen, "Cellular mechanisms of bone remodeling," *Reviews in Endocrine and Metabolic Disorders*, vol. 11, no. 4. Rev Endocr Metab Disord, pp. 219–227, Dec-2010.
- [110] T. Negishi-Koga and H. Takayanagi, "Bone cell communication factors and Semaphorins," *Bonekey Rep.*, vol. 1, p. 183, Sep. 2012.
- [111] C. Zhao *et al.*, "Bidirectional ephrinB2-EphB4 signaling controls bone homeostasis," *Cell Metab.*, vol. 4, no. 2, pp. 111–121, Aug. 2006.
- [112] U. H. Lerner, E. Kindstedt, and P. Lundberg, "The critical interplay between bone resorbing and bone forming cells," *J. Clin. Periodontol.*, vol. 46, no. S21, pp. 33–51, Jun. 2019.
- [113] B. Langdahl, S. Ferrari, and D. W. Dempster, "Bone modeling and remodeling: potential as therapeutic targets for the treatment of osteoporosis," *Therapeutic Advances in Musculoskeletal Disease*, vol. 8, no. 6. SAGE Publications Ltd, pp. 225–235, 01-Dec-2016.
- [114] N. M. Iñiguez-Ariza and B. L. Clarke, "Bone biology, signaling pathways, and therapeutic targets for osteoporosis," *Maturitas*, vol. 82, no. 2. Elsevier Ireland Ltd, pp. 245–255, 01-Oct-2015.
- [115] X. Feng and J. M. McDonald, "Disorders of bone remodeling," *Annu. Rev. Pathol. Mech. Dis.*, vol. 6, pp. 121–145, Feb. 2011.
- [116] M. D. DeLacure, "Physiology of bone healing and bone grafts," *Otolaryngol. Clin. North Am.*, vol. 27, no. 5, pp. 859–874, Oct. 1994.
- [117] J. J. Sela and I. A. Bab, "Healing of bone fracture: General concepts," in *Principles of Bone Regeneration*, Springer US, 2012, pp. 1–8.
- [118] K. M. Alghazali, Z. A. Nima, R. N. Hamzah, M. S. Dhar, D. E. Anderson, and A. S. Biris, "Bone-tissue engineering: Complex tunable structural and biological responses to injury, drug delivery, and cell-based therapies," *Drug Metabolism Reviews*, vol. 47, no. 4. Taylor and Francis Ltd, pp. 431–454, 02-Oct-2015.
- [119] C. S. Bahney *et al.*, "Cellular biology of fracture healing," *Journal of Orthopaedic Research*, vol. 37, no. 1. John Wiley and Sons Inc., pp. 35–50, 01-Jan-2019.
- [120] R. A. D. Carano and E. H. Filvaroff, "Angiogenesis and bone repair," *Drug Discovery Today*, vol.

- 8, no. 21. *Drug Discov Today*, pp. 980–989, 01-Nov-2003.
- [121] A. Schindeler, M. M. McDonald, P. Bokko, and D. G. Little, “Bone remodeling during fracture repair: The cellular picture,” *Seminars in Cell and Developmental Biology*, vol. 19, no. 5. Elsevier Ltd, pp. 459–466, 2008.
- [122] Y. Khan and C. T. Laurencin, “Fracture Repair with Ultrasound: Clinical and Cell-Based Evaluation,” *J. Bone Jt. Surgery-American Vol.*, vol. 90, no. Suppl 1, pp. 138–144, Feb. 2008.
- [123] P. P. Spicer, J. D. Kretlow, S. Young, J. A. Jansen, F. K. Kasper, and A. G. Mikos, “Evaluation of bone regeneration using the rat critical size calvarial defect,” *Nat. Protoc.*, vol. 7, no. 10, pp. 1918–1929, Sep. 2012.
- [124] Z. Gugala, R. W. Lindsey, and S. Gogolewski, “New Approaches in the Treatment of Critical-Size Segmental Defects in Long Bones,” *Macromol. Symp.*, vol. 253, no. 1, pp. 147–161, Aug. 2007.
- [125] J. C. Reichert *et al.*, “The challenge of establishing preclinical models for segmental bone defect research,” *Biomaterials*, vol. 30, no. 12, pp. 2149–2163, Apr. 2009.
- [126] G. M. Calori, E. Mazza, M. Colombo, and C. Ripamonti, “The use of bone-graft substitutes in large bone defects: Any specific needs?,” *Injury*, vol. 42, no. SUPPL. 2, pp. S56–S63, 2011.
- [127] J. A. Goulet, L. E. Senunas, G. L. DeSilva, and M. L. V. H. Greenfield, “Autogenous iliac crest bone graft: Complications and functional assessment,” in *Clinical Orthopaedics and Related Research*, 1997, no. 339, pp. 76–81.
- [128] A. Noshchenko, L. Hoffecker, E. M. Lindley, E. L. Burger, C. M. J. Cain, and V. V. Patel, “Perioperative and long-term clinical outcomes for bone morphogenetic protein versus iliac crest bone graft for lumbar fusion in degenerative disk disease: Systematic review with meta-analysis,” *Journal of Spinal Disorders and Techniques*, vol. 27, no. 3. Lippincott Williams and Wilkins, pp. 117–135, 2014.
- [129] L. Vidal, C. Kamplaitner, M. Brennan, A. Hoornaert, and P. Layrolle, “Reconstruction of Large Skeletal Defects: Current Clinical Therapeutic Strategies and Future Directions Using 3D Printing,” *Frontiers in Bioengineering and Biotechnology*, vol. 8. Frontiers Media S.A., p. 61, 12-Feb-2020.
- [130] B. B. Hudson Berrey, C. Frederick Lord, M. C. Gebhardt, and H. J. Mankin, “Fractures of Allografts,” vol. 72, no. 6, 1990.
- [131] B. H. Berrey, C. F. Lord, M. C. Gebhardt, and H. J. Mankin, “Fractures of allografts. Frequency, treatment, and end-results,” *J. Bone Jt. Surg. - Ser. A*, vol. 72, no. 6, pp. 825–833, Jul. 1990.
- [132] H. Hattori, J. Mibe, and K. Yamamoto, “Modular megaprosthesis in metastatic bone disease of the femur,” *Orthopedics*, vol. 34, no. 12, Dec. 2011.
- [133] E. Pala, G. Trovarelli, A. Angelini, M. Maraldi, A. Berizzi, and P. Ruggieri, “Megaprosthesis of the knee in tumor and revision surgery,” *Acta Biomed.*, vol. 88, no. Suppl 2, pp. 129–138, 2017.

- [134] A. Kawai, J. H. Healey, P. J. Boland, E. A. Athanasian, and D. G. Jeon, "A rotating-hinge knee replacement for malignant tumors of the femur and tibia," *J. Arthroplasty*, vol. 14, no. 2, pp. 187–196, 1999.
- [135] C. H. Gerrand, D. Currie, P. Grigoris, R. Reid, and D. L. Hamblen, "Prosthetic reconstruction of the femur for primary bone sarcoma," *Int. Orthop.*, vol. 23, no. 5, pp. 286–290, 1999.
- [136] R. Capanna, H. G. Morris, D. Campanacci, M. Del Ben, and M. Campanacci, "Modular uncemented prosthetic reconstruction after resection of tumours of the distal femur," *J. Bone Jt. Surg. - Ser. B*, vol. 76, no. 2, pp. 178–186, Mar. 1994.
- [137] F. Lundh, A. S. Sayed-Noor, O. Brosjö, and H. Bauer, "Megaprosthetic reconstruction for periprosthetic or highly comminuted fractures of the hip and knee," *Eur. J. Orthop. Surg. Traumatol.*, vol. 24, no. 4, pp. 553–557, 2014.
- [138] S. N. Khan, F. P. Cammisa, H. S. Sandhu, A. D. Diwan, F. P. Girardi, and J. M. Lane, "The biology of bone grafting.," *J. Am. Acad. Orthop. Surg.*, vol. 13, no. 1, pp. 77–86, 2005.
- [139] T. Albrektsson and C. Johansson, "Osteoinduction, osteoconduction and osseointegration," *Eur. Spine J.*, vol. 10, no. 2, pp. S96–S101, 2001.
- [140] S. Bose, M. Roy, and A. Bandyopadhyay, "Recent advances in bone tissue engineering scaffolds," *Trends in Biotechnology*, vol. 30, no. 10. Elsevier Current Trends, pp. 546–554, 01-Oct-2012.
- [141] C. C. Berry, G. Campbell, A. Spadiccino, M. Robertson, and A. S. G. Curtis, "The influence of microscale topography on fibroblast attachment and motility," *Biomaterials*, vol. 25, no. 26, pp. 5781–5788, Nov. 2004.
- [142] G. Turnbull *et al.*, "3D bioactive composite scaffolds for bone tissue engineering," *Bioact. Mater.*, vol. 3, no. 3, pp. 278–314, 2018.
- [143] V. Karageorgiou and D. Kaplan, "Porosity of 3D biomaterial scaffolds and osteogenesis," *Biomaterials*, vol. 26, no. 27. Elsevier BV, pp. 5474–5491, 2005.
- [144] S. F. Hulbert, F. A. Young, R. S. Mathews, J. J. Klawitter, C. D. Talbert, and F. H. Stelling, "Potential of ceramic materials as permanently implantable skeletal prostheses," *J. Biomed. Mater. Res.*, vol. 4, no. 3, pp. 433–456, 1970.
- [145] A. J. Harmata, S. Uppuganti, M. Granke, S. A. Guelcher, and J. S. Nyman, "Compressive fatigue and fracture toughness behavior of injectable, settable bone cements," *J. Mech. Behav. Biomed. Mater.*, vol. 51, pp. 345–355, Nov. 2015.
- [146] J. R. Vinson and R. L. Sierakowski, "Introduction To Composite Materials," pp. 1–27, 1987.
- [147] C. T. Laurencin, M. A. Attawia, H. E. Elgendy, and K. M. Herbert, "Tissue engineered bone-regeneration using degradable polymers: The formation of mineralized matrices," in *Bone*, 1996, vol. 19, no. 1 SUPPL., pp. S93–S99.

- [148] J. Du *et al.*, “Effect of hydroxyapatite fillers on the mechanical properties and osteogenesis capacity of bio-based polyurethane composite scaffolds,” *J. Mech. Behav. Biomed. Mater.*, vol. 88, pp. 150–159, Dec. 2018.
- [149] J. Z. Paxton, K. Donnelly, R. P. Keatch, and K. Baar, “Engineering the bone-ligament interface using polyethylene glycol diacrylate incorporated with hydroxyapatite,” *Tissue Eng. - Part A*, vol. 15, no. 6, pp. 1201–1209, 2009.
- [150] W. Suchanek and M. Yoshimura, “Processing and properties of hydroxyapatite-based biomaterials for use as hard tissue replacement implants,” *J. Mater. Res.*, vol. 13, no. 1, pp. 94–117, 1998.
- [151] A. R. Costa-Pinto, A. L. Lemos, F. K. Tavaría, and M. Pintado, “Chitosan and Hydroxyapatite Based Biomaterials to Circumvent Periprosthetic Joint Infections,” *Mater. (Basel, Switzerland)*, vol. 14, no. 4, pp. 1–20, Feb. 2021.
- [152] E. M. Rivera-Muñoz, “Hydroxyapatite-Based Materials: Synthesis and Characterization,” *Biomed. Eng. - Front. Challenges*, Aug. 2011.
- [153] W. F. Neuman and M. W. Neuman, “The chemical dynamics of bone mineral.,” *Chem. Dyn. bone Miner.*, 1958.
- [154] M. Akram, R. Ahmed, I. Shakir, W. A. W. Ibrahim, and R. Hussain, “Extracting hydroxyapatite and its precursors from natural resources,” *J. Mater. Sci. 2013 494*, vol. 49, no. 4, pp. 1461–1475, Nov. 2013.
- [155] C. Li, W. Qin, S. Lakshmanan, X. Ma, X. Sun, and B. Xu, “Hydroxyapatite based biocomposite scaffold: A highly biocompatible material for bone regeneration,” *Saudi J. Biol. Sci.*, vol. 27, no. 8, pp. 2143–2148, Aug. 2020.
- [156] J. Lu, H. Yu, and C. Chen, “Biological properties of calcium phosphate biomaterials for bone repair: a review,” *RSC Adv.*, vol. 8, no. 4, pp. 2015–2033, Jan. 2018.
- [157] M. Hallman, L. Sennerby, L. Zetterqvist, and S. Lundgren, “A 3-year prospective follow-up study of implant-supported fixed prostheses in patients subjected to maxillary sinus floor augmentation with a 80:20 mixture of deproteinized bovine bone and autogenous bone Clinical, radiographic and resonance frequency analysis,” *Int. J. Oral Maxillofac. Surg.*, vol. 34, no. 3, pp. 273–280, May 2005.
- [158] E. Rumpel *et al.*, “The biodegradation of hydroxyapatite bone graft substitutes in vivo,” *Folia Morphol. (Warsz.)*, vol. 65, no. 1, pp. 43–48, 2006.
- [159] M. Vallecillo Capilla, M. de N. Romero Olid, M. V. Olmedo Gaya, C. Reyes Botella, and C. Zorrilla Romera, “Cylindrical dental implants with hydroxyapatite- and titanium plasma spray-coated surfaces: 5-year results.,” *J. Oral Implantol.*, vol. 33, no. 2, pp. 59–68, Jan. 2007.
- [160] W. Zhou, Z. Liu, S. Xu, P. Hao, F. Xu, and A. Sun, “Long-term survivability of hydroxyapatite-coated implants: a meta-analysis,” *Oral Surg.*, vol. 4, no. 1, pp. 2–7, Feb. 2011.

- [161] J. Jeong, J. H. Kim, J. H. Shim, N. S. Hwang, and C. Y. Heo, "Bioactive calcium phosphate materials and applications in bone regeneration," *Biomater. Res. 2019 231*, vol. 23, no. 1, pp. 1–11, Jan. 2019.
- [162] L. Calderín, M. J. Stott, and A. Rubio, "Electronic and crystallographic structure of apatites," *Phys. Rev. B*, vol. 67, no. 13, p. 134106, Apr. 2003.
- [163] A. Dey, A. K. Mukhopadhyay, S. Gangadharan, M. K. Sinha, and D. Basu, "Characterization of Microplasma Sprayed Hydroxyapatite Coating," *J. Therm. Spray Technol. 2009 184*, vol. 18, no. 4, pp. 578–592, Sep. 2009.
- [164] P. A. Ramires, A. Wennerberg, C. B. Johansson, F. Cosentino, S. Tundo, and E. Milella, "Biological behavior of sol-gel coated dental implants," *J. Mater. Sci. Mater. Med.*, vol. 14, no. 6, pp. 539–545, Jun. 2003.
- [165] G. L. Darimont, R. Cloots, E. Heinen, L. Seidel, and R. Legrand, "In vivo behaviour of hydroxyapatite coatings on titanium implants: a quantitative study in the rabbit," *Biomaterials*, vol. 23, no. 12, pp. 2569–2575, 2002.
- [166] T. Albrektsson, "Hydroxyapatite-coated implants: a case against their use," *J. Oral Maxillofac. Surg.*, vol. 56, no. 11, pp. 1312–1326, 1998.
- [167] A. Göransson *et al.*, "An in vitro comparison of possibly bioactive titanium implant surfaces," *J. Biomed. Mater. Res. A*, vol. 88, no. 4, pp. 1037–1047, Mar. 2009.
- [168] P. T. De Oliveira, S. F. Zalzal, M. M. Beloti, A. L. Rosa, and A. Nanci, "Enhancement of in vitro osteogenesis on titanium by chemically produced nanotopography," *J. Biomed. Mater. Res. A*, vol. 80, no. 3, pp. 554–564, Mar. 2007.
- [169] R. Yoshimoto, M. Murata, T. Akazawa, and M. Arisue, "Effects of Functionally Graded Hydroxyapatite for Large Mandibular Defects in Adult Rabbits," *J. Hard Tissue Biol.*, vol. 19, no. 1, pp. 33–42, 2010.
- [170] T. J. Webster, C. Ergun, R. H. Doremus, R. W. Siegel, and R. Bizios, "Enhanced functions of osteoblasts on nanophase ceramics," *Biomaterials*, vol. 21, no. 17, pp. 1803–1810, Sep. 2000.
- [171] T. Kitsugi, T. Yamamuro, T. Nakamura, S. Kotani, T. Kokubo, and H. Takeuchi, "Four calcium phosphate ceramics as bone substitutes for non-weight-bearing," *Biomaterials*, vol. 14, no. 3, pp. 216–224, 1993.
- [172] T. J. Webster, R. W. Siegel, and R. Bizios, "Osteoblast adhesion on nanophase ceramics," *Biomaterials*, vol. 20, no. 13, pp. 1221–1227, Jul. 1999.
- [173] J. Huang *et al.*, "Development of nano-sized hydroxyapatite reinforced composites for tissue engineering scaffolds," in *Journal of Materials Science: Materials in Medicine*, 2007, vol. 18, no. 11, pp. 2151–2157.
- [174] G. Wei and P. X. Ma, "Structure and properties of nano-hydroxyapatite/polymer composite

- scaffolds for bone tissue engineering,” *Biomaterials*, vol. 25, no. 19, pp. 4749–4757, Aug. 2004.
- [175] L. Yan and D. Jiang, “Study of bone-like hydroxyapatite/polyamino acid composite materials for their biological properties and effects on the reconstruction of long bone defects,” *Drug Des. Devel. Ther.*, vol. 9, p. 6497, Dec. 2015.
- [176] Y. Wang, X. Cao, M. Ma, W. Lu, B. Zhang, and Y. Guo, “A GelMA-PEGDA-nHA composite hydrogel for bone tissue engineering,” *Materials (Basel)*, vol. 13, no. 17, Sep. 2020.
- [177] J. Li, H. Sun, D. Sun, Y. Yao, F. Yao, and K. Yao, “Biomimetic multicomponent polysaccharide/nano-hydroxyapatite composites for bone tissue engineering,” *Carbohydr. Polym.*, vol. 85, no. 4, pp. 885–894, Jul. 2011.
- [178] N. Eliaz and N. Metoki, “Calcium Phosphate Bioceramics: A Review of Their History, Structure, Properties, Coating Technologies and Biomedical Applications,” *Mater. (Basel, Switzerland)*, vol. 10, no. 4, Mar. 2017.
- [179] R. Z. LeGeros, “Properties of osteoconductive biomaterials: Calcium phosphates,” in *Clinical Orthopaedics and Related Research*, 2002, no. 395, pp. 81–98.
- [180] F. Matassi, L. Nistri, D. C. Paez, and M. Innocenti, “New biomaterials for bone regeneration,” *Clinical Cases in Mineral and Bone Metabolism*, vol. 8, no. 1, pp. 21–24, 01-Jan-2011.
- [181] E. García-Gareta, M. J. Coathup, and G. W. Blunn, “Osteoinduction of bone grafting materials for bone repair and regeneration,” *Bone*, vol. 81, pp. 112–121, 2015.
- [182] S. Miao *et al.*, “4D printing smart biomedical scaffolds with novel soybean oil epoxidized acrylate,” *Sci. Rep.*, vol. 6, no. May, pp. 1–10, 2016.
- [183] A. Gandini, “Polymers from renewable resources: A challenge for the future of macromolecular materials,” *Macromolecules*, vol. 41, no. 24, pp. 9491–9504, Dec. 2008.
- [184] S. Miao, P. Wang, Z. Su, and S. Zhang, “Vegetable-oil-based polymers as future polymeric biomaterials,” *Acta Biomaterialia*, vol. 10, no. 4. Elsevier BV, pp. 1692–1704, 2014.
- [185] L. Bao, L. Bian, M. Zhao, J. Lei, and J. Wang, “Synthesis and self-assembly behavior of a biodegradable and sustainable soybean oil-based copolymer nanomicelle,” *Nanoscale Res. Lett.*, vol. 9, no. 1, pp. 1–6, Aug. 2014.
- [186] M. Lebedevaite, J. Ostrauskaite, E. Skliutas, and M. Malinauskas, “Photoinitiator free resins composed of plant-derived monomers for the optical μ -3D printing of thermosets,” *Polymers (Basel)*, vol. 11, no. 1, Jan. 2019.
- [187] D. Mondal, A. Srinivasan, P. Comeau, Y. C. Toh, and T. L. Willett, “Acrylated epoxidized soybean oil/hydroxyapatite-based nanocomposite scaffolds prepared by additive manufacturing for bone tissue engineering,” *Mater. Sci. Eng. C*, vol. 118, p. 111400, Jan. 2021.
- [188] D. Behera and A. K. Banthia, “Synthesis, characterization, and kinetics study of thermal

- decomposition of epoxidized soybean oil acrylate,” *J. Appl. Polym. Sci.*, vol. 109, no. 4, pp. 2583–2590, Aug. 2008.
- [189] W. Liu, T. Xie, and R. Qiu, “Biobased Thermosets Prepared from Rigid Isosorbide and Flexible Soybean Oil Derivatives,” *ACS Sustain. Chem. Eng.*, vol. 5, no. 1, pp. 774–783, Jan. 2017.
- [190] M. Sukul, G. Cama, P. Dubruel, J. E. Reseland, and H. J. Haugen, “Methacrylation increase growth and differentiation of primary human osteoblasts for gelatin hydrogels,” *Emergent Mater.*, vol. 3, no. 4, pp. 559–566, Aug. 2020.
- [191] S. A. Bencherif, A. Srinivasan, F. Horkay, J. O. Hollinger, K. Matyjaszewski, and N. R. Washburn, “Influence of the degree of methacrylation on hyaluronic acid hydrogels properties,” *Biomaterials*, vol. 29, no. 12, pp. 1739–1749, Apr. 2008.
- [192] N. Sultana, “Fabrication techniques and properties of scaffolds,” in *SpringerBriefs in Applied Sciences and Technology*, no. 9783642348013, Springer Verlag, 2013, pp. 19–42.
- [193] E. I. Akpan, X. Shen, B. Wetzel, and K. Friedrich, “Design and Synthesis of Polymer Nanocomposites,” in *Polymer Composites with Functionalized Nanoparticles: Synthesis, Properties, and Applications*, Elsevier, 2018, pp. 47–83.
- [194] A. E. Jakus, A. L. Rutz, and R. N. Shah, “Advancing the field of 3D biomaterial printing,” *Biomed. Mater.*, vol. 11, no. 1, p. 014102, Jan. 2016.
- [195] F. P. W. Melchels, M. A. N. Domingos, T. J. Klein, J. Malda, P. J. Bartolo, and D. W. Huttmacher, “Additive manufacturing of tissues and organs,” *Progress in Polymer Science*, vol. 37, no. 8. Elsevier Ltd, pp. 1079–1104, 01-Aug-2012.
- [196] A. Youssef, S. J. Hollister, and P. D. Dalton, “Additive manufacturing of polymer melts for implantable medical devices and scaffolds,” *Biofabrication*, vol. 9, no. 1, p. 012002, Mar. 2017.
- [197] E. Yang, S. Miao, J. Zhong, Z. Zhang, D. K. Mills, and L. G. Zhang, “Bio-Based Polymers for 3D Printing of Bioscaffolds,” *Polym. Rev.*, vol. 58, no. 4, pp. 668–687, 2018.
- [198] D. Mondal *et al.*, “mSLA-based 3D printing of acrylated epoxidized soybean oil - nano-hydroxyapatite composites for bone repair,” *Mater. Sci. Eng. C*, vol. 130, p. 112456, Nov. 2021.
- [199] D. Mondal and T. L. Willett, “Mechanical properties of nanocomposite biomaterials improved by extrusion during direct ink writing,” *J. Mech. Behav. Biomed. Mater.*, vol. 104, p. 103653, Apr. 2020.
- [200] J. S. Miller and J. A. Burdick, “Editorial: Special Issue on 3D Printing of Biomaterials,” *ACS Biomaterials Science and Engineering*, vol. 2, no. 10. American Chemical Society, pp. 1658–1661, 10-Oct-2016.
- [201] J. A. Lewis, “Direct Ink Writing of 3D Functional Materials,” *Adv. Funct. Mater.*, vol. 16, no. 17, pp. 2193–2204, Nov. 2006.

- [202] N. W. Solís Pinargote, A. Smirnov, N. Peretyagin, A. Seleznev, and P. Peretyagin, “Direct Ink Writing Technology (3D Printing) of Graphene-Based Ceramic Nanocomposites: A Review,” *Nanomaterials*, vol. 10, no. 7, p. 1300, Jul. 2020.
- [203] J. W. Stansbury and M. J. Idacavage, “3D printing with polymers: Challenges among expanding options and opportunities,” *Dent. Mater.*, vol. 32, no. 1, pp. 54–64, Jan. 2016.
- [204] Q. Mu *et al.*, “Digital light processing 3D printing of conductive complex structures,” *Addit. Manuf.*, vol. 18, pp. 74–83, Dec. 2017.
- [205] D. Behera and A. K. Bantia, “Synthesis, characterization, and kinetics study of thermal decomposition of epoxidized soybean oil acrylate,” *J. Appl. Polym. Sci.*, vol. 109, no. 4, pp. 2583–2590, Aug. 2008.
- [206] D. Wang, K. Christensen, K. Chawla, G. Xiao, P. H. Krebsbach, and R. T. Franceschi, “Isolation and characterization of MC3T3-E1 preosteoblast subclones with distinct in vitro and in vivo differentiation/mineralization potential,” *J. Bone Miner. Res.*, vol. 14, no. 6, pp. 893–903, 1999.
- [207] K. Rabel *et al.*, “Controlling osteoblast morphology and proliferation via surface microtopographies of implant biomaterials,” *Sci. Reports 2020 101*, vol. 10, no. 1, pp. 1–14, Jul. 2020.
- [208] N. W. Roehm, G. H. Rodgers, S. M. Hatfield, and A. L. Glasebrook, “An improved colorimetric assay for cell proliferation and viability utilizing the tetrazolium salt XTT,” *J. Immunol. Methods*, vol. 142, no. 2, pp. 257–265, Sep. 1991.
- [209] Y. Zhang, S. E. Chen, J. Shao, and J. J. J. P. Van Den Beucken, “Combinatorial Surface Roughness Effects on Osteoclastogenesis and Osteogenesis,” *ACS Appl. Mater. Interfaces*, vol. 10, no. 43, pp. 36652–36663, Oct. 2018.
- [210] E. Uchimura *et al.*, “In-situ visualization and quantification of mineralization of cultured osteogenic cells,” *Calcif. Tissue Int.*, vol. 73, no. 6, pp. 575–583, Dec. 2003.
- [211] K. Chatterjee *et al.*, “The effect of 3D hydrogel scaffold modulus on osteoblast differentiation and mineralization revealed by combinatorial screening,” *Biomaterials*, vol. 31, no. 19, pp. 5051–5062, Jul. 2010.
- [212] S. Thangakumaran, S. Sudarsan, K. Arun, A. Talwar, and J. James, “Osteoblast response (initial adhesion and alkaline phosphatase activity) following exposure to a barrier membrane/enamel matrix derivative combination,” *Indian J. Dent. Res.*, vol. 20, no. 1, pp. 7–12, Jan. 2009.
- [213] M. Izumiya *et al.*, “Evaluation of MC3T3-E1 Cell Osteogenesis in Different Cell Culture Media,” *Int. J. Mol. Sci.*, vol. 22, no. 14, Jul. 2021.
- [214] A. Ziolkowska, M. Rucinski, A. Pucher, C. Tortorella, G. G. Nussdorfer, and L. K. Malendowicz, “Expression of osteoblast marker genes in rat calvarial osteoblast-like cells, and effects of the endocrine disruptors diphenylpropane, benzophenone-3, resveratrol and silymarin,” *Chem. Biol.*

- Interact.*, vol. 164, no. 3, pp. 147–156, Dec. 2006.
- [215] M. D. Yazid, S. H. Z. Ariffin, S. Senafi, M. A. Razak, and R. M. A. Wahab, “Determination of the differentiation capacities of murines’ primary mononucleated cells and MC3T3-E1 cells,” *Cancer Cell Int.*, vol. 10, no. 1, pp. 1–12, Oct. 2010.
- [216] C. Fu, H. Bai, Q. Hu, T. Gao, and Y. Bai, “Enhanced proliferation and osteogenic differentiation of MC3T3-E1 pre-osteoblasts on graphene oxide-impregnated PLGA–gelatin nanocomposite fibrous membranes,” *RSC Adv.*, vol. 7, no. 15, pp. 8886–8897, Jan. 2017.
- [217] F. Yazid, A. N. M. Kay, W. Y. Qin, N. A. Luchman, R. M. A. Wahab, and S. H. Z. Ariffin, “Morphology and Osteogenic Capability of MC3T3-E1 Cells on Granular Hydroxyapatite Scaffold,” *J. Biol. Sci.*, vol. 19, no. 3, pp. 201–209, Apr. 2019.
- [218] J. P. St-Pierre, M. Gauthier, L. P. Lefebvre, and M. Tabrizian, “Three-dimensional growth of differentiating MC3T3-E1 pre-osteoblasts on porous titanium scaffolds,” *Biomaterials*, vol. 26, no. 35, pp. 7319–7328, Dec. 2005.
- [219] L. Cai, A. S. Guinn, and S. Wang, “Exposed hydroxyapatite particles on the surface of photocrosslinked nanocomposites for promoting MC3T3 cell proliferation and differentiation,” *Acta Biomater.*, vol. 7, no. 5, pp. 2185–2199, May 2011.
- [220] Z. Zheng, L. Zhang, L. Kong, A. Wang, Y. Gong, and X. Zhang, “The behavior of MC3T3-E1 cells on chitosan/poly-L-lysine composite films: effect of nanotopography, surface chemistry, and wettability,” *J. Biomed. Mater. Res. A*, vol. 89, no. 2, pp. 453–465, May 2009.
- [221] Y. Zhao, H. Guan, S. F. Liu, R. C. Wu, and Z. Wang, “Overexpression of QM induces cell differentiation and mineralization in MC3T3-E1,” *Biol. Pharm. Bull.*, vol. 28, no. 8, pp. 1371–1376, Aug. 2005.
- [222] R. Ma *et al.*, “Preparation, characterization, and in vitro osteoblast functions of a nano-hydroxyapatite/polyetheretherketone biocomposite as orthopedic implant material,” *Int. J. Nanomedicine*, vol. 9, no. 1, pp. 3949–3961, Aug. 2014.
- [223] Á. Györgyey *et al.*, “Attachment and proliferation of human osteoblast-like cells (MG-63) on laser-ablated titanium implant material,” *Mater. Sci. Eng. C. Mater. Biol. Appl.*, vol. 33, no. 7, pp. 4251–4259, Oct. 2013.
- [224] H. Tan, S. Guo, S. Yang, X. Xu, and T. Tang, “Physical characterization and osteogenic activity of the quaternized chitosan-loaded PMMA bone cement,” *Acta Biomater.*, vol. 8, no. 6, pp. 2166–2174, Jul. 2012.
- [225] “Cell–Material Interactions: Fundamental Design Issues for Tissue Engineering and Clinical Considerations,” *An Introd. to Biomater.*, pp. 77–110, Jul. 2020.
- [226] J. Y. Wong, J. B. Leach, and X. Q. Brown, “Balance of chemistry, topography, and mechanics at

- the cell–biomaterial interface: Issues and challenges for assessing the role of substrate mechanics on cell response,” *Surf. Sci.*, vol. 570, no. 1–2, pp. 119–133, Oct. 2004.
- [227] W. M. Saltzman and T. R. Kyriakides, “Cell Interactions with Polymers,” *Princ. Tissue Eng. Fourth Ed.*, pp. 385–406, Jan. 2014.
- [228] J. Lincks *et al.*, “Response of MG63 osteoblast-like cells to titanium and titanium alloy is dependent on surface roughness and composition,” *Biomaterials*, vol. 19, no. 23, pp. 2219–2232, 1998.
- [229] D. E. Discher, P. Janmey, and Y. L. Wang, “Tissue cells feel and respond to the stiffness of their substrate,” *Science*, vol. 310, no. 5751, pp. 1139–1143, Nov. 2005.
- [230] K. Kurima *et al.*, “Cell locomotion and focal adhesions are regulated by substrate flexibility,” *Proc. Natl. Acad. Sci.*, vol. 94, no. 25, pp. 13661–13665, Dec. 1997.
- [231] R. J. Pelham and Y. L. Wang, “Cell locomotion and focal adhesions are regulated by the mechanical properties of the substrate,” *Biol. Bull.*, vol. 194, no. 3, pp. 348–350, 1998.
- [232] D. H. Lee, J. S. Han, J. H. Yang, and J. B. Lee, “MC3T3-E1 CELL RESPONSE TO PURE TITANIUM, ZIRCONIA AND NANO-HYDROXYAPATITE,” <http://dx.doi.org/10.1142/S0217979209061226>, vol. 23, no. 6–7, pp. 1535–1540, Jan. 2012.
- [233] R. Shu, R. McMullen, M. J. Baumann, and L. R. McCabe, “Hydroxyapatite accelerates differentiation and suppresses growth of MC3T3-E1 osteoblasts,” *J. Biomed. Mater. Res. A*, vol. 67, no. 4, pp. 1196–1204, Dec. 2003.
- [234] K. H. Son and J. W. Lee, “Synthesis and Characterization of Poly(Ethylene Glycol) Based Thermo-Responsive Hydrogels for Cell Sheet Engineering,” *Mater. (Basel, Switzerland)*, vol. 9, no. 10, Oct. 2016.
- [235] J. Elisseff, W. McIntosh, K. Anseth, S. Riley, P. Ragan, and R. Langer, “Photoencapsulation of chondrocytes in poly(ethylene oxide)-based semi-interpenetrating networks.,” *undefined*, 2000.
- [236] S. J. Bryant, C. R. Nuttelman, and K. S. Anseth, “The effects of crosslinking density on cartilage formation in photocrosslinkable hydrogels.,” *Biomed. Sci. Instrum.*, vol. 35, pp. 309–314, Jan. 1999.
- [237] J. W. Nichol, S. T. Koshy, H. Bae, C. M. Hwang, S. Yamanlar, and A. Khademhosseini, “Cell-laden microengineered gelatin methacrylate hydrogels,” *Biomaterials*, vol. 31, no. 21, pp. 5536–5544, Jul. 2010.
- [238] E. Quinlan, A. López-Noriega, E. Thompson, H. M. Kelly, S. A. Cryan, and F. J. O’Brien, “Development of collagen-hydroxyapatite scaffolds incorporating PLGA and alginate microparticles for the controlled delivery of rhBMP-2 for bone tissue engineering,” *J. Control. Release*, vol. 198, pp. 71–79, Jan. 2015.
- [239] M. B. Kim, Y. Song, and J. K. Hwang, “Kirenol stimulates osteoblast differentiation through activation of the BMP and Wnt/ β -catenin signaling pathways in MC3T3-E1 cells,” *Fitoterapia*, vol.

- 98, pp. 59–65, Oct. 2014.
- [240] D. Georgess, I. Machuca-Gayet, A. Blangy, and P. Jurdic, “Podosome organization drives osteoclast-mediated bone resorption,” *Cell Adh. Migr.*, vol. 8, no. 3, pp. 192–204, May 2014.
- [241] J. Pasuri *et al.*, “Osteoclasts in the interface with electrospun hydroxyapatite,” *Colloids Surf. B. Biointerfaces*, vol. 135, pp. 774–783, 2015.
- [242] M. Roy and S. Bose, “Osteoclastogenesis and osteoclastic resorption of tricalcium phosphate: Effect of strontium and magnesium doping,” *J. Biomed. Mater. Res. - Part A*, vol. 100 A, no. 9, pp. 2450–2461, 2012.
- [243] C. A. Martins, G. Leyhausen, J. Volk, and W. Geurtsen, “Effects of alendronate on osteoclast formation and activity in vitro,” *J. Endod.*, vol. 41, no. 1, pp. 45–49, Jan. 2015.
- [244] M. Marchisio, M. Di Carmine, R. Pagone, A. Piattelli, and S. Miscia, “Implant surface roughness influences osteoclast proliferation and differentiation,” *J. Biomed. Mater. Res. B. Appl. Biomater.*, vol. 75, no. 2, pp. 251–256, Nov. 2005.
- [245] F. Chen *et al.*, “Effects of hydroxyapatite surface nano/micro-structure on osteoclast formation and activity,” *J. Mater. Chem. B*, vol. 7, no. 47, pp. 7574–7587, 2019.
- [246] A. K. Macmillan, F. V. Lamberti, J. N. Moulton, B. M. Geilich, and T. J. Webster, “Similar healthy osteoclast and osteoblast activity on nanocrystalline hydroxyapatite and nanoparticles of tri-calcium phosphate compared to natural bone,” *Int. J. Nanomedicine*, vol. 9, no. 1, pp. 5627–5637, 2014.
- [247] D. O. Costa *et al.*, “The differential regulation of osteoblast and osteoclast activity by surface topography of hydroxyapatite coatings,” *Biomaterials*, vol. 34, no. 30, pp. 7215–7226, Oct. 2013.
- [248] J. Brinkmann, T. Hefti, F. Schlottig, N. D. Spencer, and H. Hall, “Response of osteoclasts to titanium surfaces with increasing surface roughness: an in vitro study,” *Biointerphases*, vol. 7, no. 1–4, pp. 1–9, 2012.
- [249] F. Saltel, A. Chabadel, E. Bonnelye, and P. Jurdic, “Actin cytoskeletal organisation in osteoclasts: a model to decipher transmigration and matrix degradation,” *Eur. J. Cell Biol.*, vol. 87, no. 8–9, pp. 459–468, Sep. 2008.
- [250] D. Geblinger, C. Zink, N. D. Spencer, L. Addadi, and B. Geiger, “Effects of surface microtopography on the assembly of the osteoclast resorption apparatus,” *J. R. Soc. Interface*, vol. 9, no. 72, pp. 1599–1608, Jul. 2012.
- [251] D. Geblinger, L. Addadi, and B. Geiger, “Nano-topography sensing by osteoclasts,” *J. Cell Sci.*, vol. 123, no. Pt 9, pp. 1503–1510, May 2010.
- [252] J. Padmanabhan *et al.*, “Regulation of cell-cell fusion by nanotopography,” *Sci. Reports 2016 61*, vol. 6, no. 1, pp. 1–9, Sep. 2016.
- [253] S. Redey *et al.*, “Osteoclast adhesion and activity on synthetic hydroxyapatite, carbonated

- hydroxyapatite, and natural calcium carbonate: relationship to surface energies.,” *undefined*, 1999.
- [254] B. Ten Harkel, T. Schoenmaker, D. I. Picavet, N. L. Davison, T. J. De Vries, and V. Everts, “The Foreign Body Giant Cell Cannot Resorb Bone, But Dissolves Hydroxyapatite Like Osteoclasts,” *PLoS One*, vol. 10, no. 10, Oct. 2015.
- [255] Z. Sheikh, P. J. Brooks, O. Barzilay, N. Fine, and M. Glogauer, “Macrophages, Foreign Body Giant Cells and Their Response to Implantable Biomaterials,” *Mater. (Basel, Switzerland)*, vol. 8, no. 9, pp. 5671–5701, 2015.
- [256] K. Matsuo and N. Irie, “Osteoclast-osteoblast communication,” *Arch. Biochem. Biophys.*, vol. 473, no. 2, pp. 201–209, May 2008.
- [257] C. Heinemann, S. Heinemann, H. Worch, and T. Hanke, “Development of an osteoblast/osteoclast co-culture derived by human bone marrow stromal cells and human monocytes for biomaterials testing,” *Eur. Cells Mater.*, vol. 21, no. January, pp. 80–93, 2011.
- [258] G. Borciani, G. Montalbano, N. Baldini, G. Cerqueni, C. Vitale-Brovarone, and G. Ciapetti, “Co-culture systems of osteoblasts and osteoclasts: Simulating in vitro bone remodeling in regenerative approaches,” *Acta Biomater.*, vol. 108, pp. 22–45, May 2020.
- [259] P. S. Sharif and M. Abdollahi, “The role of platelets in bone remodeling,” *Inflamm. Allergy Drug Targets*, vol. 9, no. 5, pp. 393–399, 2010.
- [260] B. P. Sinder, A. R. Pettit, and L. K. McCauley, “Macrophages: Their Emerging Roles in Bone,” *J. Bone Miner. Res.*, vol. 30, no. 12, pp. 2140–2149, Dec. 2015.
- [261] A. G. Robling and C. H. Turner, “Mechanical signaling for bone modeling and remodeling,” *Crit. Rev. Eukaryot. Gene Expr.*, vol. 19, no. 4, pp. 319–338, 2009.
- [262] C. W. Hsu, R. M. Olabisi, E. A. Olmsted-Davis, A. R. Davis, and J. L. West, “Cathepsin K-sensitive poly(ethylene glycol) hydrogels for degradation in response to bone resorption,” *J. Biomed. Mater. Res. - Part A*, vol. 98 A, no. 1, pp. 53–62, 2011.

Appendix 1 – Pilot study of osteoblast interaction with nanocomposites containing 30% nHA

A pilot study of osteoblast interaction with nanocomposites was done on nanocomposite discs containing 30% nHA (SP30-60S, 70S, 80S) that were 3D-printed using an extrusion-based Hyrel 3D-printer. dMC3T3-OB cells were cultured on these nanocomposite discs for 1, 3, and 7 days. The results of this study were submitted as an abstract for the World Biomaterials Congress 2020 and accepted as a poster presentation.

To make ink with a higher volume fraction of nano-hydroxyapatite (30%), first AESO was dissolved in ethanol. Nano-hydroxyapatite particles were added gradually to the mixture and dispersed using an ultrasonic homogenizer for 3 min at each step. The concentration of nano-hydroxyapatite powder in ethanol was 50% (w/v). Afterward, PEGDA was added to the mixture and homogenized for approximately 5 min. Finally, Igracure 819 was dissolved in acetone (10% w/v) separately and then added to the ink mixture at 1 vol% of total ink. The mixture was kept under the vacuum to evaporate the ethanol and acetone. The nanocomposite ink was printed as cylindrical discs (9.4 mm diameter and 1 mm thickness) after the complete evaporation of ethanol and acetone. Discs were printed by using an extrusion-based 3D printer (Hyrel System 30M, USA) with simultaneous layer-by-layer UV curing (385 nm) (Figure 0-1). Three nanocomposite inks were prepared with 30 vol% of nHA (30) with different AESO to PEGDA ratio (AESO/PEGDA:60,70,80):

- i) 42 vol% AESO (S) and 28 vol% PEGDA (P),
- ii) 49 vol% AESO (S) and 21 vol% PEGDA (P), and
- iii) 56 vol% AESO (S) and 14 vol% PEGDA (P).

These compositions hereafter are referred to as SP30- 60S, 70S, and 80S, respectively.

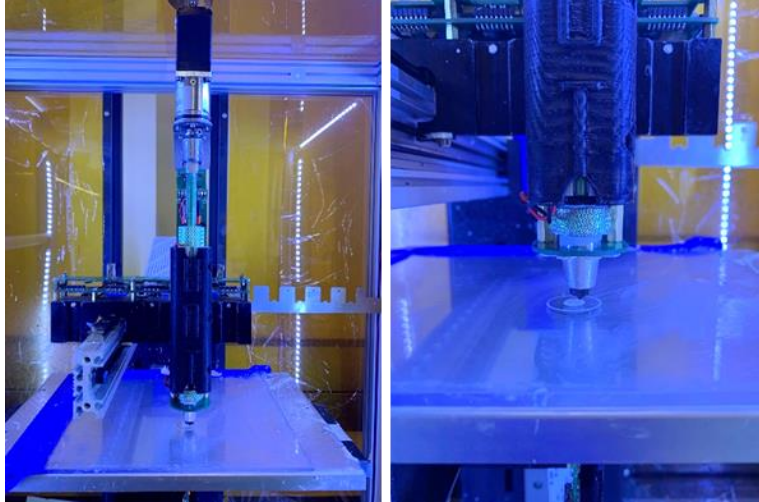


Figure 0-1. Image of Hyrel 3D-printer and discs

After printing discs, a UV post-print curing step was done in a Creative CADworks curing unit (CureZone, Canada). The nanocomposite discs were exposed to lower intensity UV light on each side for 5 minutes and then washed with ethanol 70% to remove any debris and uncured particles on the surface.

Osteoblast adhesion and proliferation on Acrylated Epoxidized Soybean Oil and Hydroxyapatite-Based 3D-printed Nanocomposites

Zahra Haghpanah¹, Dibakar Mondal¹, Maud Gorbet², Thomas L Willett¹

¹Composite Biomaterial Systems Laboratory, ²Material Interactions with Biological Systems
Department of Systems Design Engineering, University of Waterloo, 200 University Ave. West, Waterloo
N2L 3G1, Canada

Introduction: Ideally, a synthetic bone graft biomaterial would have similar or better mechanical properties, biocompatibility, and osteoconductivity than allograft bone [1,2]. An ideal bone graft should be non-cytotoxic and able to induce beneficial cell-material responses such as adhesion and proliferation of bone cells *in vitro* [3]. We have recently developed 3D printable novel nanocomposites consisting of Acrylated Epoxidized Soybean Oil (AESO), Polyethylene Glycol Diacrylate (PEGDA) and nano-Hydroxyapatite (nHA). In this study, we evaluated the *in vitro* viability and metabolic activity of osteoblast cells on these novel nanocomposites. We hypothesized that our nanocomposites support cell adhesion and proliferation without depending significantly on the amounts of AESO and PEGDA.

Experimental methods: The nanocomposite inks were prepared by mixing AESO, PEGDA (Sigma Aldrich Co.) and nHA (MKNano Inc. Canada) using an ultrasonic homogenizer. Three nanocomposite inks were prepared with 30 vol% of nHA and, i) 42 vol% AESO and 28 vol% PEGDA (60S), ii) 49 vol% AESO and 21 vol% PEGDA (70S), and iii) 56 vol% AESO and 14 vol% PEGDA (80S). Irgacure 819 photoinitiator was used for UV curing. The inks were then printed as cylindrical discs (9.4 mm diameter and 1 mm thickness) by using an extrusion-based 3D printer (Hyrel System 30M, USA) with simultaneous layer-by-layer UV curing (385nm). For tensile test, inks were cast into dogbone-shaped mold and cured using UV. These specimens were then tested in a Psylotech μ TS (Psylotech Inc., USA) with strain measured and

calculated using microscope-enabled digital image correlation. The 3D printed discs were washed with ethanol, phosphate buffered saline, and incubated (at 37 °C, 5% CO₂) in Minimum Essential Medium Alpha medium overnight prior to cell seeding. Osteoblast cells were differentiated from mouse pre-osteoblast MC3T3-E1 by using the osteogenesis assay kit (EMD Millipore). Hydroxyapatite (HA) discs (BioTek, USA) were used as control. 3×10⁴ osteoblast cells per disc were seeded. XTT (Trevigen USA) and live/dead assay (Life Technologies Inc., CA) were performed on day 1 and day 3 post seeding. To study cell adhesion and proliferation, cells were fixed using 4% paraformaldehyde and F-actin and nuclei were then labelled using Alexa Flour 488 phalloidin⁴ (Life Technologies Inc., CA) and DAPI (Dojindo Molecular Technologies Inc., Japan), respectively. The staining was imaged using a LSM 700 confocal microscope (Zeiss, Germany).

Results and discussion: Ultimate tensile stress and modulus values increased with increasing PEGDA content in the nanocomposites (Figure 0-2.A). Live-dead assay results after 1 and 3 days (Figure 0-2.C) demonstrated excellent viability of osteoblasts with all three nanocomposites. XTT showed slightly better cellular metabolic activity for 60S and 80S compared with the 70S nanocomposite at day 3 (Figure 0-2.B). However, metabolism or proliferation was impaired relative to the HA controls at Day 3. Adhesion, spreading and proliferation of osteoblasts are significant parameters that indicate good osteoconductivity [4]. As illustrated in Figure 0-2.D, cells on 3D-printed nanocomposite discs showed a well-organized network of actin filaments. These results clearly demonstrated excellent cell-material interactions on AESO/PEGDA/nHA nanocomposites.

Conclusion: The novel nanocomposites made from AESO, PEGDA and nHA have good mechanical properties and excellent cell-material interactions. PEGDA enhanced the tensile mechanical properties of the nanocomposites without detectably affecting cell-material interactions. All 3D-printed nanocomposites supported cell viability and metabolic activity of mouse osteoblasts, indicating a lack of cytotoxic response.

Acknowledgments: This work is supported by the Canadian Institutes of Health Research and the Natural Sciences & Engineering Research Council-CREATE training program in Global Biomedical Technology Research and Innovation.

References:

1. Z. Zhang *et al.*, *Acta Biomater.* vol. 8, no. 1, pp. 13–19, 2012.
2. C. Heinemann *et al.*, *Eur. Cells Mater.*, vol. 21, no. January, pp. 80–93, 2011.
3. C. Steffi *et al.*, *J. Funct. Biomater.*, vol. 9, no. 1, 2018.
4. S. Miyamoto *et al.*, *Science*, 267(5199), 883-885, 1995.

⁴ Phalloidin actin staining is used to observe cell adhesion and the organization of the cell cytoskeleton. Phalloidin is a fluorescent probe that binds specifically to actin filaments. The fluorescent-labelled actin filaments are visualized using LSM 700 confocal microscope (Carl Zeiss, Germany). The images are viewed in ImageJ software and optimized for brightness and contrast.

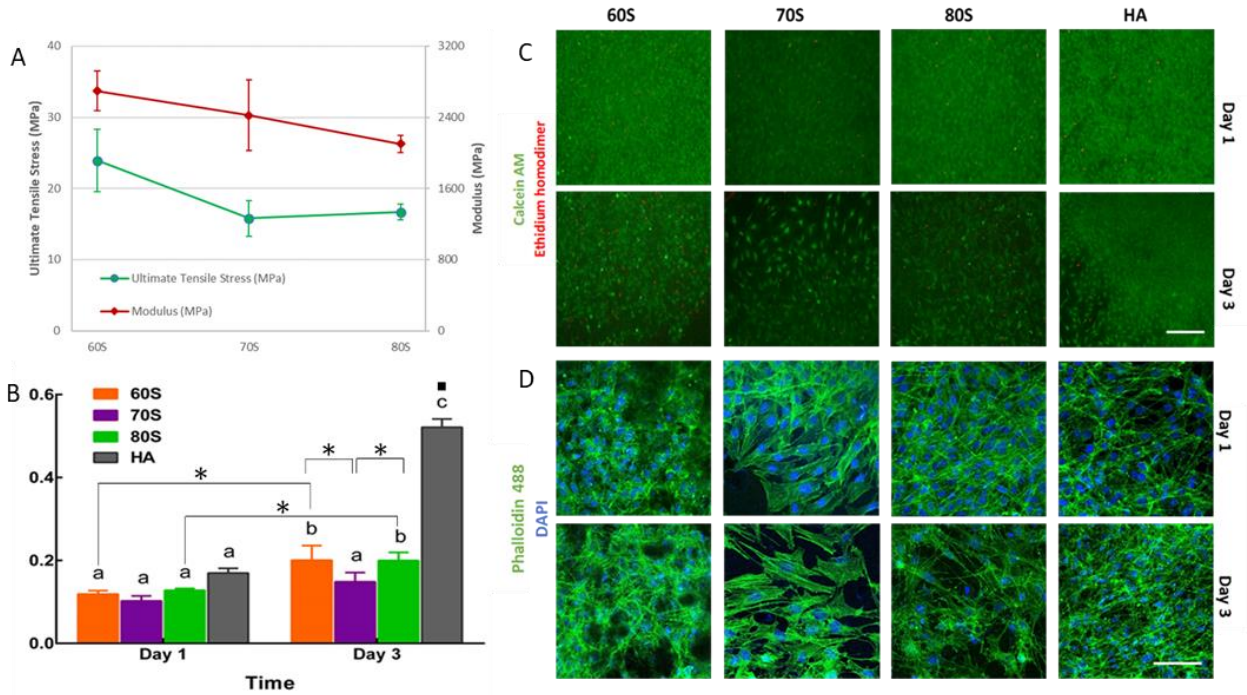


Figure 0-2. A) Tensile strength and elastic modulus values of 3D printed SP30 nanocomposites. Data are mean \pm SD [$n=3$]. B) Osteoblast metabolic activity as measured by the XTT assay. Values are mean \pm SD [$n=3$]. Two-way ANOVA and Tukey's multiple comparison test were used for statistical analysis. *statistically significant, $p<0.05$, •statistically significant from all samples, $p<0.05$. C) Live-dead assay showing live cells (green) and dead cells (red). Few dead cells were observed. Scale bar: 300 μm . D) Cytoskeletons of osteoblast cells seeded on the nanocomposites for day-1 and day-3. F-actin and nuclei were labelled with phalloidin 488 (green) and DAPI (blue), respectively. Scale bar: 100 μm .

Appendix 2 – Osteoclast proliferation and morphology on nanocomposite discs

On SP0, SP10, SP30, and HA discs, 1×10^4 cells/cm² of dRAW-OC cells were cultured with 30 ng/ml RANKL in the culture medium. The XTT experiment was done on SP0, SP10, and SP30 nanocomposite discs with the same protocol for osteoblast study (Figure 0-1). The XTT assay was performed after 48 hours, 7, and 14 days to study the proliferation of dRAW-OC cells on the discs. A significant increase in proliferation ($p < 0.05$) was observed on SP10 and HA discs at day 7 and day 14.

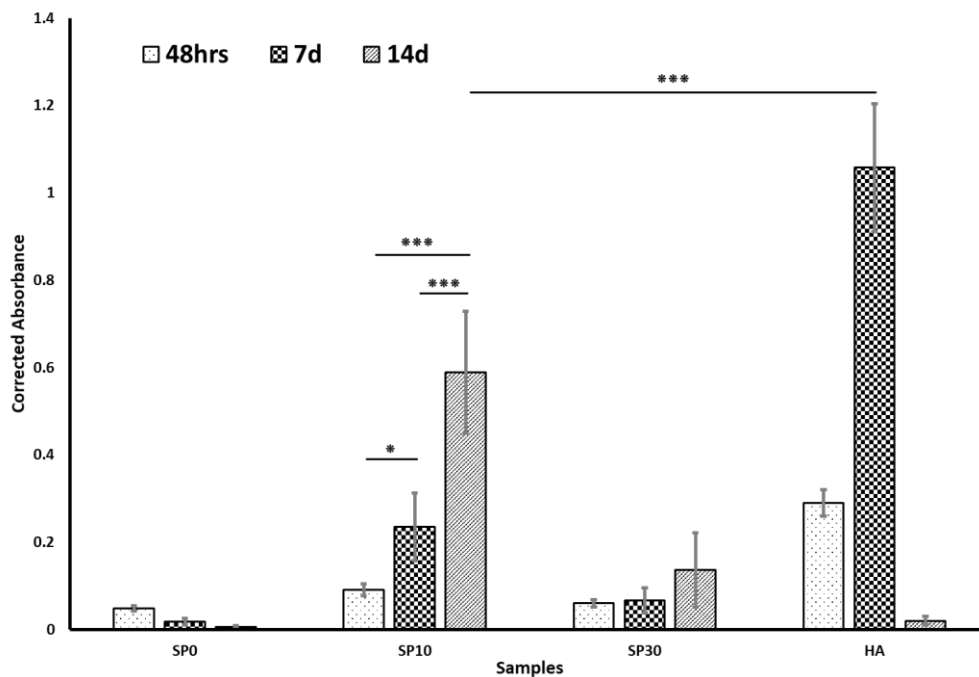


Figure 0-1. dRAW-OC cells proliferation on 3D printed nanocomposite discs SP0 (0% nHA), SP10 (10% nHA), SP30 (30% nHA). Proliferation of dRAW-OC cells as measured using the XTT assay. Data are means \pm SD ($n=4$ for nanocomposite and HA discs, *** statistically significant $p \leq 0.001$).

The morphology of differentiated RAW264.7 cells on SP10 and SP30 nanocomposite discs was observed with SEM using a Quanta FEG 250 (ThermoFisher Scientific, USA). Cells were washed with 0.2M sodium phosphate buffer (SPB) at pH 7.2. Afterwards, cells were fixed with 2.5% Glutaraldehyde in 0.2M SPB, dehydrated in a sequential series of ethanol, coated with gold, and then observed using SEM (Figure 0-2). The morphology of osteoclasts can be seen in the SEM images of SP10 and SP30

nanocomposite discs; this confirms the presence of osteoclast cells on the surface of the nanocomposite discs.

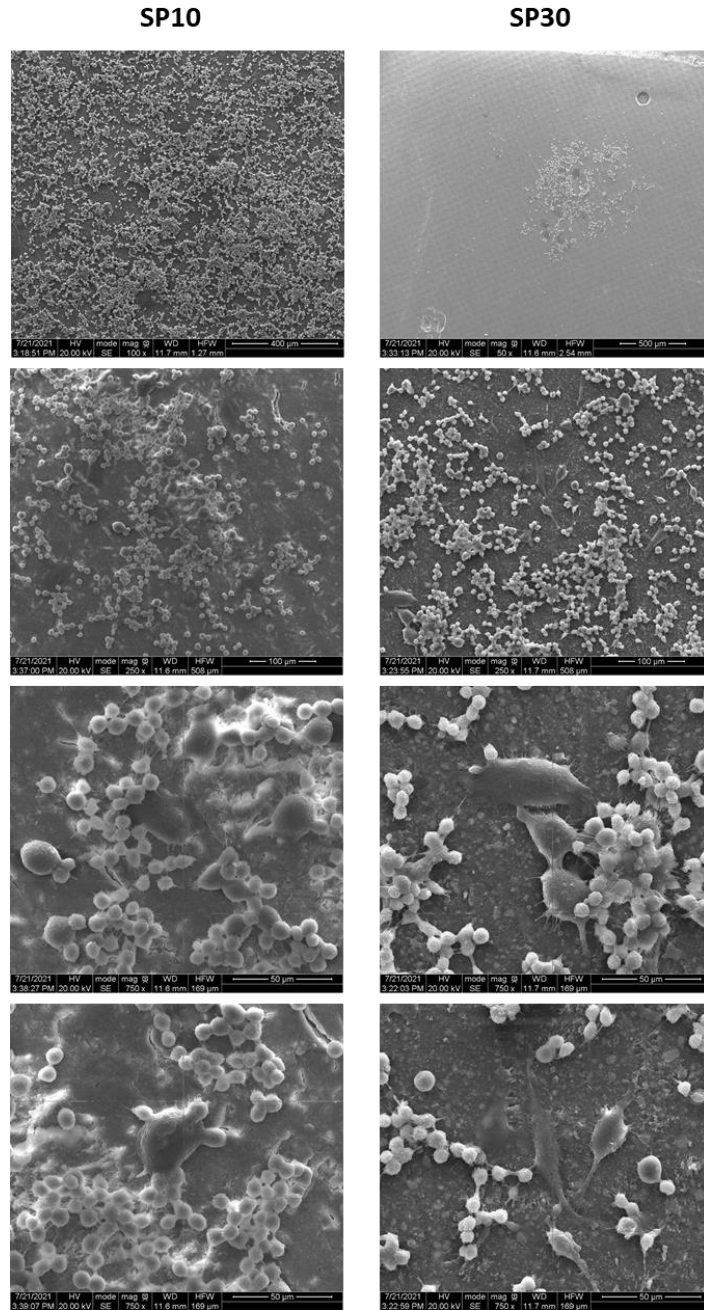


Figure 0-2. SEM images RAW264.7 and dRAW-OC cells grown on SP10 (10% nHA) and SP30 (30% nHA) nanocomposite discs under RANKL stimulation at day 14.